UNIVERSITY OF THE WITWATERSRAND

Numerical Modelling of the Insect Respiratory System and Gas Flow

Author:
Simphiwe Simelane

Supervisors:
Prof Shirley Abelman
Prof Frances Duncan

A thesis submitted in fulfilment of the requirements for the degree of Doctor of Philosophy

in the

School of Computer Science and Applied Mathematics

WITS
UNIVERSITY

November 2015

Declaration of Authorship

I, Simphiwe Simelane, declare that this thesis titled, 'Numerical Modelling of the Insect Respiratory System and Gas Flow' and the work presented in it are my own. I confirm that:

- This work was done wholly or mainly while in candidature for a research degree at this University.
- Where any part of this thesis has previously been submitted for a degree or any other qualification at this University or any other institution, this has been clearly stated.
- Where I have consulted the published work of others, this is always clearly attributed.
- Where I have quoted from the work of others, the source is always given. With the exception of such quotations, this thesis is entirely my own work.
- I have acknowledged all main sources of help.
- Where the thesis is based on work done by myself jointly with others, I have made clear exactly what was done by others and what I have contributed myself.

Signed: _____

Date: _____

"The thesis is completed and now the spiracles are closed."

Prof S. Abelman
S. Simelane

UNIVERSITY OF THE WITWATERSRAND

Abstract

Faculty of Science
School of Computer Science and Applied Mathematics

Doctor of Philosophy

Numerical Modelling of the Insect Respiratory System and Gas Flow

by Simphiwe Simelane

The understanding of fluid flow at microscale geometrics is an increasingly important field in applied science and mechanics, especially in bioinspiration and biomimetics. These fields seek to imitate processes and systems in biology to design improved efficient engineering devices. In this thesis, inspired by the efficiency of the insect tracheal system in transporting respiratory gases at microscale, mathematical models that both mimic and explain the gas exchange process are developed. Models for the simultaneous movement of respiratory gases across the insect spiracle, gas transfer from one respiratory chamber to the next, end diffusion and tissue absorption at the tracheole tips, and tracheal fluid transport are presented. Expressions for tracheal partial pressures of the respiratory gases, rate of change of gas concentrations, rate of tracheal volume change, spiracle behaviour on net gas flow, cellular respiration and tissue absorption, and global gas movement within the insect are presented as well.

Two versions of bioinspired pumping mechanism that is neither peristaltic nor belongs to impedance mismatch class of pumping mechanism are then presented. A paradigm for selectively pumping and controlling gases at the microscale in a complex network of channels is presented. The study is inspired by the internal flow distributions of respiratory gases produced by rhythmic wall contractions in dung beetle tracheal networks. These networks have been shown to efficiently manage fluid flow compared to current produced microfluidic devices. The insect-like pumping models presented are expected to function efficiently in the microscale flow regime in a simple or complex network of channels. Results show the ability to induce a unidirectional net flow by using an inelastic channel with at least two moving contractions. These results might help in explaining some of the physiological systems in insects and may help in fabricating novel efficient microfluidic devices.

In this study, both theoretical and the Differential Transform Method are used to solve the flexible trachea with gas exchange problem as well as the 2D viscous flow transport with or without prescribed moving wall contractions problem. Both lubrication theory and quasi-steady approximations at low Reynolds number are used in the derivation of theoretical analysis. Moreover,

an analytical investigation into compressible gas flow with slight rarefactions through the insect trachea and tracheoles is undertaken, and a complete set of asymptotic analytical solutions is presented. Then, estimation of the Reynolds and Mach numbers at the channel terminal ends where the tracheoles directly deliver respiratory gases to the cells is obtained by comparing the magnitude of the different forces in the compressible gas flow. The 2D Navier-Stokes equations with a slip boundary condition are used to investigate the compressibility and rarefied effects in the respiratory channels.

Acknowledgements

First, I would like to express my sincere appreciation to my supervisors Professor S. Abelman and Professor F.D. Duncan for their tireless guidance, assistance, patience and encouragement. I appreciate their immense knowledge and continuous support during my PhD study, whilst allowing me the room to work in my own way. One simply could not have imagined having better supervisors and mentors for PhD study. Without their supervision, this work would not have been possible.

I must acknowledge staff members and higher degree students from the School of Computer Science and Applied Mathematics for their outstanding academic and social contribution which made the school an excellent place to do my research work. To my friends around Johannesburg and in Swaziland, thank you for all the cheerful and happy times that kept me going.

I highly recognize the contribution given by my wonderful family who have always been there for me. My dear momma Jabu Simelane has been my pillar of strength and everything I have accomplished is indebted to her. To Sandile, John, Bagezile and my sisters, Gugu, Bubu, Sengetile, Phindile, Ntando and Nonophile thanks for your unconditional encouragement and love. I appreciate everything you have done for me.

Finally, I thank the University of the Witwatersrand, Johannesburg and the DST-NRF Centre of Excellence in Mathematical and Statistical Sciences (CoE-MaSS) for financial support.

Contents

List of Figures

List of Tables

In dedication to my mother Jabu for making me be who I am and my family who supported me throughout my life. I love you all.

Chapter 1

Introduction

Insects are unique in that they differ in morphology from almost all other phyla and use different physiological structures and processes. The insect respiratory system which uses common distribution mechanisms for efficient transport of respiratory gases is an example. In this thesis, the tracheal system and the discontinuous exchange of respiratory gases through insect spiracles are described. The phases of the discontinuous gas exchange cycle are described and its significance in insect physiology is presented. A brief introduction about the insect's tracheal network of tubes and their rhythmic wall contraction pattern is given. Various transport mechanisms that possibly exist in the tracheal network are also explored. Previous studies that form a basis for the theoretical analysis and the Differential Transform Method (DTM)) are presented.

1.1 Preface

The phenomenon by which respiratory gases, namely oxygen (O_2) and carbon dioxide (CO_2), manage to move across the insect spiracles as well as the efficient transport of these gases in the insect trachea is an important challenging problem and its solution has many scientific applications. For instance, biomimetic microfluidic devices based on these physiological systems in insects have, in recent years, gained attention. There have been numerous attempts to manufacture devices in the guise of simple channels with different membranes attached along their length to act as pumping actuators that mimic these systems. These membranes are currently manufactured using multilayer soft lithography techniques (MSL) (see Aboelkassem and Staples [122], and Pandolfi and Ortiz [139]). Solutions to microscale flow in the trachea as well as the simultaneous movement of respiratory gases across confined spaces can also provide insights into solving the problem of controlled pumping of microlitres of fluids in microgeometrics. Pressure-driven flow and valveless mechanisms are two main techniques currently used to

transport microlitres of fluids at microscale. However their functional drawbacks and complex designs make it difficult with current microfabrication techniques to manufacture them.

This thesis presents novel models tracing the simultaneous movement of respiratory gases across the insect spiracles, describes cellular respiration and tissue absorption of the respiratory gases in the trachea, oxygen uptake by mitochondria and carbon dioxide transport in the form of a bicarbonate at the tracheole tips, and a novel model describing microscale fluid flow in the trachea. Gas is considered as a fluid. Liquids and gases are sometimes grouped together as fluids because they flow very readily under the application of an external force.

Figure 1.1 summarizes the three main models presented, namely:

1. Outer ventilation (interactions across insect spiracles).
2. Inner ventilation,
   - end diffusion, and
   - compartmental exchange.
3. Microscale flow transport induced by rhythmic wall contractions.

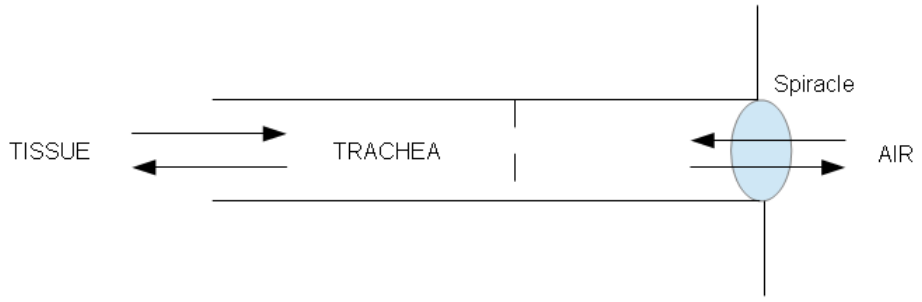

FIGURE 1.1: Schematic view of the problem layout. Three compartments are considered: the atmosphere, trachea and respiring cells.

The first part of the introduction describes the insect respiratory system, tracheal system, discontinuous gas exchange, and rhythmic tracheal wall contractions. The tracheal wall contractions are hypothesized to be the main driving force behind transporting fluids in these complex networks. The second part summarizes some of the theoretical and numerical investigations that form the basis of our derived mathematical models.

1.2 Insect respiratory system

All terrestrial animals exchange oxygen (O_2) and carbon-dioxide (CO_2) with the atmosphere and thereby costs are incurred in the form of water vapor (H_2O) loss during this exchange.

Inevitable water loss stems from the characteristic of terrestriality [13]; adequate gas exchange requires large surface areas of high-conductance tissues which are usually invaginated (condition of being folded inward), high conductance tissues saturate internal exchange spaces with water vapor, and those surfaces must be ventilated by the atmosphere, at least intermittently. Water vapor tends to move across the concentration gradient into the surrounding dry air. The insects thus face a gas-water trade-off in which higher rates of gas exchange result in higher rates of water loss. The severity of this trade-off depends on the portion of total water loss through the gas exchange system. The temperature and aridity of the insect's habitat plays a crucial role in determining the amount of water loss during the respiration process.

Gas exchange in insects is a continual conflict between the need to support aerobic need and the need to reduce respiratory water loss [7, 9, 11]. Some insects exchange respiratory gases with the atmosphere discontinuously permitting gas exchange while minimizing water loss, despite their relative high metabolic rates. While oxygen consumption and carbon dioxide production are continuous, the external elimination of gases is discontinuous [9, 24].

1.2.1 The Tracheal System

Insects develop a respiratory system called the tracheal system which is responsible for transporting oxygen and carbon dioxide in the gas phase. Unlike most animals, insects do not rely on internal circulation to provide oxygen to their tissues [50]. An advantage of this mechanism is saving energy as compared to the costly convective transport of gases dissolved in a fluid.

The insect tracheal system consists of gas-filled, branching tubes that spread into all parts of the insect body [24]. The ends of the tubes open into the external cuticle at the spiracles. The spiracles are pores augmented in most insects with a valve-like structure which helps to seal the tracheal system. The action of these spiracles ultimately affects the changes in diffusive and convective conductance which are necessary to control the tracheal gas composition. The principal sites for gas exchange are the fine branches (less than a μm in diameter) at the tips of the tracheal system, which penetrate the tissues [24]. Note that the insect outer cuticle is impermeable to water [9]; thus water loss is through the spiracles. Figure 1.2 gives a schematic view of an insect's tracheal system.

Sieve plate: A sieve plate is a dense network of trabeculae which consist of exocuticular structures and prevents entry of unwanted substances such as parasites, dust or water drops [21]. This plate has been hypothesized to reduce bulk airflow due to increased frictional drag, which in turn is thought to minimize water loss [21].

The closing muscle: The closing apparatus of spiracles in Saturnidae like *Attucus atlas* is of the lever-and-bar type [30]. The single closing muscle, when contracted, presses the bar against

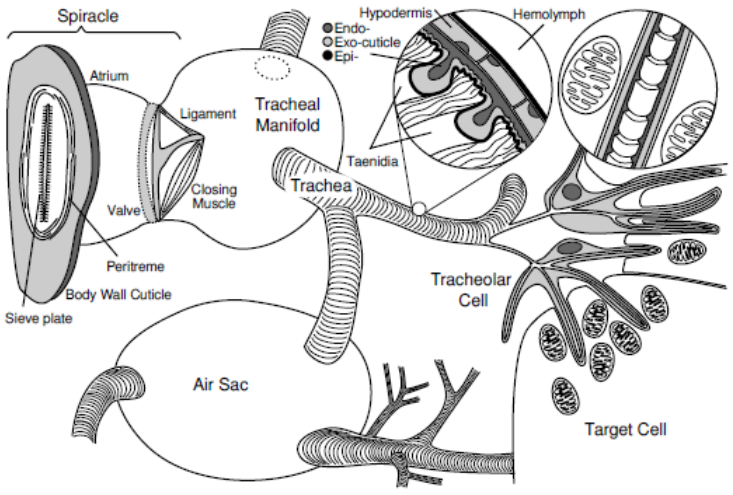

FIGURE 1.2: Schematic view of the problem layout. Three compartments are considered: the atmosphere, trachea and the respiring cells. (Photo from Chapman [50] and Miller [21])

the opposite wall of the spiracle and closes it [7, 87]. When the muscle relaxes, an elastic ligament made of connective tissue and having been tensed by the contraction pulls the lever back and stretches the closing muscle. This action may then allow gas exchange between the tracheal space and the surrounding air.

Trachea: These are gas filled tubes that form a variable branched hierarchy and constitute a great part of the tracheal system. The tracheal walls show the cross section of insect cuticle with a base epidermal layer which excretes the endo- and exocuticle. In the trachea, the taenidiae form helical rings of cuticle on top of the tracheal cuticle and have been attributed to prevent the collapse of the trachea. It is assumed that no or only limited lateral diffusion occurs across the tracheal wall because of the relatively thick cuticle. The oxygen pathway is thought to follow the tracheal lumen up to the fine terminal branches before the gas dissolves in the hemolymph and tissue liquids.

Tracheoles: The trachea opens up to the finest branches of the tracheal system called the tracheoles with a diameter of less than $1\mu m$. The minimum diameter is probably bound by the mean free path length of diffusion molecules, as smaller diameters would impede O_2 diffusion along the tracheoles [14]. Despite their small size, the tracheoles are similar to the trachea in outer appearance [21].The tips of the tracheoles are filled with fluid and are barely visible [15]. Because the meniscus is dependent on local oxygenation status of the surrounding tissue, it is thought that the fluid serves as a kind of regulator of oxygen supply [7].

Air sacs: These are an auxiliary structure in the tracheal system which serve various roles and probably not all of them are respiratory. Air sacs provide extra space for tissues to grow into during development, as the outer volume is defined by the cuticle and cannot be increased.

However, air sacs do increase tracheal volume and also provide the tracheal system with sections of increased compliance. Therefore they might as well facilitate convective distribution of air by their repeated collapse [16].

1.2.2 Discontinuous gas exchange (*DGC*)

The earliest report of the phenomenon known as *DGC* in insects can be found in Punt [17]. At first, it was seen as an error in respiratory measurements, however, a more systematic investigation is in progress. Even today, the *DGC* pattern still puzzles investigators.Usually *DGCs* are demonstrated using the release of CO_2 through the spiracles as a marker for their behaviour and they show themselves as a rhythm in the external gas exchange (Figure 1.3). Most often, this pattern of gas exchange is observed in resting insects at low temperatures or dormant life stages [18]. Three phases can be distinguished in the pattern, and are described in more detail in the following paragraphs.

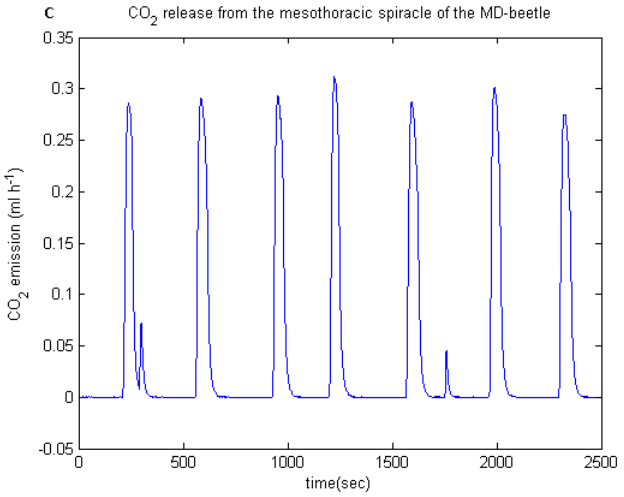

FIGURE 1.3: CO_2 release of a dung beetle at room temperature. The three *DGC* phases are shown. Unpublished data from F.D. Duncan.

The classical pattern of *DGC* consists of three phases [22, 25, 27]:

1. Closed phase (C)**:** This phase begins when the spiracles are tightly closed and the insect is essentially hermetically sealed [7, 9]. Respiration occurs here and is driven by the oxygen stored in the cells. The oxygen partial pressure (p_{O_2}) within the trachea declines according to the metabolic rate and the compliance of the tracheal system [20]. CO_2 is buffered chemically in the hemolymph during this phase and thus the partial pressure of carbon-dioxide (p_{CO_2}) increases. Owing to the high solubility of CO_2, the increase in p_{CO_2} in the air within the trachea is less than the decline in p_{O_2}. As a result, total atmospheric pressure in the tracheal lumina declines slightly during the closed phase [24]. After some time, the O_2 partial pressure

reaches a threshold which triggers spiracle opening [19]. The closed phase ends and moves into the flutter phase.

2. Flutter phase (F)**:** The spiracles begin to flutter, allowing a bulk of air down this pressure gradient. Inward convection is an important mean of restricting outward water movement [26, 27]. Here, convective influx of oxygen rich-air into the tracheal system allows O_2 uptake matching metabolic demand now with minimal water-loss. Throughout the whole flutter phase, the endotracheal p_{O_2} is regulated to values near the triggering threshold [24, 27]. CO_2 continues to accumulate during this phase.

3. Open or burst phase (O)**:** As the p_{CO_2} still increases during the flutter phase, eventually a threshold of CO_2 is reached [19] and the spiracles open. During this phase, the spiracles remain fully open and the gases are exchanged with the atmosphere. Oxygen gain and carbon dioxide loss occurs during this period [28]. p_{O_2} and p_{CO_2} tend towards levels present in the external atmosphere due to diffusion of these gases down their concentration gradients through the trachea and open spiracles [24, 29]. This phase is important because water loss is high as long as the spiracles remain open [7–9].

The significance of DGC**:** The adaptive significance of DGC in insects is a subject of considerable debate. The paradigm that DGC is an adaptation to reduce respiratory water-loss has been challenged since several studies reveal that respiratory water-loss comprises $< 15\%$ of total water-loss, even when the spiracles are open [22]. Three main adaptive hypotheses have emerged to explain this behaviour.

- Hygric hypothesis: This hypothesis states that $DGCs$ are an adaptation to reduce respiratory water-loss [27].
- Chthonic-hygric hypothesis: This hypothesis suggests that DGC may have evolved in underground insects as a way of dealing with hypoxic or hypercapnic conditions such that a water-loss penalty is not paid [22, 31].
- Oxidative-damage hypothesis: This hypothesis suggests that $DGCs$ are an adaptation that serves to reduce the supply of oxygen to the tissues during periods when the metabolic rate is low [32].

Each of the hypotheses makes firm predictions concerning the relationship between the duration of $DGCs$ and ambient temperature (T_E), saturation deficit, P_{O_2} or some combination thereof [31]. The underlying result behind all three hypotheses is that $DGCs$ of insects reduces respiratory water-loss while ensuring adequate gas exchange.

External and internal factors influencing DGC**:**

Several factors have been identified that are necessary for *DGC*. Note that, not all insects use *DGC* [25].

- *DGC* is typical of resting insects. The discontinuous pattern vanishes once the insect becomes active and is replaced by continuous gas exchange to meet increased metabolic need.
- *DGC* might solely be a result of control that faces a change in metabolic rate [33]. For instance, if temperature is modified, a systematic change in *DGC* pattern occurs.

1.3 Rhythmic tracheal wall contractions

Insect respiratory gas exchange involves both convective and diffusive transport modes, with convection a result of internal pressure gradients that are responsible for producing or enhancing both directed and tidal airflows [122]. Westneat et al. [47] first described rhythmic wall contractions observed at multiple locations in insect tracheal tubes. These abdominal contractions are hypothesized to induce changes in the insect's hemolymph pressure. Changes in hemolymph pressure are hypothesized to produce multiple rhythmic tracheal wall contractions which in turn are hypothesized to produce changes in the internal tracheal tube pressure [123]. The contractions are believed to be the main driving mechanism that delivers and transports air efficiently to every cell [47, 49, 123].

Synchrotron X-ray imaging has been used in recent studies to visualize insect respiratory systems. Images of ground beetle respiratory systems have revealed that the tracheal tubing network undergoes periodic localized collapses and re-inflations [47–49, 61]. These motions are known as rhythmic compressions and are believed to be the driving force for transporting airflow where diffusion becomes insufficient [47, 48]. Socha et al. [49] presented X-ray videos showing kinematics of the tracheal compressions. The compressions undergo a collapse region then followed by re-inflation region. Figure 4.1 shows the complex tracheal network X-ray image. A summary of the tracheal structure is given in Socha et al. [49, 61]. X-ray images show rapid cycles of tracheal compression and expansion which are parallel to inflation and deflation of the human lung system. This observation further supports arguments presented in Chapter 3 where a parallel analysis to the human lung system is presented. In Chapter 4, a mathematical model that describes flow motions of these contractions is developed.

1.4 Tracheal wall contractions induced flow transport

To the best of my knowledge, very little has been reported experimentally on the relationship between observed wall contractions and net flow. The geometric and spatial configurations of rhythmic contractions and their effect on net flow in tracheal networks is not fully understood. However, there have been theoretical attempts aimed at determining this relationship [49, 133, 135]. Fluid transport in microscopic tubes can either be induced by stationery (non-propagative) contractions or by longitudinal traveling waves generated by these wall contractions (propagative contractions).

Non-Propagative flow transport: Macagno and Christensen [119, 120] described how stationery contractions are generated. They argued that although these contractions are observed in many physiological systems, the flow transport by this class of wall motions is not fully understood. Contractions from this class of wall motions assume that all wall successive movements are in the lateral direction only over a finite length (see figure 1.4(a)).

With analysis adopted from literature, this thesis considers flow transport in the trachea assuming the contractions observed are non-propagative. Chapter 4 describes this flow transport model. In Chapter 7, flow transport is considered in the absence of contraction and assuming that the insect is hermetically sealed.

Propagative flow transport: Figure 1.4(b) shows the case of propagative waves. Propagative flow transport, also known as peristaltic flow, can be attributed to smooth progressive muscle contractions-expansions. Peristaltic flows can be found in many biological flows such as urinal transport and blood pumping. This flow transport has been extensively discussed in the literature and there are several models proposed to explain this phenomenon (see [118]). Tube length, wave form, wave shape and Reynolds number approximations have all been presented in detail in literature (see [118, 121]). Results on propagative waves suggest that triangular wave forms had the worst performance while rectangular wave forms produced maximum pressure gradient [121]. Thus, the shape of the wave plays an important role for efficient propagative flows. Although the shape and form of the waves that propagate in flexible tubes are not known a priori, some researchers have presented estimates of net flow induced by these waves. Li and Brausser [118] pioneered the modeling of progressive contractions over a finite length tube for an arbitrary wave shape and wave number using lubrication theory.

1.5 End diffusion

The primary goals of the insect respiratory system are to deliver oxygen from the air to the tissues and to transport carbon dioxide from the tissues to air. Upon entering the trachea through

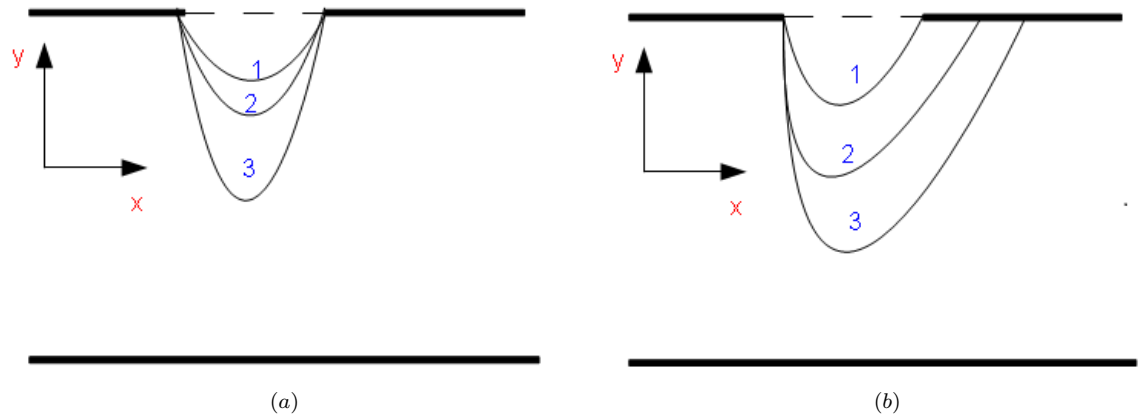

(*a*) (*b*)

FIGURE 1.4: (a) Propagative and (b) Non-propagative contractions.

the spiracles, air is transported by diffusion and convection to the tracheoles, each less than 1 μm in diameter [59, 60]. The tracheoles provide a thin, moist interface for the exchange of gases between atmospheric air and a living cell. The terminal ends of the tracheoles are often filled with interstitial fluid [13, 50]. Evidence suggests that there is no difference in the permeability of larger trachea or tracheoles to oxygen, but only tracheoles are close enough to mitochondria for O_2 to diffuse to the mitochondria in quantities needed [59]. Oxygen first dissolves in the liquid of the tracheole and must then move across the tracheal walls, across the plasma membranes of the adjacent cells, the cytoplasm and finally through mitochondrial membranes [59]. The tracheoles are the main site of gas exchange with tissues; they closely surround and might even penetrate the tissues to become intimately associated with individual cells and to lie close to mitochondria [46, 59, 64]. Carbon dioxide is produced during cellular respiration and moves in the opposite direction from the respiring cells to the trachea against concentration gradients. Increased ionic strength or acidification of the interstitial fluid withdraws fluid from the tracheoles, facilitating gas exchange during activity or varying oxygen partial pressures. The structure and layout of the cells suspended in the hemolymph is shown in figure 3.1.

1.6 Literature reviews

This section discusses previous research that has attempted to model simultaneous movement of gases across confined spaces, end diffusion, flow transport by moving wall actions and microscale compressible flows.

1.6.1 Modelling review

Studies of gas movement across the insect spiracles have been carried out in detail focusing on partial pressure differences as the driving force for gas exchange. Insect respiratory research groups have been divided into two [9]; one group focus on gas exchange and water balance, and the other group focuses on the sites of resistance to gas exchange and gas transport. Research described in this thesis intersects these paths.

Microscale incompressible flow: Several studies have been carried out to understand complex and unsteady transport within collapsible tubes. Uchida and Aoki [126] presented a similarity solution for unsteady viscous flow in a semi-infinite pipe with either contractions or expansions. The solution presented is general and valid when the radius of the pipe is uniformly collapsed or fully collapsed. Secomb [127] presented a two dimensional flow field for incompressible viscous flow in infinitely long channels induced by prescribed pulsatile and sinusoidal wall motions with small amplitudes. Further, Singh et al. [129] presented a generic approach to studying a squeezing flow problem between parallel plates using a similarity transformation to reduce the Navier-Stokes equations to a nonlinear ordinary differential equation that can easily be solved numerically.

Theoretical models describing channel flows with localized contractions are somewhat more involved. The pioneering work by Macagno and Christensen [119, 120] laid a foundation for the current study on incompressible viscous flow. They quantified peristaltic flow in the human duodenum. In their review, supported by a theoretical analysis, they concluded that at least two stationery contractions were required to produce net flow. Recently, Aboelkassem et al. [135] also presented an analytic solution for fluid flow in channels with localized contractions. In their review, they also concluded that at least two contractions were required to produce net flow. They also observed that the contractions should move with a slight time lag to produce this flow. Westneat et al. [47] and Socha et al. [49] also described other physiological systems with localized wall contractions. A theoretical analysis of flow along a channel with time dependent indentation assigned to one wall was presented by Ralph and Pedley [131]. The solutions presented were for different values of observed Reynolds numbers. Mahmood and Merkin [132] presented a simplified analysis of flow in a narrow duct with indentation given on one side wall. Aboelkassem and Staples [133] modelled this particular work with a no-slip boundary condition in the tracheal walls.

The work presented in Chapter 4 is more related to the problem of localized wall contraction induced flow in microtubes than any of the previous cited examples. A marked distinction between the reviewed work and the work presented in this thesis is that the tracheal tube wall contractions are localized and independent, unlike the uniform wall deformation being fixed in time. A distinction between the work presented in this thesis and that of Aboelkassen

and Staples [122, 133] and Aboelkassen et al. [135] is that the tracheal wall contractions are independent, do not recall previous positions (do not recall their contraction history) and slip boundary conditions are assumed. Further, the effects of slip conditions on the time-averaged net flow are shown. Lubrication theory [138] is used to model propagative flow of wavy contractions over a finite length tube. Rhythmic wall contractions observed by Socha et al. [49] motivated this particular study in Chapter 4.

Microscale gaseous slip flow: Chapter 7 considers gaseous slip flow during the closed spiracle phase. Gas flow in microchannels has been studied extensively in the literature in the rarefied gas community. Significant previous studies of gaseous flows in microchannels have been conducted by Cai and Wang [82], Arkilic *et al.* [114, 115], Pong et al. [147], Beskok and Karniadakis [149] and Peikos and Breuer [154]. Studies of compressible flow without the incorporation of rarefied gas behaviour has been conducted by Prud'homme et al. [150]. Their perturbation solution of the Navier-Stokes equations for radially symmetric geometries, without the inclusion of rarefaction effects, does show the significance of gas compressibility on the pressure distribution. Van den Berg *et al* [152] also presented a $1D$ perturbation analysis of radially symmetric flow without inclusion of rarefaction effects.

Harley et al. [153] studied gas flow in $2D$ microchannels for various Knudsen numbers. Their model assumed negligible wall-normal pressure gradients and was based on the Navier-Stokes streamwise momentum equation, with nonlinear terms neglected. Results of this study demonstrated the existence of nonzero wall velocities in microchannels and showed the contribution of slip to the mass-flow pressure-drop relationship. Resulting microfluidic channels designed from this setup did not posses well-controlled surface structure and the technique used to characterize mass flow was susceptible to thermal fluctuations [114]. Arkilic et al. [114, 115] showed the effects of wall slip on mass-flow pressure-drop relationships in $2D$ microchannels with uniform surface structure. Experimental investigations into the pressure distribution that exists in microchannel flows have also been carried out by Arkilic et al. [114, 115] and Pong et al. [147]. These results have also shown empirically that compressibility is an important feature in a microchannel. Over and above this, simulations of rarefied gas behaviour in microchannel flow were carried out by Beskok and Karniadakis [149], and Peikos and Breuer [154]. Results show that mass flow within microchannels can be increased by both slip and thermal effects.

By studying compressible flow when the spiracles are completely sealed, estimates of the Reynolds and Mach numbers at the tube terminal ends where the tracheoles directly deliver oxygen to the cells are obtained. Likewise, in an attempt towards solution, a quasi-steady model is derived using $2D$ Navier-Stokes equations with slip boundary conditions for compressible flow, ignoring body forces. The possibility of using this channel configuration as a microscale fluid transport mechanism is explored. The present work on microscale gaseous slip flow is an extension of the work of Arkilic et al. [114], which is extended to include quasi-isothermal flow condition with

appropriate determination of flow parameters, and to consider temperature effects on net flow. Temperature considerations arise from the fact that heat conduction can be quite significant because the tubes under consideration have tiny dimensions of height. In this case, temperature gradients can be large even with small temperature variations.

Flexible tracheal system: Numerous experiments have revealed complex interactions between the respiratory and circulatory systems in insects. Chapter 3, considers the structure of the tracheal system and its role in mass net flow. Some examples of such interactions are synchronization between spiracle opening and mass flow rate [50], changes in spiracle opening patterns due to changes in metabolic activity [58] and oxidative tissue damage due to prolonged exposure to oxygen [24]. These interactions are not fully understood and thus provide a motivation for developing these models in Chapter 3.

In the past, gas exchange in the trachea has been modelled from different perspectives and at different levels of detail. The simplest models assume that the diffusive and chemical processes involved in oxygen uptake and carbon dioxide release are in equilibrium by the time the gas diffuses from the tracheoles to the point where it attaches to the mitochondria, and vice-versa. The simple models are used when considering spiracle control and mass flow (see [19, 50, 51, 57]). Detailed studies of chemical and diffusive processes at the tracheole and respiring cell interface have been carried (see [13, 50, 59, 60]). However these studies do not assume equilibria of the diffusive and chemical processes that involve carbon dioxide.

There are different sources of interaction between spiracles and the tracheal system in insects. The work presented in Chapter 3, is concerned with the interactions via the gas exchange process. The gas exchange process is considered as the control system where the hemolymph pressure and net flow are the control variables and the partial pressure of oxygen and carbon dioxide are the measured variables. Unlike previous studies, this thesis regards body tissues as another compartment to store oxygen. Thus, it is shown that gas exchange at tissue level and time delay due to differences in diffusion capacities are then an important part of the mathematical modelling. The consumption of oxygen and the rate of carbon dioxide production in respiring cells are viewed as disturbances to the system. The disturbances are considered implicitly via the respiring cell's partial pressures of oxygen and carbon dioxide. To the best of my knowledge, existing modelling efforts have not described a model for gas exchange at the tracheoles and oxygen uptake by mitochondria.

The primary goal of this study is to explore how respiratory gases are distributed in the insect from the initial point when they enter through the spiracles right to the point where oxygen is used up for metabolism and carbon dioxide is produced. Mainly, I explore how respiratory gases are transported in the tracheal network due to observed tracheal wall collapses. The idea of using a tube with two collapsing sites that move with a time lag as a microscale pumping mechanism is considered. The pumping model is derived from steady Navier-Stokes equations that are then

derived analytically following lubrication theory. The analytical derivation relies mainly on the assumption of using quick contraction movements where the wall history is neglected. The net flow is thus assumed to depend on the wall motion. Although the unsteadiness effect is omitted from the governing equations, the time dependence effect is introduced via a series of steady wall motions. The models presented are accurate to the assumptions made. There may be accumulated errors due to these assumptions, but the qualitative nature of the flow will not be altered.

1.6.2 Differential Transform Method (DTM) review

The differential transform method (DTM) is a numerical method based on a Taylor series expansion. It is an iterative procedure that is described by transformed equations of original functions for solutions of differential equations [100, 101]. This method constructs an analytical solution in the form of a polynomial [102]. Unlike the high order Taylor series method which requires many symbolic computations, the DTM is an iterative procedure to obtain Taylor series solutions. Advantages of this DTM include less computation time when applied to nonlinear systems, few symbolic computations and that an analytic solution in the form of a polynomial is obtained [102]. Solutions of nonlinear ordinary differential equations ($ODEs$) have been constructed using DTM. Two dimensional DTM has been applied by Jafari et al. [103] to solve nonlinear gas dynamics and Klein-Gordon equations. Ndlovu and Moitsheki [104] applied 2D DTM to a heat conduction problem for heat transfer in longitudinal rectangular fins. Their results indicated that the solutions obtained by DTM are reliable, useful and that DTM was an effective method for decoupling partial differential equations ($PDEs$).

Aboelkassen and Staples [134] presented Stokelets-meshfree computations based on the method of fundamental solution (MFS) to study transport in a 2D microchannel with moving dynamic collapses. MFS is considered to be an efficient numerical technique for solving an elliptic class of boundary value problems (BVP) with moving boundaries. Although MFS is relatively easy to implement and does not require any computational grid, it still has functional drawbacks related to non-invertible or ill-conditioning matrix problems associated with determining force coefficients [134]. This drawback can lead to inaccurate force coefficients and consequently incorrect flow fields [134]. The 2D DTM is adopted to provide semi-analytical solutions for fluid transport in 2D channels with rhythmic contractions. The derived analytical solutions are validated numerically using DTM for the steady Navier-Stokes equations. The analytic solutions are said to be exact while those from DTM are said to be semi-analytic.

1.7 Thesis statement and outline

The simultaneous movement of respiratory gases across the insect tracheoles, movement of respiratory gases within a flexible trachea and the efficient transport of fluids within a network of channels are challenging problems and of importance in many scientific applications. For instance, microfluidic devices and microelectromechanical systems (MEMS) inspired by these physiological systems in insects have in recent years gained attention. Microfluidic devices, MEMS and their environments are typically of the order of microns. Microfuidic devices are normally composed of multiple tiny branches that usually move, mix or separate fluids in drug delivery, cell manipulations, DNA chips and inkjet printheads. These applications are usually carried out via transporting of microlitre amounts of fluids in a directional and controlled manner from one site to another.

In this thesis, attempts are made to answer the following questions: How do respiratory gases manage to move in opposite directions simultaneously across the insect spiracles and how does extended spiracle opening influence the influx of gases into the trachea. Upon entering the trachea, respiratory gases are transported to the tips of the tracheoles where gas exchange with tissues occurs. The thesis proposes novel paradigms by which oxygen is transported and absorbed by respiring cells at the tracheole tips. The phenomenon by which carbon dioxide is removed from respiring cells via the tracheal network is derived. Lastly, inspired by insect rhythmic tracheal compressions, novel paradigms which trace microscale fluid flow in the tracheal network are proposed. One model traces fluid flow during the open spiracle phase while another model traces compressible gas flow during the closed spiracle phase. The insect inspired models can be useful in engineering where insect physiological systems are mimicked to design efficient microfluidic devices. In simple tube geometries, the results presented are expected to function efficiently in the microscale flow regime. Theoretical analysis is used to obtain most of the results presented throughout this research work.

An outline of the thesis is as follows:

- In Chapter 1, a brief overview of the insect respiratory system is given. The theory behind the movement of the respiratory gases through the insect spiracles is explained. Discussions related to various gas flow transport mechanisms and lists of related previous work are given.
- In Chapter 2, the dynamics of respiratory gases interaction accompanied by the loss of water through the insect spiracle are given. The interactions are analyzed by deriving a system of ordinary differential equations that traces the simultaneous movement of gases across the insect spiracles.

- In Chapter 3, models for the movement of respiratory gases in a rigid, flexible and flexible trachea with gas exchange are presented. The models presented address spiracle behaviour on net flow of the respiratory gases, cellular respiration and tissue absorption, and global gas movement within the insect.
- In Chapter 4, a novel bioinspired pumping paradigm tracing flow motion in confined domains namely the trachea and tracheoles with moving non-propagative, non-peristaltic wall contractions is presented. The presented model is inspired by rhythmic tracheal wall contractions observed by using synchrotron X-ray imaging when the insect is at rest.
- In Chapter 5, the global minima based constrained optimization technique is used to optimize the derived tracheal pumping models for efficient net flow. The optimal spatial and temporal parameters of the models derived in Chapter 4 are presented for a flexible trachea with moving wall contractions.
- In Chapter 6, the Differential Transform Method, a numerical method based on Taylor series expansion, is presented to validate the model derived in Chapter 3 for movement of respiratory gases in the insect trachea.
- In Chapter 7, a new compressible gas flow transport protocol through the tracheal system during the closed spiracle phase is presented. The concept presented allows the respiratory gases to be transported and controlled in the tracheal network branches.
- In Chapter 8, conclusions and future work are presented.

Chapter 2

Dynamics of the oxygen, carbon dioxide and water interaction across the insect spiracle

The work in this chapter appeared in: *Simelane, S.M., Abelman, S., and Duncan, F.D, 2014. Dynamics of oxygen, carbon dioxide, and water interaction across the insect spiracle. Abstract and Applied Analysis.* ***157573*** *(11pp).*

This chapter explores the dynamics of respiratory gases interactions which are accompanied by the loss of water through an insect's spiracle. Here we investigate and analyze this interaction by deriving a system of ordinary differential equations for oxygen, carbon dioxide and water vapor. The analysis is carried out in continuous time. The purpose of the research is to determine bounds for the gas volumes and to discuss the complexity and stability of the equilibria. Numerical simulations also demonstrate the dynamics of our model utilizing the new conditions for stability and instability.

2.1 Introduction

The Lotka-Volterra equations have been used as a basis for many types of models that involve the interactions of different populations (see [1–3]), mostly the interaction of two populations. Other extensions and modifications such as diffusion, ratio dependence and functional response have been added to the Lotka-Volterra equations to gain an even better and deeper understanding of the dynamics of population interactions [2, 4, 5]. The model discussed in this paper is also based on the simple Lotka-Volterra model developed by Manson and Lundberg [6]. In predator-prey models, both the predator and prey are being born, the predator feeds on its prey and

the predator dies at some point. In a sense O_2 and CO_2 are being born and die. O_2 is born when it enters the trachea and starts to die as it is used by the cells. O_2 is replaced by CO_2. This is just the same way in that if there is sufficient prey the predator population expands at the expense of the prey. So CO_2 increases as O_2 is consumed and the point is reached when the populations need to be stable; this is when the spiracle opens and we now have the cycle reversing. Just the same way as the classical predator-prey model has an increase in prey then a delayed increase in predators which causes a decrease in prey and then a decrease in the predators and it cycles, so too do the O_2 and CO_2 in the insect trachea. The motivation behind this is that the model presented here is a competing species model in that the respiratory gases, oxygen and carbon dioxide, are competing for space in the trachea and there is a maximum spiracle area through which the gases can pass. When the spiracle opens for gas exchange, the gases manage to move in opposite directions simultaneous. Thus on the opening of the spiracle, O_2 needs to be replaced and CO_2 needs to exit through the same area. This analysis prompted us to consider any existing competing species model to try and explain the gases movement. The simple competing predator-prey model provides a starting point for our argument.

Studies of gas exchange through the insect tracheal system have been carried out in detail (see [7, 8] for reviews) focusing on partial pressure differences as the driving force for gas exchange. Individuals attempting to quantify gas exchange in insects have been divided into two groups according to Snyder et al. [9]. One group is interested in insect physiology and focuses on gas exchange and the relationship between gas exchange and water balance [8–11]. Several models have been developed for predicting respiratory water loss as a consequence of the opening of the spiracles (see [12, 13]. The other group interested in respiratory physiology focused on the sites of resistance to gas exchange, attempting to determine as to where resistance lies and if gas exchange occurs entirely by diffusion or convection [7, 9, 14].

Cockroaches and locusts inhale air through the anterior spiracles and exhale through the more posterior spiracles [21]. Thus the co-ordinated action of spiracles can direct air flow through an insect. Insects are also known to close their spiracles for periods of time resulting in no gas exchange taking place. The intermittent opening and closing of spiracles is referred to as discontinuous gas exchange (DGC) [22]. The species used for this study is a flightless dung beetle, which uses a single spiracle for gas exchange at rest [52].

The purpose of this paper is to analyze and demonstrate the dynamics of various gases in our model system by

1. determining ultimate bounds for the interacting gas volumes.
2. exploring the stability and instability of the equilibrium equations.
3. obtaining numerical simulations for the pattern of the dynamics for the interacting gases.

In our research, we present a mathematical model that captures how the respiratory gases manage to move in opposite directions simultaneously. The model should be applicable to terrestrial insects under any environmental conditions to trace the DGC, cyclic and continuous gas flux. It should answer questions such as: how do respiratory gases manage to move in opposite directions simultaneously? How does extended spiracle opening influence the influx of the gases? What factors are responsible for instability of the system? To answer all the above questions, we need to study the dynamical behaviour of the system and test it with experimental data.

In section 2.2, the discontinuous gas exchange across the insect spiracles is summarized. In the third section, the model assumptions and the system model are presented. Primary results for the model and boundedness properties for the respiratory gases are given in the fourth section. The analysis of equilibrium solutions is also undertaken along with conditions that ensure non-negativity of the equilibrium solutions in section 2.5. Asymptotic stability and instability for the five equilibrium solutions are determined through linearization. In the sixth section, graphical display for the dynamics and pattern of the gas volumes is shown by utilizing the conditions for stability and instability. Finally in section 2.7, we summarize our findings and explain how the conclusions are made.

2.2 Gas exchange in insects

Many beetles living in arid areas are flightless and have a subelytral cavity. The dung beetle is wingless and has a sealed air-space called the subelytral cavity beneath the wing covers (Fig. 2.1). Dung beetles have only one pair of spiracles in the head region and have 7 pairs of spiracles in the body region. The 7 pairs of spiracles open into the subelytral cavity and are all positioned under the elytra. The spiracles are the sites of gas exchange.

Gas exchange in insects is a continual conflict between the need to support aerobic need and the need to reduce respiratory water loss [7, 9, 11]. The respiratory system of insects consists of a highly branched system of cuticle-lined tubes extending throughout the body. The tubes are filled with air, which greatly facilitates the transport of gases through the body [24]. The trachea opens to the external atmosphere through valve-like spiracles on the surface of the abdomen and thorax. The principal sites for gas exchange are the fine branches (less than a micro-meter in diameter) at the tip of the tracheal system, internal to the spiracles [24]. Insects loose water through the cuticle and through the open spiracles, with respiratory water loss contributing a small proportion of the overall water loss in most insect species [22].

Many insects exchange respiratory gases with the atmosphere discontinuously, thus permitting gas exchange while minimizing water loss despite their relatively high metabolic rates. While

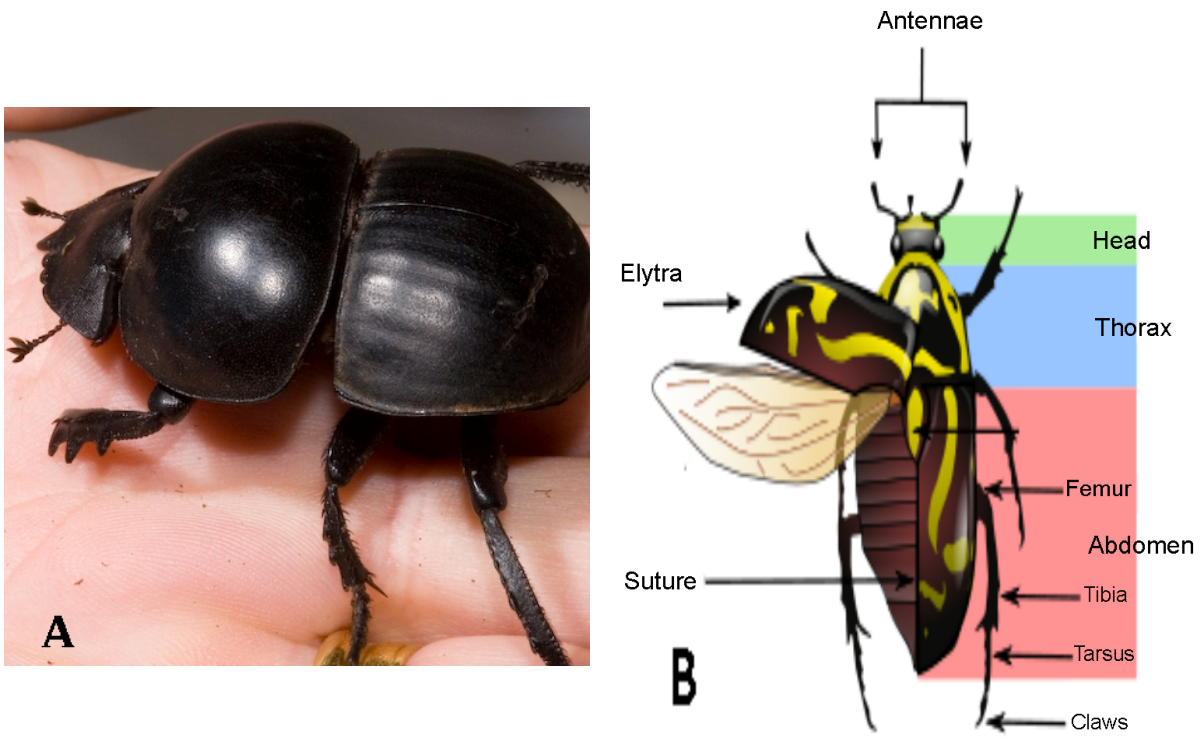

FIGURE 2.1: Summary figure showing two beetles: (A). Shows a dung beetle (Photo: F.D. Duncan) and (B). shows the typical morphology of a beetle (see [23]).

oxygen consumption and carbon dioxide production are continuous, the external elimination of gases is discontinuous [9, 24]. The classical pattern of *DGC* consists of three phases [22, 25, 27]; also observed in the beetle used for this study.

1. *Closed spiracle phase* $(C - phase)$

This phase begins when the spiracles are tightly closed and the insect is essentially hermetically sealed [7, 9]. Respiration occurs here and is driven by the oxygen stores in the cells. The oxygen partial pressure (P_{O_2}) within the trachea declines and the partial pressure of carbon dioxide (P_{CO_2}) increases. Owing to the high solubility of CO_2, the increase in P_{CO_2} in the air within the trachea is less than the decline in P_{O_2}. As a result, total atmospheric pressure in the tracheal lumina declines slightly during the closed phase [24].

2. *Flutter phase* $(F - phase)$

The spiracles begin to flutter, allowing large quantities of air down this pressure gradient. Inward convection during the $F - phase$ is an important means of restricting outward water movement

[26, 27]. Here, convective influx of oxygen rich air into the tracheal system allows O_2 uptake with minimal water loss. CO_2 continues to accumulate throughout the $F - phase$ period.

3. *Open spiracle phase* $(O - phase)$

During this phase, the spiracles remain fully opened and the gases are exchanged with the atmosphere. Oxygen gain and carbon dioxide loss happens during this time [28]. P_{O_2} and P_{CO_2} tend towards levels present in the external atmosphere due to the diffusion of these gases down their concentration gradients through the trachea and open spiracles [24, 29]. This phase is important because water loss is high as long as the spiracles remain open [7–9].

In the following sections, we develop and analyze a model for the respiratory gases dynamics that considers the discontinuous exchange of these gases. The model includes all of the above features.

2.3 The model system

Internally within an insect, oxygen is taken into the cells and through the process of cellular respiration carbon dioxide is produced as a waste product. In insects, this CO_2 is stored in the tissues and haemolymph (similar to blood in vertebrates). When this storage is saturated the CO_2 enters the trachea (hollow tubes) in order to be expelled to the exterior of the insect. Air enters and leaves the insect through the spiracles, which are the opening of the trachea tube to the exterior.

In insects using DGC the spiracles are closed while the O_2 is being used by the cells and CO_2 is stored. When there is sufficient build-up of CO_2, this increase in CO_2 concentration causes the spiracles to open. Upon opening CO_2 rushes out of the tracheal system and O_2 rushes in. Both these gases and water vapor have to leave or enter through the small spiracle opening. Thus these gases are competing for space [7].

The model presented looks at the movement of the respiratory gases across the spiracle opening, across the tracheal system. We consider the standard predator-prey model which consists of two non-linear ordinary differential equations (see [1–6] for reviews). We extend this model to include a third non-linear differential equation, hence a system of three non-linear ordinary equations. We assume there are three components; (i). Oxygen denoted by O_2, (ii). Carbon dioxide denoted by CO_2, and (iii). Water vapor denoted by H_2O.

Predator-prey models are an essential tool in mathematical modeling and for our understanding of interacting species in the natural environment. A better description of this model is a

competing species model. Thus throughout the paper we will refer to a competing species model. Traditional predator-prey models are based on the principle of mass action. The mass action principle predicts that the rate at which an individual predator consumes prey should depend only on prey density. In applying the mass action principle there is also the implicit assumption that the system is well mixed so that inhomogeneities do not develop. In developing our model of the gas interaction, the principle of mass action was the main driving principle. The rate at which respiring cells take in oxygen depends on the oxygen density in the trachea. This parallel analysis prompted the use of basic predator-prey models in an attempt to trace the movement of the respiratory gases. Assumptions in building the competing species model:

1. If one gas is moving, the rate of change of the gas follows a logistic model (model with tracheal size threshold).

2. The rate of change of each gas decreases at a rate proportional to the amount of gas flow (competition).

These assumptions are reasonable because when the spiracle opens, the rate of change of oxygen growth is an accelerating function of oxygen until atmospheric pressure is reached. Again, the rate of change of oxygen once the spiracle closes decreases at a rate proportional to the amount of oxygen used up for respiration and thus carbon dioxide production.

Many models that trace the movement of respiratory gases exist in the literature. These models are based on both Fick's laws of diffusion, which uses the fact that most insects use both convective and diffusive exchanges. For instance, Welch and Tracy [12] developed a model of convective gas flux as a function of the total gas, the inspired and expired fractions of the gases. Even though the model is widely accepted, it ignores known complications to insect physiologists. This includes the effects of end diffusion, interference between adjacent respiratory tubes, and interactions between water vapor leaving and gas entering through the tubes. It also fails to address the fact that carbon dioxide elimination takes longer than the ingress of oxygen.

The failure of the existing models to provide generality and unification because of their taxon-specific design prompted us to develop a novel general model. The assumptions in our model derivation are analogous to those in predator-prey models. With these assumptions, we develop a ratio dependent model and derive a model for oxygen-carbon dioxide interactions with ratio dependent interaction rate. Ratio-dependent functional response is a better starting point for modeling population dynamics. There is a legitimate predictive use of ratio-dependent models in the literature (see [34–37] for reviews). Evidence suggests that even when functional responses are measured in the short term, they are closer to ratio-dependent than prey dependent. This is supported by the argument that on a periodic time scale, the surrounding cells limit each other's oxygen supply through sharing (i.e when oxygen is in short supply during the $C-phase$).

Berryman [38] developed a ratio dependent model by extending the logistic growth model. The new model is developed by extending Berryman's [38] model (see [38–41]). Here, the oxygen intake by the respiring cells, i, is described by

$$i = \frac{a}{1 + b(CO_2/O_2)}, \tag{2.1}$$

where CO_2 is the carbon dioxide volume, O_2 is the oxygen volume, a the amount of O_2 taken in by the respiring cell when O_2 is in excess, and b is the saturating factor deciding how quickly the respiring cells intake decelerates as oxygen density decreases in the trachea.

It follows from equation 2.1 that the risk of being used by a respiring cell for each unit of oxygen is

$$\frac{a(CO_2/O_2)}{1 + b(CO_2/O_2)}, \tag{2.2}$$

where CO_2/O_2 is the respiratory quotient.

Now, we assume that the carbon dioxide elimination rate is a function of oxygen intake rate, i. Thus, the CO_2 production and elimination functions are respectively:

$$\frac{ci}{1 + gi} \quad \text{and} \quad d_{maxCO_2} - \delta_{CO_2} i, \tag{2.3}$$

where c measures how the cells turn the inspired oxygen into carbon dioxide, g how carbon dioxide production is physiologically constrained by these cells, d_{maxCO_2} measures carbon dioxide maximum per capita elimination rate, and δ_{CO_2} adjusts carbon dioxide elimination rate proportionality to the respiring cell intake rate. We model the cell's carbon dioxide production rate as a non-linear increasing function of oxygen intake rate while the elimination rate is a linearly decreasing function. The non-linearity of the carbon dioxide production function reflects a physiological constraint on the rate of new carbon dioxide. It involves trade-offs with for instance cell growth and is likely to be limited since the quantities of carbon dioxide are finite. Note that the CO_2 elimination could be modeled as any kind of decreasing function of intake, but for simplicity we used a linear function.

The following differential equations model the dynamics of the gas volumes:

$$\frac{dO_2}{dt} = uO_2\left(1 - \frac{O_2 + CO_2}{K}\right) - a\frac{O_2CO_2}{O_2 + bCO_2}, \tag{2.4}$$

$$\frac{dH_2O}{dt} = fH_2O - e\frac{CO_2H_2O}{H_2O + h} - sH_2O, \tag{2.5}$$

$$\frac{dCO_2}{dt} = ac\frac{O_2CO_2}{O_2(1 + ga) + bCO_2} - d_{maxCO_2}CO_2 + \delta_{CO_2}\frac{aO_2CO_2}{O_2 + bCO_2}. \tag{2.6}$$

with $u, a, b, c, e, f, g, s, K > 0$.

O_2, CO_2 and H_2O denote the non-negative gas and moisture volumes, respectively. u is the oxygen ingress rate at low oxygen densities, K is the tracheal carrying capacity of the oxygen gas, e maximum spiracular water loss in the thorax and elytral case as a result of the insect respiration, f is the water ingress rate into the trachea and h is the water density/volume where water loss is half saturated. Lastly, s is the rate of water loss due to other forms of water loss besides through the spiracular openings.

In the system modeled here, the mean surface area of the spiracle, trachea and respiratory cells affect both oxygen intake, carbon dioxide production and water loss. Worth noting is the fact that these affect carbon dioxide production only indirectly. Hence, the carrying capacity may be defined as a function of the spiracle size, tracheal length and the respiring cell's size. This would mean that the trachea can sustain more oxygen when airflow (air-supply) is higher. In addition, for a given density, oxygen intake rate is higher when the size of both the cells and spiracle is larger. We then define the carrying capacity K as

$$K = \frac{i\Psi}{1 + m\Psi}, \tag{2.7}$$

where Ψ is mean surface area of the spiracle, trachea and cells, i here governs how K increases with Ψ during the different phases of DGC. To allow for other limiting factors such as the ambient temperature, humidity, spiracle location and body size, we do not let K grow indefinitely with Ψ. Instead, the size of m decides how K is limited due to the constraints of these factors.

Ratio dependence, as opposed to dependence on total size of Ψ, is a mechanistic way of modeling oxygen intake in that a unit of oxygen is affected by the amount of oxygen molecules surrounding it through sharing the navigation space. This model for oxygen is captured in our system. To simplify the model, we allow the respiring cells to take up only new oxygen as only a very small volume of O_2 remains in the trachea from the previous inhalation.

2.4 Ultimate bounds for the gas volumes

The following comparison argument [42] is employed in the proofs associated with the boundedness of the gas volumes. Consider the respective solutions ν_1, ν_2 and ν_3 of the initial value problem

$$\nu_j' = \Phi_j(t, \nu_j) \quad \text{in} \quad (0, T), \quad \nu_j(0) = \nu_{j,0}. \tag{2.8}$$

where $j = 1, 2, 3$. Φ_1, Φ_2 and Φ_3 are continuous in $[0, T] \times R$. We have,

Lemma 2.4.1. The comparison argument. Assume that $\partial\Phi_1/\partial t$, $\partial\Phi_2/\partial t$ and $\partial\Phi_3/\partial t$ are continuous in $[0, T] \times R$. Comparing any two, if $\Phi_1(t, \nu) \leq \Phi_2(t, \nu)$ in $(0, T] \times R$ and $\nu_{1,0} \leq \nu_{2,0}$, then the respective solutions ν_1 and ν_2 of equation 2.8 satisfy $\nu_1(t) \leq \nu_2(t)$ on $[0, T]$.

Note that the comparison of $\Phi_2(t,\nu) \leq \Phi_3(t,\nu)$ follows as above.

Theorem 2.4.2. *The amount of oxygen, O_2, in our model system satisfies:*

$$\left[\left(\frac{1}{O_2(0)} + \frac{u}{aK}\right)e^{at} - \frac{u}{aK}\right]^{-1} \leq O_2(t) \tag{2.9}$$

$$\leq \left[\left(\frac{1}{O_2(0)} - \frac{1}{K}\right)e^{-ut} + \frac{1}{K}\right]^{-1}. \tag{2.10}$$

Proof. From the non-negativity of the gas quantities

$$\frac{dO_2}{dt} \geq -\frac{uO_2^2}{K} - aO_2. \tag{2.11}$$

By the comparison argument in Lemma 1, we know that

$$O_2(t) \geq \left[\left(\frac{1}{O_2(0)} + \frac{u}{aK}\right)e^{at} - \frac{u}{aK}\right]^{-1}, \tag{2.12}$$

which is the solution of the initial value problem

$$\nu' = -\frac{u\nu^2}{K} - b\nu \quad \text{in} \quad (0,\infty), \quad \nu(0) = O_2(0). \tag{2.13}$$

On the other hand, for the upper bound of $O_2(t)$ we have

$$\frac{dO_2}{dt} \leq uO_2 - \frac{uO_2^2}{K}. \tag{2.14}$$

Once again from the comparison argument,

$$O_2(t) \leq \left[\left(\frac{1}{O_2(0)} - \frac{1}{K}\right)e^{-ut} + \frac{1}{K}\right]^{-1}, \tag{2.15}$$

which is the solution of the initial value problem

$$\nu' = u\nu - \frac{u\nu^2}{K} \quad \text{in} \quad (0,\infty), \quad \nu(0) = O_2(0). \tag{2.16}$$

□

From the results of Theorem 2.4.2, we can then determine the ultimate bounds for the amount of oxygen in the trachea, $O_2(t)$, namely

$$0 \leq \lim_{t\to\infty} \inf(O_2(t)) \leq \lim_{t\to\infty} \sup(O_2(t)) \leq K. \tag{2.17}$$

Next we look at ultimate bounds for both CO_2 and H_2O. Let $N_j(t)$ denote the total oxygen volume/density where O_2 is allowed to occupy two regions. These regions are the trachea(tracheoles) and the tissues. These two regions are coupled by the diffusion of the respiratory gases.

Theorem 2.4.3. *When $N_j(0) \leq K$ $(j = 1, 2)$, the gas volumes CO_2 and H_2O satisfy:*

$$(CO_2(0) + H_2O(0))\, e^{-\mu t} \leq CO_2(t) + H_2O(t) \tag{2.18}$$

$$\leq (CO_2(0) + H_2O(0))\, e^{\left(\frac{aK}{a+K} - \mu\right) t}. \tag{2.19}$$

Proof. Define $P = CO_2 + H_2O$, then

$$\frac{dP}{dt} = \frac{aO_2CO_2}{a + O_2} - \mu CO_2 + \frac{aCO_2H_2O}{a + CO_2} - \mu H_2O \geq -\mu P. \tag{2.20}$$

where $\mu = s \times d_{max_{CO_2}}$. By the comparison argument in Lemma 1, we have

$$CO_2(t) + H_2O(t) = P(t) \geq (CO_2(0) + H_2O(0))\, e^{-\mu t}. \tag{2.21}$$

When $N_j(0) \leq K$ then $N_j(t) \leq K$ for all t. It can also be seen from the model that

$$\frac{dP}{dt} = \frac{aO_2CO_2}{a + O_2} - \mu CO_2 + \frac{aCO_2H_2O}{a + CO_2} - \mu H_2O \tag{2.22}$$

$$\leq aK \left[\frac{CO_2}{a + K} + \frac{H_2O}{a + K}\right] - \mu(CO_2 + H_2O) = \frac{aKP}{a + K} - \mu P \tag{2.23}$$

$$\leq \left(\frac{aK}{a + K} - \mu\right) P. \tag{2.24}$$

Again by the comparison argument

$$CO_2(t) + H_2O(t) = P(t) \tag{2.25}$$

$$\leq P(0) e^{\left(\frac{aK}{a+K} - \mu\right) t} \tag{2.26}$$

$$= (CO_2(0) + H_2O(0))\, e^{\left(\frac{aK}{a+K} - \mu\right) t}. \tag{2.27}$$

□

The following corollary gives a condition for the external elimination of carbon dioxide and water loss. This will be used later for the stability of a semi-trivial equilibrium solution.

Corollary 1. If $aK/(a+K) < \mu$ and $N_j(0) \leq K$ $(j = 1, 2)$, then

$$\lim_{t\to\infty}(CO_2(t) + H_2O(t)) = 0. \tag{2.28}$$

This result shows that persistence or elimination of the dependent gases is directly affected by the carrying capacity and initial volume of the trachea, as well as other physiological parameters such as the ingress rate, respiration rate, and saturation value of the functional response. Note that for Theorem 2.4.3 and Corollary 1, if one considers oxygen only occupying the trachea, then $N_j(t)$ is just $O_2(t)$.

2.5 Equilibrium solutions and stability

Our model system has five equilibrium solutions which are summarized in Table 2.1.

Equilibrium	O_2	CO_2	H_2O
E_1	N_1	$(N_d + N_1W_1)/N_f$	0
E_2	N_1	$(N_d + N_1W_1)/N_f$	$(N_e + N_1W_2)/N_g$
E_3	N_2	$(N_d + N_2W_1)/N_f$	0
E_4	N_2	$(N_d + N_2W_1)/N_f$	$(N_e + N_2W_2)/N_g$
E_5	K	0	0

TABLE 2.1: Five equilibrium solutions to our system.

The entries in Table 2.1 are defined as follows. For simplicity, we define $p = d_{maxCO_2}$ and $q = \delta_{CO_2}$.

$$N_1 = \frac{(N - K\sqrt{N_a}N_b)}{2N_c} \tag{2.29}$$

$$N_2 = \frac{(N + K\sqrt{N_a}N_b)}{2N_c} \tag{2.30}$$

$$\begin{aligned} N = &-a^2cgKqu + a^2g^2Kpqu + a^2(-g)Kq^2u + abcgKqu^2 \\ &- abg^2Kpqu^2 - 2abgKpqu + abgKq^2u^2 + 2acgKpu \\ &- 2acKqu - Ku(ac)^2 - ag^2Kp^2u + 2agKpqu - aKq^2u \\ &+ 2b^2gKpqu^2 - bcKpu + bgKp^2u - 2bgKpqu^2 \\ &- bKpqu + cKpu - gKp^2u + Kpqu \end{aligned} \tag{2.31}$$

$$N_a = c^2 - 2cgp + 2cq + g^2p^2 + 2gpq + q^2 \tag{2.32}$$

$$N_b = u\left(a^2gq - abgqu + ac - agp + aq + bp - p\right) \tag{2.33}$$

$$\begin{aligned} N_c = &-a^2g^2q^2u^2 + abcgqu^2 - abg^2pqu^2 + abgq^2u^2 \\ &- acgqu^2 + ag^2pqu^2 - agq^2u^2 + b^2gpqu^2 \\ &- 2bgpqu^2 + gpqu^2 \end{aligned} \tag{2.34}$$

$$\begin{aligned} N_d = &a^3(-g)Kq + 2a^2bgKqu - a^2cK + a^2gKp - a^2Kq \\ &- ab^2gKqu^2 + abcKu - abgKpu + abKqu + aKp \end{aligned} \tag{2.35}$$

$$\begin{aligned} N_e = &a^3(-e)gKq + 2a^2begKqu - a^2bfgqhu + a^2bgqshu \\ &- a^2ceK + a^2egKp - a^2eKq - ab^2egKqu^2 + ab^2fgqhu^2 \\ &- ab^2gqshu^2 + abceKu - abcfhu + abcshu - abegKpu \\ &+ abeKqu + abfgphu - abfqhu - abgpshu + abqshu \\ &+ aeKp - b^2fphu + b^2pshu + bfphu - bpshu \end{aligned} \tag{2.36}$$

$$N_f = a^2bgqu - ab^2gqu^2 + abcu - abgpu + abqu + b^2pu - bpu \tag{2.37}$$

$$\begin{aligned} N_g = &a^2bfgqu - a^2bgqsu - ab^2fgqu^2 + ab^2gqsu^2 \\ &+ abcfu - abcsu - abfgpu + abfqu + abgpsu - abqsu \\ &+ b^2fpu - b^2psu - bfpu + bpsu \end{aligned} \tag{2.38}$$

Finally,

$$\begin{aligned} W_1 = &a^2(-b)gqu - a^2gpqu + ab^2gqu^2 - acu \\ &+ agpu - aqu - bpu + pu \end{aligned} \tag{2.39}$$

$$\begin{aligned} W_2 = &a^2(-b)egqu - a^2egqu + ab^2egqu^2 + aceu \\ &+ aegpu - aequ - bepu + epu \end{aligned} \tag{2.40}$$

In Table 2.2, we summarize the conditions for a non-negative equilibrium solution.

Equilibrium	condition
E_1 & E_2	1. $N > K\sqrt{N_a}N_b$ & $N_c > 0$
	2. $N_d > -N_1W_1$ & $N_f > 0$
	3. $N_e > -N_1W_2$ & $N_g > 0$
E_3 & E_4	1. $N > -K\sqrt{N_a}N_b$ & $N_c > 0$
	2. $N_d > -N_2W_1$ & $N_f > 0$
	3. $N_e > -N_2W_2$ & $N_g > 0$
E_5	1. $K > 0$

TABLE 2.2: Conditions for a non-negative equilibrium.

We discuss the stability of the equilibrium solutions E_1-E_5. Through the method of linearization, it is known that an equilibrium solution is asymptotically stable if all the eigenvalues of the Jacobian matrix have negative real parts. For ease of computation, define $x = O_2$, $y = CO_2$ and $z = H_2O$ in this section only. The Jacobian matrix of our system is;

$$J = \begin{pmatrix} \eta_1 & \eta_2 & \eta_3 \\ \varphi_1 & \varphi_2 & \varphi_3 \\ \xi_1 & \xi_2 & \xi_3 \end{pmatrix}$$

where,

$$\eta_1 = -\frac{ay}{by+x} + \frac{axy}{(by+x)^2} - \frac{ux}{K} + u\left(1 - \frac{x+y}{K}\right) \tag{2.41}$$

$$\eta_2 = -\frac{ux}{K} - \frac{ax}{by+x} + \frac{abxy}{(by+x)^2} \tag{2.42}$$

$$\eta_3 = 0 \tag{2.43}$$

$$\varphi_1 = \frac{acy}{x(ag+1)+by} - \frac{acxy(ag+1)}{(x(ag+1)+by)^2} + \frac{aqy}{by+x} - \frac{aqxy}{(by+x)^2} \tag{2.44}$$

$$\varphi_2 = \frac{acx}{x(ag+1)+by} - \frac{abcxy}{(x(ag+1)+by)^2} + \frac{aqx}{by+x} - \frac{abqxy}{(by+x)^2} - p \tag{2.45}$$

$$\varphi_3 = 0 \tag{2.46}$$

$$\xi_1 = 0 \tag{2.47}$$

$$\xi_2 = -\frac{ez}{h+z} \tag{2.48}$$

$$\xi_3 = -\frac{ey}{h+z} + \frac{eyz}{(h+z)^2} + (f-s). \tag{2.49}$$

The stability analysis here is carried out on the water vapor differential equation parameters; f, s, e and h. This is motivated by the fact that insect survival solely depends on its ability to minimize water loss to resist dessication. Hence, the model system stability depends heavily on these parameters.

Theorem 2.5.1. *The equilibrium solution E_5 is unstable.*

Proof. By substituting the equilibrium E_5 into the Jacobian matrix, J, the associated eigenvalue problem is

$$\det|J - \lambda I| = 0. \tag{2.50}$$

This is equivalent to

$$(-a - \lambda)(f - \lambda - s)\left(\frac{ac}{ag+1} + aq - \lambda - p\right) = 0. \tag{2.51}$$

Since $f > s$, at least one eigenvalue is positive. As long as the insect is alive, the insect water ingress rate should be greater than the cuticular water loss. This indicates that E_5 is unstable.

E_5 is asymptotically stable when $f < s$ and $\frac{ac}{ag+1} + aq$. For $O_2(0) \leq K$, corollary 1 indicates that

$$\lim_{t\to\infty}(CO_2(t) + H_2O(t)) = 0. \tag{2.52}$$

Note that $O_2(t)$ converges $(t \to \infty)$ to K which is the global attracting equilibrium in the logistic equation

$$\frac{dO_2}{dt} = uO_2\left(1 - \frac{O_2}{K}\right). \tag{2.53}$$

□

The next theorems state new results concerning the stability of equilibrium solutions $E_1 - E_4$. Due to the complexity of the eigenvalue problems associated with these equilibrium solutions, we only obtained conditions of instability.

Theorem 2.5.2. *Assume $K > N > 0$, where N is as defined earlier. The equilibrium solutions E_1 and E_3 are unstable if*

$$\frac{f - s}{e} > \frac{N_d + N_jW_1}{hN_f} \tag{2.54}$$

where $j = 1, 2$ and $h > 0$.

Proof. By substituting E_1 into the Jacobian matrix, J, and then simplifying the resulting eigenvalue problem, one of the eigenvalues is given by

$$\lambda = f - s - e\frac{N_d + N_1W_1}{hN_f}. \tag{2.55}$$

Now, $\lambda > 0$ implies

$$f - s - e\frac{N_d + N_1W_1}{hN_f} > 0. \tag{2.56}$$

Hence

$$\frac{f-s}{e} > \frac{N_d + N_1W_1}{hN_f}. \tag{2.57}$$

□

Substituting E_3 into J follows the same analysis.

Theorem 2.5.3. *Assume $K > 0$ and $e > 0$, the equilibrium solutions E_2 and E_4 are unstable if either of these conditions hold:*

$$(i). \quad N_e + N_1W_1 > N_g(h + GG_j). \tag{2.58}$$

$$(ii). \quad \frac{N_d + N_jW_1}{N_f(h + GG_j)}\left[\frac{N_e + N_jW_2}{N_g(h + GG_j)} - 1\right] > \frac{s-f}{e} \tag{2.59}$$

where $GG_j = \dfrac{N_e + N_jW_2}{N_g}$, $j = 1, 2$ and $h > 0$.

Proof. By substituting E_2 into the Jacobian matrix, J, the third eigenvalue is given by

$$\begin{aligned}\lambda = &\frac{e(N_1W_1 + N_d)(N_1W_2 + N_e)}{N_fN_g\left(\dfrac{N_1W_2 + N_e}{N_g} + h\right)^2} \\ &- \frac{e(N_1W_1 + N_d)}{N_f\left(\dfrac{N_1W_2 + N_e}{N_g} + h\right)} + f - s.\end{aligned} \tag{2.60}$$

Now, $\lambda > 0$ implies

$$f - s + e\frac{N_1W_1 + N_d}{N_f(h + GG_1)}\left[\frac{N_e + N_1W_2}{N_g(h + GG_1)} - 1\right] > 0. \tag{2.61}$$

where $GG_1 = \dfrac{N_e + N_1W_2}{N_g}$.

The above inequality gives rise to two cases of instability. The first case (i) which is independent of e occurs when $N_e + N_1W_2 > N_g(h + GG_1)$. In this case, the inequality 2.61 will hold.

The second case (ii) occurs when $N_g(h+GG_1) > N_e+N_1W_2$. The inequality (2.61) holds when

$$\frac{N_1W_1 + N_d}{N_f(h + GG_1)}\left[\frac{N_e + N_1W_2}{N_g(h + GG_1)} - 1\right] > \frac{s-f}{e}. \tag{2.62}$$

□

By substituting E_4 into the Jacobian matrix and then simplifying the resulting matrix as above, similar results are found for the stability.

2.6 Numerical simulation

Numerical simulations for the dynamics and pattern of the gas volumes are discussed here. The dynamics of the model system change as we vary the parameter values. This behaviour may eventually settle on a steady-state or may exhibit some unstable behaviour. In each of the figures, the biological parameters K, f, s, e and h are chosen according to the conditions of stability or instability of the equilibrium given in the theorems in sections 2.4 and 2.5. A stable steady-state in the plots of the dynamic system suggests that the system trajectories tend to an equilibrium state as $t \to \infty$. That is, the system is characterized by a fixed loop or an inward spiral. Instability is characterized by unstable behaviour, where the trajectories drift in an unbounded fashion and the system never forms an orbit around that point [43]. The initial gas volumes were taken from the sample data received earlier: $O_2(0) = 0.25$ ml, $CO_2(0) = 0.75$ ml and $H_2O(0) = 1.75$ ml.

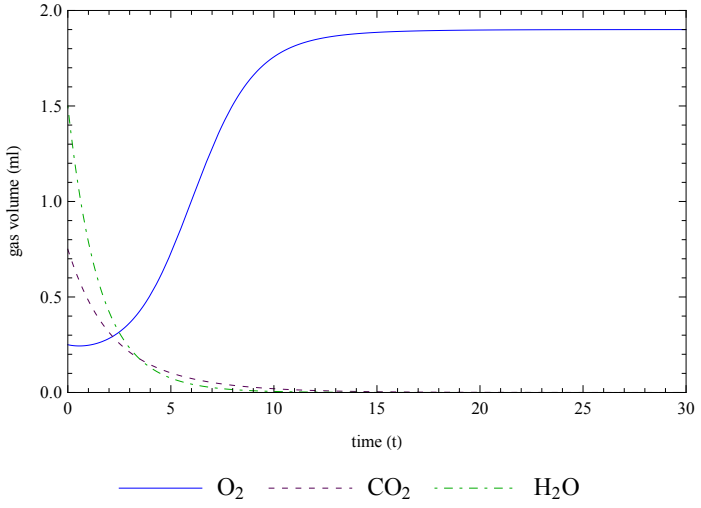

FIGURE 2.2: This figure shows the stability of equilibrium E_5 when $f < s$, which is given in Theorem 2.5.1. We choose $f = 0.5$ and $s = 1$. As can be seen from the graph, the oxygen volume goes to equilibrium $K = 1.9$ and the carbon dioxide and water-vapor go to equilibrium 0.

Figures 2.2, 2.3 and 2.4 show the time series diagrams of the system of differential equations for different values of the system parameters. The simulations were carried out to determine the ranges in the parameter spaces which support the dynamic behaviour of this system. These ranges were then compared with the actual parameter values from the data received. For the model to be applicable, the ranges of the parameter values must be biologically feasible and

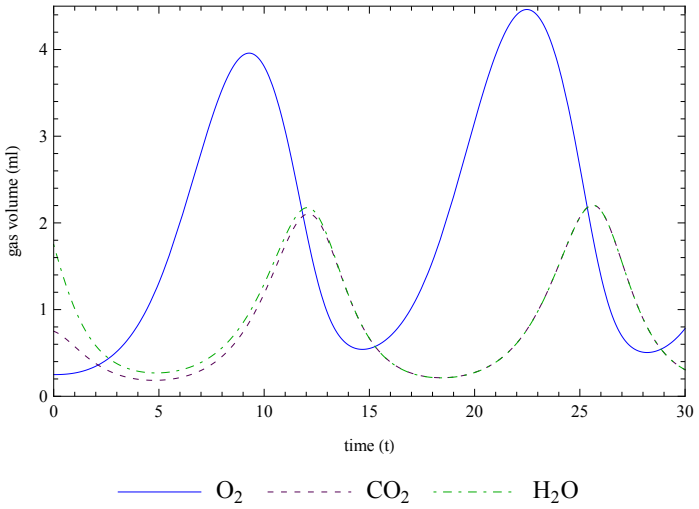

FIGURE 2.3: This figure illustrates the case when equilibria E_1 and E_3 are both unstable. The condition for instability is $(f - s)/e > (N_d + N_j W_1)/hN_f$. For this case we choose $K = 5$, $u = 0.7$, $f = 0.5$, $s = 0.03974$, $e = 0.8$ and $h = 2.7$.

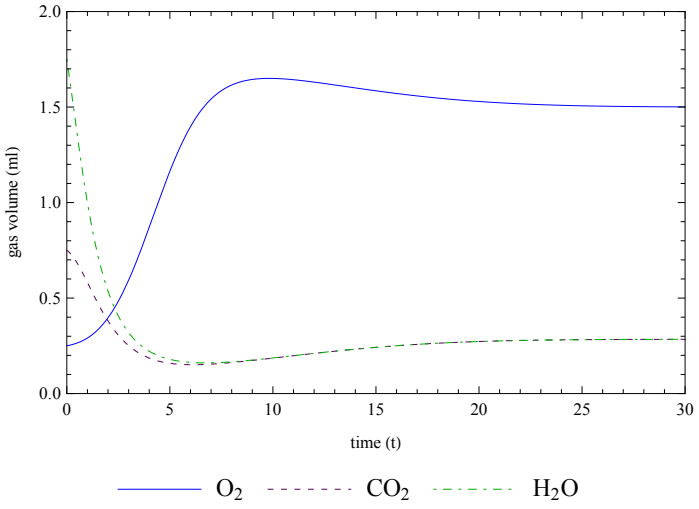

FIGURE 2.4: This figure shows the stability of both E_2 and E_4. We choose the parameters $a = 0.6$, $K = 1.9$, $u = 1$, $f = 0.5$, $s = 1$, $e = 0.5$ and $h = 1$.

must contain or enclose the parameter values from the actual data. The system stability was studied by varying one of the critical parameter values while fixing the others.

Figure 2.2 shows the stability of E_5 when $f < s$, characterized by a quick convergence of CO_2 and H_2O towards their equilibrium values. However, this condition is not feasible biologically while the insect is alive. The model stability is achieved when the water ingress rate into the trachea is less than the water loss due to the cyclic openings. This would mean that the insect is losing water and thus the insect eventually dies from dessication. The time series shows that O_2 goes to equilibrium $K = 1.9$, the tracheal carrying capacity. CO_2 and H_2O go to equilibrium zero. In figures 2.2 and 2.4, for prolonged spiracle opening, the CO_2 and H_2O graphs decay to the long-term steady-state values as outlined in table 2.1. Values of CO_2 and H_2O below

zero would mean that the insect is not breathing or may be dead from dessication, hence the condition $f > s$ is of interest to biologists.

Cuticular water-loss plays a major role in determining the stability of both E_1 and E_3. Figure 2.3 illustrates the case when equilibria of E_1 and E_3 are both unstable. The time series is characterized by an outward spiral. For instance, the O_2 volume at the first peak when $t = 9.3$ is approximately 3.96 ml. At the second peak at $t = 22.5$, O_2 volume is approximately 4.46 ml. For even larger values of t, the O_2 values reach even higher volumes, while both CO_2 and H_2O oscillate in a stable manner with no convergence. Figure 2.4 shows the stability of both E_2 and E_4 for specific parameter values K, u, f, s, e and h. O_2 converges to the equilibrium N_1 which is slightly below the tracheal carrying capacity, K. The CO_2 and H_2O graphs oscillate in a stable manner initially and finally converge to $(N_d + N_1W_1)/N_f$ and $(N_e + N_1W_2)/N_g$ respectively.

2.7 Discussion

Our main objective was to obtain a mathematical model that depicts how the respiratory gases manage to move in opposite directions simultaneously. We developed the model described by equations in section 2.3 and studied its existence for different ranges of system parameters. Additionally in section 2.6 we investigated the variable parameter ranges to control unstable dynamics, if any. The simulation results suggest that the model system may show different interesting dynamical behaviour starting from stable limit cycle to unstable cycles.

In section 2.4, we found that the O_2 and CO_2 gases in the trachea were bounded below by zero and above by twice the tracheal carrying capacity. Hence, as long as the insect is alive, tracheal O_2 volume should be positive. Likewise, prolonged O_2 uptake means respiration is prolonged and thus there is a positive CO_2 volume in the trachea. The combined tracheal volume of O_2 and CO_2 cannot exceed $2K$.

The stability analysis was undertaken on the water vapor differential equation parameters; f, s, e and h in section 2.6. From the simulation results, these parameters are responsible for determining the stability of our system and thus the insect survival. We found that f, s and h were bounded over a large parameter regime compared to the other system parameters such as a and e. Our system supports stable limit cycles in a reasonably fair parameter range for f, s and h. Unpredictable behaviour was observed outside these studied parameter values in narrow ranges. For instance, the cumulative effect of increased e results in an inward shift in the H_2O graph as shown in figure 2.5. With increased cuticular water loss rate, the dynamics of H_2O quickly converges to zero, beyond which we would expect dessication.

When the oxygen ingress rate in the trachea is high, the volume of oxygen in the insect respiratory system rises and so does the elimination of carbon dioxide. An increase in the elimination

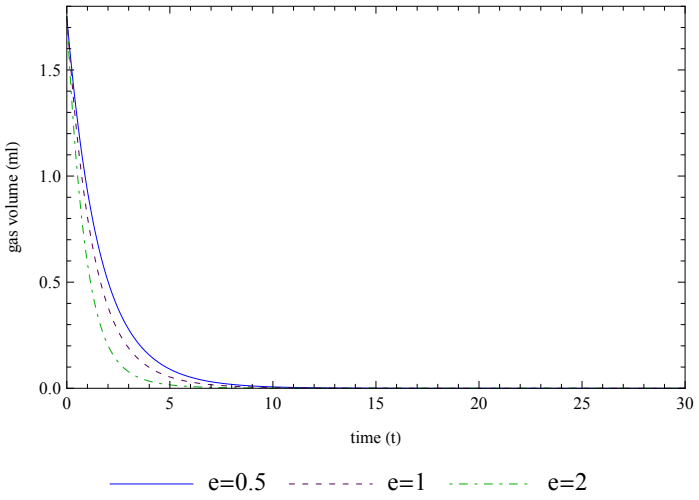

FIGURE 2.5: H_2O profile in the beetle for varying values of e. Here, all other parameter values are fixed.

of carbon dioxide results in large volumes of water loss into the atmosphere. A further increase in this oxygen ingress results in further elimination of CO_2 and thus unpredictable dynamics will be observed. Figure 2.6 depicts this observation. For instance, the O_2 and H_2O graphs oscillate in an unstable manner. As K increases, the spiracle remains open for a longer time to increase O_2 uptake. The longer the spiracular opening the more H_2O is lost to the atmosphere. Prolonged H_2O loss results in unpredictable dynamics.

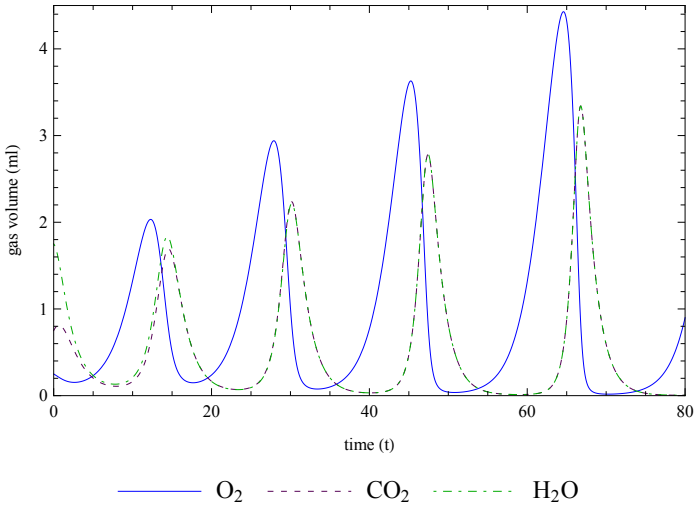

FIGURE 2.6: Phase diagram with unstable trajectories. Here $K = 9$ and $u = 0.7$.

The dung beetle receives oxygen from the atmosphere when it opens its spiracles. These high oxygen volumes increase the values of K and u. The carrying capacity (the insect tracheal system maximum load) limits the amount of oxygen that the insect can take in at any given time. Thus when the values of u and K are high, and keeping other parameters constant, the model system is expected to exhibit some unstable dynamics. Since water is lost as a consequence during the

elimination of CO_2, we expect that an increase in a results in large quantities of water loss. Dessication results due to large quantities of water being lost; hence the cumulative effect of increased a is to force the dynamics of the system to settle on an unstable state.

Insects adapt to control for this unstable behaviour by performing DGC. During DGC, O_2 uptake and CO_2 release follow a cyclical pattern defined by periods of little to no release of CO_2. Thus they have a way of keeping K, u and a low most of the time. The value of a (respiration rate) is bounded on a narrow range where the system exhibits stable behaviour. Search for food and flight from danger demand an increase in the value for a.

The competing species model is a useful starting point to illustrate that the respiratory gases compete for space in both the spiracle opening and the tracheal system. The model developed here reveals that the change in CO_2 elimination is directly related to the level of oxygen uptake into the trachea, while the change in water levels in the trachea is directly proportional to CO_2 emission. The equilibria are stable over fairly large parameter regimes and exhibit cycles in which prolonged O_2 uptake perpetually rises and falls in a systemic manner.

Chapter 3

Gas exchange models for a flexible insect tracheal system

The work in this chapter has been submitted to *Acta Biotheoretica.*

In this chapter two models for movement of respiratory gases in the insect trachea are presented. One model considers the tracheal system as a single flexible compartment while the other model considers the trachea as a single flexible compartment with gas exchange. The purpose of the work is to study nonlinear phenomena seen in the insect respiratory system. It is assumed that the flow inside the trachea is laminar, and that the air inside the chamber behaves as an ideal gas. Further, with the isothermal assumption, the expressions for the tracheal partial pressures of oxygen and carbon dioxide, rate of volume change, and the rates of change of oxygen concentration and carbon dioxide concentration are derived. The effects of some flow parameters such as diffusion capacities, reaction rates and air concentrations on net flow are studied. Numerical simulations of the tracheal flow are performed. The model developed can be regarded as the controlled system and provide a mathematical framework to further investigate gas exchange in insects.

3.1 Introduction

Insects are the most abundant and successful terrestrial arthropods. Many physiological structures and processes are only uniquely found in insects. One unique feature is the air-filled respiratory system, the tracheal system, which uses both diffusion and convection for efficient distribution of respiratory gases [44–46]. The trachea generally consists of gas filled tubes that bifurcate into all parts of the body delivering oxygen (O_2) and removing carbon dioxide (CO_2) [59, 60]. The distal ends of the tubes concentrate at lateral pores called the spiracles in the

external cuticle and connect the tracheal system to the outside [61]. The spiracles have constricting muscles or valve-like structures which open and close to regulate gas exchange. The action of these valves ultimately affects the changes in diffusive and conductive conductance. During rest, many insects close their spiracles and only exchange oxygen and carbon dioxide during brief periods of time [63]. In extreme cases, the spiracles remain open for longer periods if oxygen demand is elevated by high temperature, activity, and during reproduction.

After passing through a spiracle, air enters a longitudinal tracheal trunk eventually diffusing throughout a complex, branching network of tracheal tubes that subdivide into smaller and smaller diameters and reach every part of the body. The large trachea (which can be up to 0.2 mm) is supported by annular or spiral thickening of the cuticle [59]. At the end of the smallest tracheal branch, about 2 to 5 μm in diameter, the tracheoles, each less than 1 μm in diameter [59, 60], provide a thin, moist interface for the exchange of gases between atmospheric air and a living cell. The terminal ends of the tracheoles are often filled with interstitial fluid [13, 50]. Evidence suggest that there is no difference in the permeability of larger trachea or tracheoles to oxygen, but only tracheoles are close enough to mitochondria for O_2 to diffuse to the mitochondria in quantities needed [59]. Snelling *et al.* [92] showed that while the tracheoles only comprise 13% of the intratracheal volume, their high surface area-to-volume ratio allows them to provide more than 90% of the tracheal system lateral diffusion capacity. Oxygen first dissolves in the liquid of the tracheole and must then move across the tracheal walls, across the plasma membranes of the adjacent cells, the cytoplasm and finally through mitochondrial membranes [59]. The tracheoles are the main site of gas exchange with tissues; they closely surround and might even penetrate the tissues to become intimately associated with individual cells and to lie close to mitochondria [46, 59, 64] where cell respiration and energy metabolism occur. Carbon dioxide moves in the opposite direction. Increased ionic strength or acidification of the interstitial fluid withdraws fluid from the tracheoles, facilitating gas exchange during activity or varying oxygen partial pressures.

Insect respiration is significantly different from mammalian respiratory system in which there are lungs and a circulatory system with an oxygen carrier [88]. The mammalian circulatory system deliver oxygen to tissues where respiration takes place. Likewise, cellular respiration and energy metabolism occur in the mitochondria. The insect respiratory and circulatory systems have been totally disengaged, relegating the circulatory system from a meaningful role in gas exchange [60]. Insects have an open circulatory system in that they do not have arteries or veins and instead blood (hemolymph) flows openly throughout their bodies. The hemolymph squeezes around in an open space called the hemocoel ("blood space"). The hemolymph differs from vertebrate blood in that it does not have red blood cells which in vertebrates contain a special protein, the hemoglobin, that binds oxygen. Although the hemolymph does not have red blood cells, O_2-binding pigments known as hemocyanins have been found in the hemolymph of a variety of primitive insects phyla such as the mollusca and athropods [55, 65]. Hemocyanins are

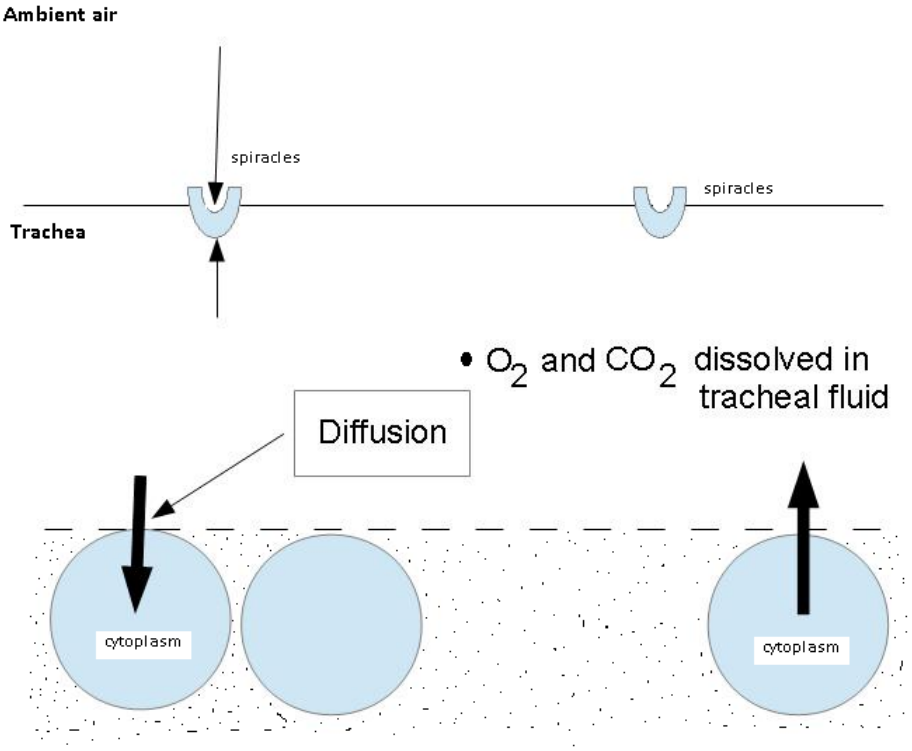

FIGURE 3.1: Schematic view of the tracheal system and circulation with gas exchange.

metalloproteins that contain two copper atoms that reversibly bind a single O_2 molecule, and are not bound to cells but are suspended directly in the hemolymph [55, 65]. Recently, hemoglobin has been identified in *Drosphila, Anopheles, Apis* and many other insects [66]. Whether the hemolymph hemocyanins or hemoglobin play a significant role in oxygen delivery is still a subject of much debate. The structure and layout of the cells suspended in the hemolymph (insect blood) is shown in figure 3.1.

Key functional differences arise due to this structural diversity of the insect respiratory system, most notable the external gas exchange patterns. Some insect groups (beetles, ants, butterfly pupae, grasshoppers and cockroaches) use the novel form of respiration (in an evolutionary sense) known as discontinuous gas-exchange cycle (DGC), and all insects have an open circulatory system. In the case of discontinuous gas exchange, O_2 consumption and CO_2 production are continuous but the external elimination of gases is discontinuous [9, 24], hence the reference to discontinuous gas exchange. DGC consists of three phases [25, 27, 54]; (1) a closed spiracle phase where the insect is hermetically sealed [54, 56], (2) a flutter phase where the spiracles flutter allowing small quantities of air down the pressure gradient, and (3) an open spiracle phase where the spiracles remain fully open and the gases are exchanged with the atmosphere. O_2 gain and CO_2 loss occur mainly during the open spiracle phase. Under different ambient conditions and metabolic demands, the same insects have been observed switching to continuous and cyclic ventilation. Hypercanic and hypoxic environments induce the abandonment of DGC

in favor of continuous respiration [90, 91]. Extreme ambient conditions increases the cycle frequency and may result in an open spiracle state [89]. Several adaptive and non-adaptive explanations for the occurrence of the *DGC* pattern in terms of its mechanisms and its role in the physiological functioning of the insect have also been proposed. Adaptive hypotheses look into the effects and benefits of *DGC*. These include the chthonic, oxidative damage, and metabolic rates hypothesis, focusing on issues of the elimination of carbon dioxide and delivery of oxygen [24, 88, 89]. Closure of the spiracles is proposed to be an important water conservation mechanism by the hygric hypothesis [8, 21, 52, 54]. Non-adaptive hypotheses address causes of and mechanisms of *DGC* [88]. These include the neural hypothesis which proposes that *DGC* occurs as a passive pattern under low brain activity [89], and the emergent hypothesis which poses *DGC* as a pattern that emerges under certain conditions and is a result of two interacting feedback loops regulating internal partial pressures of oxygen and carbon dioxide [89, 91].

The primary goals of the insect respiratory system are to deliver oxygen from the air to the tissues and to transport carbon dioxide from the tissues to air. Most of the oxygen and carbon dioxide transport occurs in the gas phase, with the gases transported through the tracheal system by both diffusion and convection. The airflow inside the tracheal network might be tidal or directed, depending on the insect class and its physiological systems. Most insects use their body movements and multiple wall contractions along the tracheal network to enhance the convected airflow and to produce tidal or directed airflow. Rhythmic contractions observed at multiple locations are believed to be the main driving force that efficiently delivers and transports fresh air to every cell. Contractions exist in sequences and are naturally set to move in the tube lateral direction. The motion of the contractions is induced as a result of internal pressure variations as alternations that might be produced by the entire body movements action or by the hemolymph circulation. The rapid cycles of compression and expansion are analogous to inflation and deflation of the human lung system.

Numerous studies have investigated the function of the trachea in gas exchange, revealing complex interactions between the insect tracheal system and gas transport. Examples of such interactions include rhythmic contractions and redistribution of air [47–49], innervation of the spiracle muscles and spiracle control [50, 51], and spiracle control for discontinuous gas exchange [8–10, 52–54]. Models of gas exchange across the spiracles has also been presented and studied in different levels of detail [7, 12–14, 52, 54, 57]. These models, however, ignore complications known to insect physiologists such as end diffusion, the role of the hemolymph in respiration, and interaction of vapor leaving and gas entering the tubes. Recently, Grieshaber and Terblanche [88] presented a two sensor *DGC* model (pH/carbon dioxide and oxygen setpoints) for an Orthopteran gas exchange system and they showed computationally that a control system of two interacting feedback loops is capable of generating a full *DGC* pattern. Their study considers not only gas exchange at the spiracles, but sources and sinks for both O_2 and CO_2 systems in

isolation and interaction between these systems. They went on to show that their results support the emergent property hypothesis for the existence of DGC. However, we should highlight that our study focused only on the mechanistic aspects of DGC and not on the revolutionary aspects just like Grieshaber and Terblanche [88] work. We were looking at the how and not the why.

The work presented in this manuscript is based on Ben-Tal's [67] previous work on models for gas exchange in the human lung which is extended here to tracheal flow, with proper determination of the flow parameters. Although there are significant differences between gas exchange in human lungs and the insect respiratory system, we modify these models to uniquely explain the phenomena observed in insect physiology. We regard the gas exchange process as controlled in that the hemolymph pressure, cytoplasm volume and respiratory output are the controlled variables. The O_2 and CO_2 partial pressures are the measured variables and are viewed as disturbances to the control system. The disturbances are taken into account implicitly via tissue/cells partial pressures of O_2 and CO_2 at the tips of the tracheoles. The hemocoel pressure is the pressure in the cavity between the trachea and insect outer body line, and will also affect air flow. The insect body tissues are another compartment of gas exchange. Thus, gas exchange at tissue level (respiring cell level) is a critical part of the mathematical model developed.

As has been highlighted, one of the difficulties in developing mathematical models is to decide what structured features need to be incorporated in the model to capture certain phenomena. This is made even more difficult where processes that occur on different scales need to be considered simultaneously. Whether structure implies function or whether structure obscures function is an important question in science. In this paper, we present a model that addresses spiracle behaviour on flow of gases, including cellular respiration and tissue absorption, tracheal flow at microscale, and global gas movement within the insect. The simple and detailed models provide more quantitative information and insight into the insect system and the process of DGC. It is assumed that the flow is laminar and that the air inside the trachea behaves as an ideal gas. We also assume that during the open spiracle phase the airflow through the spiracle is equal to the rate of change in the trachea, and that the process of oxygen uptake by the mitochondria is near equilibrium. Further, with the isothermal assumption, the expressions for tracheal partial pressures of oxygen and carbon dioxide, rate of change of the gas concentrations, and rate of tracheal volume change are presented. Finally, numerical simulations of gas flow inside the trachea are performed, with parameters obtained from the literature and with proper initial and boundary conditions. We hope this is a first step in constructing a truly microscale representation of gas exchange across the insect tracheal system. The symbols used in the mathematical model are not the standard symbols used in respiratory physiology but are chosen to make the mathematical equations easier to read.

3.2 Mathematical models for the tracheal system

In this section we present two models for the insect tracheal system. The designed models are based on the work of Ben-Tal [67] on compartmental gas exchange (see also [68, 69]). In all the models, we present the trachea as a single container of air. The mathematical derivations of the model are described. Unless stated otherwise, the models presented are for the open spiracle phase. For all the models, it is assumed that body temperature depends on ambient temperature and does not change throughout the breathing process. Note that we use T for temperature, but also use the sub-index T to refer to the trachea. Sub-index T should not be confused with temperature.

3.2.1 Flexible trachea

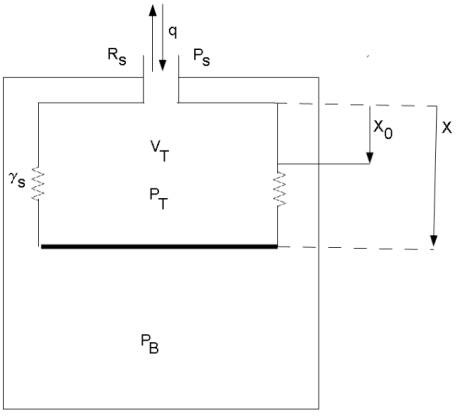

FIGURE 3.2: The trachea modeled as a flexible container. V_T-total tracheal volume, P_T-average tracheal pressure, P_s-spiracle pressure, P_B-body/hemocoel pressure, q-airflow, R_s-overall resistance of airways, X_0-unloaded spring position, X-loaded spring position, and γ_s-spring constant representing the trachea expansion.

Figure 3.2 illustrates a simple model that takes into account the flexibility of the trachea and in which the trachea can hold air. The trachea is modeled by a large, single and flexible container. The total volume of the container is given by V_T, and is constant with value V_0 in the case where no abdominal contractions are observed. P_s is the pressure inserted by the spiracle muscles plus that exerted by ambient air when the spiracles open (this pressure is assumed to be constant for a rigid container). P_T is the total pressure averaged over all the parts of the trachea (note that we state all the pressures in absolute value), P_B is the body/hemocoel pressure, R_s is the overall resistance to airflow in the conducting airways, γ_s is the spring constant representing the trachea expansion, and q is the net airflow during the open spiracle phase. Note that a symbol may refer to (physical, chemical) feature as well as the value related to it.

We intend to show that changes in the body/hemocoel pressure cause the tracheal pressure to change, resulting in airflow in and out of the trachea (the hypothesis is supported by findings

given in Pendar *et al.* [93] and Aboelkassem and Staples [122]). Hemocoel pressure changes due to movement of the body due to locomotion and flight. For this model to capture the possibility of the tracheal wall movements, we assume that the lower wall of the trachea (see figure 3.2) is a moving plate with mass m, friction μ and an area A. The plate is moved up or down by a spring Γ_s. The trachea elastance, E_T, is equivalent to γ_s/A^2, the trachea resistance, R_T, is equivalent to μ/A^2 and the inertance, I_T, is equivalent to m/A^2. In figure 3.2, the spring is unloaded at X_0. The spring contraction represents trachea contraction while spring extension represents expansion.

Assuming laminar flow, the following relationship holds;

$$qR_s = P_s - P_T. \tag{3.1}$$

If the air inside the container behaves as an ideal gas (this assumption holds if the gas is far from its condensation point), then

$$P_T V_T = nkT, \tag{3.2}$$

where n is the number of gas molecules, k is the Boltzman constant and T is the absolute temperature. Further, we assume a constant temperature with volume, pressure and number of particles changing with time. The outside air is treated as an infinite source with a constant pressure P_s and a rate of volume change that is equal to q. Thus, the relationship between the rate of change in the number of air molecules and the net flux q into the chamber is

$$P_s q = \frac{dn}{dt} kT. \tag{3.3}$$

If the number of molecules that leave the outside air is the same as those that enter the trachea, then

$$V_T \frac{dP_T}{dt} + P_T \frac{dV_T}{dt} = \frac{dn}{dt} kT = P_s q. \tag{3.4}$$

Rearranging equation 3.4, the rate of change of P_T is given by

$$\frac{dP_T}{dt} = \frac{1}{V_T} \left(P_s q - P_T \frac{dV_T}{dt} \right), \tag{3.5}$$

where (from equation 3.1)

$$q = \frac{P_s - P_T}{R_s}. \tag{3.6}$$

q can be written as $q = q_i - q_e$, with q_i denoting the air flow from an infinite source into the trachea, and q_e denoting the air flow out of the trachea into the infinite source. In case $q = q_i - q_e > 0$, there is a net flux into the trachea, and a negative value of q implies a net flux out of the trachea.

From the equation of motion of a mass on a spring (equation of the moving plate) in figure 3.2, we obtain the rate of change of V_T given by

$$I_T \frac{d^2V_T}{dt^2} + R_T \frac{dV_T}{dt} + E_T(V_T - V_0) = P_T - P_B. \tag{3.7}$$

3.2.2 Flexible trachea with gas exchange

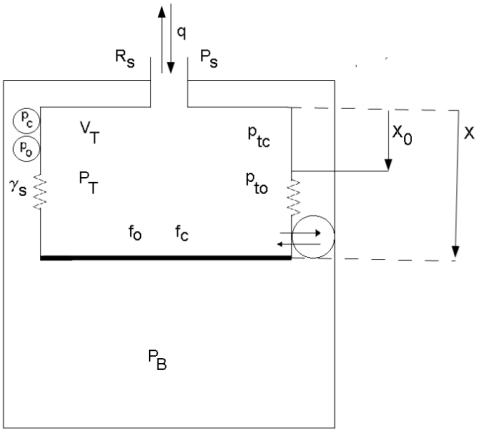

FIGURE 3.3: Model for a flexible container with gas exchange. p_o and p_c are the respiring cells partial pressures of O_2 and CO_2, respectively. p_{to} and p_{tc} are the tracheal partial pressures of O_2 and CO_2, respectively. f_o and f_c are the tracheal concentration of O_2 and CO_2 respectively. All other symbols are the same as those defined in figure 3.2.

Figure 3.3 shows a model of a flexible trachea with gas exchange. Insects rely on passive diffusion and physical activity for the movement of gases within the tracheal system. Recent studies [25, 44, 49] have revealed that insects use their abdominal muscles to alternately expand and contract body volume. These body movements act as a pumping mechanism to further enhance the transport of O_2 and CO_2. In the tracheole, O_2 dissolves in the liquid of the trachea and then diffuses into the cytoplasm of an adjacent cell (represented by the circles in figure 3.3). All the symbols in figure 3.3 are the same as those defined in figure 3.2 with the addition of the O_2 tracheal partial pressure, p_{to}, and CO_2 tracheal partial pressure, p_{tc}.

$$p_{to} = f_o(P_T - p_w), \tag{3.8}$$

$$p_{tc} = f_c(P_T - p_w), \tag{3.9}$$

where f_o and f_c are the O_2 and CO_2 concentrations, respectively. P_T as before is the total pressure in the tracheoles and p_w is the vapor pressure of water at 25^oC. p_o and p_c are the cytoplasm/respiring cell partial pressures of O_2 and CO_2, respectively. For this model, p_o and

p_c are parameters. The fluxes of oxygen (F_o) and carbon dioxide (F_c) are given by,

$$F_o = D_o(p_o - p_{to}), \tag{3.10}$$

$$F_c = D_c(p_c - p_{tc}), \tag{3.11}$$

where D_o and D_c are the diffusion capacities of O_2 and CO_2, respectively. The direction of the fluxes depends on the partial pressures in the cells and in the tracheoles. If $p_{to} > p_o$, then $F_o < 0$ meaning that oxygen diffuses from the tracheoles to the cells. During the open spiracle phase, the net flux of gas into the trachea is given by

$$Q_T = q + D_c(p_c - p_{tc}) + D_o(p_o - p_{to}). \tag{3.12}$$

For the closed spiracle phase $q = 0$.

Assuming an ideal gas and a constant T throughout the exchange process while V_T, P and n change, and taking the number of molecules that leave the outside air equal to those that enter the trachea, the rate of change of P_T is given by

$$\frac{dP_T}{dt} = \frac{1}{V_T}\left(P_s q + P_T(D_c(p_c - p_{tc}) + D_o(p_o - p_{to})) - P_T\frac{dV_T}{dt}\right). \tag{3.13}$$

The rate of tracheal volume change is given by equation 3.7.

If we define the diffusion capacities units as $mols^{-1}mmHg^{-1}$, then $D_c(p_c - p_{tc}) + D_o(p_o - p_{to})$ gives a direct measurement of dn/dt [1]. The O_2 concentration, f_o, is the ratio between the number of oxygen molecules n_o and the total number of gas molecules n in the trachea. Thus, the rate of change of f_o with respect to time can be expressed as

$$\frac{df_o}{dt} = \frac{d}{dt}\left(\frac{n_o}{n}\right) = \frac{d}{dt}\left(\frac{V_{to}}{V_T}\right) \tag{3.14}$$

$$= \frac{1}{V_T}\left(\frac{dV_{to}}{dt} - f_o\frac{dV_T}{dt}\right), \tag{3.15}$$

where V_{to} is the volume of oxygen in the trachea. For the open spiracle phase we have the rate of change of oxygen volume in the trachea as

$$\frac{dV_{to}}{dt} = D_o(p_o - p_{to}) + f_{oi}q_i - f_o q_e, \tag{3.16}$$

where q_i is inward airflow during the open spiracle phase, q_e is the outward airflow during the open spiracle phase and f_{oi} is the concentration of O_2 in the bulk inward air through the spiracles (ambient air concentration of O_2) (D_o , f_{oi}, q_i & $q_e \geq 0$). For the closed spiracle phase, we have

[1] In literature, the values of D_o and D_c are given as $ls^{-1}mmHg^{-1}$ while some authors give them as $mols^{-1}mmHg^{-1}$. The conversion between these values is usually done by assuming a constant pressure.

$$\frac{dV_{to}}{dt} = D_o(p_o - p_{to}). \tag{3.17}$$

During the closed spiracle phase, there is no outward ventilation and so $q_i = q_e = 0$. Note that respiration within the insect is a continuous process and so the internal flux $D_o(p_o - p_{to})$ is never zero.

If we assume that $dV_T/dt = Q_T$ (this is true near equilibrium), then the rate of change of f_o and f_c for the open spiracle phase can be approximated as

$$\frac{df_o}{dt} = \frac{1}{V_T}\left(D_o(p_o - p_{to}) + (f_{oi} - f_o)q_i - f_o(D_o(p_o - p_{to}) + D_c(p_c - p_{tc}))\right), \tag{3.18}$$

$$\frac{df_c}{dt} = \frac{1}{V_T}\left(D_c(p_c - p_{tc}) + (f_{ci} - f_c)q_i - f_c(D_o(p_o - p_{to}) + D_c(p_c - p_{tc}))\right). \tag{3.19}$$

f_{oi} and f_{ci} are constant in this model. For the closed spiracle phase, the rate of change of f_o and f_c can be expressed as

$$\frac{df_o}{dt} = \frac{1}{V_T}\left(D_o(p_o - p_{to}) - f_o(D_o(p_o - p_{to}) + D_c(p_c - p_{tc}))\right), \tag{3.20}$$

$$\frac{df_c}{dt} = \frac{1}{V_T}\left(D_c(p_c - p_{tc}) - f_c(D_o(p_o - p_{to}) + D_c(p_c - p_{tc}))\right). \tag{3.21}$$

Equations 3.7, 3.13, 3.18 and 3.19 form a system of nonlinear ordinary differential equations for the open spiracle phase of a flexible trachea, while equations 3.7, 3.13, 3.20 and 3.21 form a system for the closed spiracle phase.

Under certain assumptions, the models described above can be reduced to simpler models. The models are simplified to understand the conditions under which certain assumptions are valid.

3.2.2.1 Simplified flexible model

If we assume that the velocity and acceleration terms in equation 3.7 are very small, then the volume of the trachea can be approximated as

$$V_T = \frac{P_T - P_B}{E_T} + V_0. \tag{3.22}$$

Substituting equation 3.22 and its derivative with respect to t into equation 3.4 yields,

$$\frac{dP_T}{dt}\left(\frac{P_T - P_B}{E_T} + V_0\right) + P_T\frac{1}{E_T}\left(\frac{dP_T}{dt} - \frac{dP_B}{dt}\right) = P_s q. \tag{3.23}$$

If V_0 is small and P_T and P_B are of the same order (which is the case near equilibrium, when the tracheal pressure P_T is similar to the cytoplasm pressure P_B), then the compressibility of

air $(P_T - P_B)/E_T + V_0$ is small compared to P_T/E_T. This implies that changes in tracheal pressure due to volume change are more dominant than changes in the pressure due to the compressibility of air. Ignoring the inertia and compressibility of air, and rearranging equation 3.23 with $q = (P_s - P_T)/R_s$ (equation 3.6) yields

$$\frac{dP_T}{dt} = \frac{E_T P_s}{P_T}\left(\frac{P_s - P_T}{R_s}\right) + \frac{dP_B}{dt}. \tag{3.24}$$

Now, linearizing near the equilibrium point (where $P_T = P_s$) gives

$$\frac{dP_T}{dt} = \frac{E_T}{R_s}(P_s - P_T) + \frac{dP_B}{dt}. \tag{3.25}$$

Equations 3.18, 3.19 and 3.25 are used in the numerical simulations shown for the flexible model with gas exchange.

3.2.2.2 A calculated averaged model from the flexible tracheal model with gas exchange

Under certain assumptions, the flexible tracheal model with gas exchange can be reduced to a calculated average model. $D_c \geq 0$, so we consider two cases: when $D_c = 0$ and when $D_c \neq 0$. If $D_c = 0$, then an average value of $p + to$ at steady state (designated as $\bar{p}_{to}$) can be calculated by solving the nonlinear ordinary differential equation 3.26 (see also equation 3.18):

$$0 = D_o(p_o - \bar{p}_{to})\left(1 - \frac{\bar{p}_{to}}{\bar{P}_T - p_w}\right) + \left(f_{oi} - \frac{\bar{p}_{to}}{\bar{P}_T - p_w}\right)\bar{q}_i, \tag{3.26}$$

where $\bar{q}_i = \frac{1}{\mathcal{T}}\int_0^{\mathcal{T}} q_i(t)dt$ ($\mathcal{T}$ is the period of each DGC and we take this DGC-period to be a fixed value) and $\bar{P}_T = P_s$.

For the closed spiracle phase, we have

$$0 = D_o(p_o - \bar{p}_{to})\left(1 - \frac{\bar{p}_{to}}{\bar{P}_T - p_w}\right). \tag{3.27}$$

Note that for equations 3.26 and 3.27, we replace f_o by $\bar{p}_{to}/(\bar{P}_T - p_w)$ by making use of equation 3.8.

When $D_c \neq 0$, average values of p_{to} and p_{tc} can be determined by solving equations 3.18 and 3.19 for the open spiracle phase (3.20 and 3.21 for the closed spiracle phase) at steady state, with averaged values of P_T and q_i.

3.2.2.3 A mass balance model from the flexible trachea with gas exchange

If the tracheal volume (V_T) is assumed to be constant, then from equation 3.14 we have for the open spiracle phase

$$\frac{df_o}{dt} = \frac{1}{V_T}\left(\frac{dV_{to}}{dt}\right), \tag{3.28}$$

$$\frac{df_o}{dt} = \frac{1}{V_T}\left(D_o(p_o - p_{to}) + (f_{oi} - f_o)q_i\right). \tag{3.29}$$

Further, if the fluxes of oxygen and carbon dioxide are assumed to be of the same order and $\bar{q}_i$ is taken as the average flow though the trachea, then for the open spiracle phase, equations 3.18 and 3.19 are reduced to a standard mass balance model

$$D_o(\bar{p}_{to} - p_o) = \left(f_{oi} - \frac{\bar{p}_{to}}{\bar{P}_T - p_w}\right)\bar{q}_i, \tag{3.30}$$

where $\bar{p}_{to}$ and p_{to} are as previously defined.

For q_i given by

$$q_i = \begin{cases} \frac{\psi}{2}\nu\sin(\nu t), & 0 < t \leq \frac{\pi}{\nu}, \\ 0, & \frac{\pi}{\nu} < t \leq \frac{2\pi}{\nu}, \end{cases} \tag{3.31}$$

$$\bar{q}_i = \frac{\psi\nu}{2\pi}, \tag{3.32}$$

where ψ represents the volume of air displaced during the open spiracle phase when the insect is at rest (when metabolic activity is minimal) and ν is the ventilation frequency.

3.2.3 Model of oxygen uptake by mitochondria

In the tracheoles which are less than 1 μm in diameter, O_2 diffuses across the cytoplasm into the oxygen sink, the mitochondria, of adjacent cells. This is the slowest part of the final delivery of oxygen. The diffusion of O_2 in a water filled path is about 10^6 times less rapid than its movement in an air path. Hence, the closer the tracheoles are to the site of the mitochondria, the higher the rate of O_2 consumption that can be supported (i.e. tracheoles need to be within 10 μm of a mitochondrion to deliver sufficient O_2 to support active metabolism) [59]. The difference between the amount of O_2 that enters the cytoplasm from the tracheoles and the amount that sinks to the mitochondria (oxygen sink) of a respiring cell yields the rate of change in the partial pressure of oxygen

$$\frac{dp_o}{dt} = \frac{D_o}{v_{ct}\sigma}(p_{to} - p_o) - \frac{N_o T_m}{\sigma}\frac{dS}{dt}, \tag{3.33}$$

where p_o is the cell partial pressure, D_o is the diffusion capacity of oxygen, v_{ct} is the volume of the cytoplasm, σ is the solubility of oxygen, p_{to} is the tracheal partial pressure of oxygen, S is a saturation function of the mitochondria, T_m is the total concentration of mitochondria and N_o is the maximum number of oxygen molecules that each mitochondria can take. Many insect cells are usually 30 to 60 μm in diameter and tracheoles often touch and indent mitochondria [59]. The motivation for this model is shown in A.

If the hemolymph has the O_2 binding proteins, the hemocyanins, then

$$\frac{dp_o}{dt} = \frac{D_o}{V_h \sigma}(p_{to} - p_o) - \frac{N_o T_h}{\sigma}\frac{dS}{dt}, \tag{3.34}$$

where p_o is the hemocoel partial pressure of O_2, D_o is the diffusion capacity of O_2, V_h is the hemocoel volume, σ is the solubility of oxygen, p_{to} is the tracheal partial pressure of oxygen, S is the saturaton function of the hemocyanins, T_h is the total concentration of hemocyanin and N_o is the maximum number of molecules of oxygen that can bind to each molecule of hemocyanins.

For this study, we use equation 3.33 for the O_2 absorption by the mitochondria. Equation 3.33 is simple and a special case based on the assumptions made on the absorption phenomena. For simplicity, we assume that the mitochondria absorb O_2 according to

$$O_2 + M \rightleftharpoons_l^r MO_2, \tag{3.35}$$

where r and l are the rate constants for recombination and dissociation for the oxygen binding. In equation 3.33 we thus have that $N_o = 1$ for O_2 uptake by mitochondria. Let $\mathbf{x} \equiv x = [MO_2]$, i.e., x denotes the concentration of O_2-mitochondria combinations. We take the mitochondria saturation function S to be $S(x) = x/T_m$, and furthermore we assume that $dx/dt = g(x, p_o) = r\sigma p_o(T_m - x) - lx$. Equation 3.33 then becomes (see B)

$$\frac{dp_o}{dt} = \frac{D_o}{v_{ct}\sigma}(p_{to} - p_o) - \frac{N_o}{\sigma}(r\sigma p_o(T_m - x) - lx). \tag{3.36}$$

We no consider only the process of oxygen diffusion (equation 3.33) and introduce the following non-dimensional parameters

$$p_r = \frac{p_o}{p_{to}}, \qquad \tau = \frac{D_o}{\sigma v_{ct}}t, \tag{3.37}$$

$$\alpha = \frac{N_o T_m}{\sigma p_{to}}, \qquad \beta = \frac{r\sigma^2 v_{ct}}{D_o}p_{to}, \tag{3.38}$$

$$\tilde{x} = \frac{x}{T_m}, \qquad \gamma = l/(r\sigma p_{to}). \tag{3.39}$$

Substituting the above non-dimensional parameters into equation 3.33 and saturation function S, we obtain

$$\frac{dp_r}{d\tau} = 1 - p_r - \alpha\frac{d\tilde{S}}{d\tau}, \tag{3.40}$$

$$\frac{d\tilde{x}}{d\tau} = \beta G(\tilde{x}, p_r), \tag{3.41}$$

$$\tilde{S} = \tilde{x}, \tag{3.42}$$

where

$$G(\tilde{x}, p_r) = (1 - \tilde{x})p_r - \gamma\tilde{x}. \tag{3.43}$$

The physical meaning of α and β is explored. α is the ratio of the maximum amount of O_2 that could be taken up by the mitochondria and the maximum amount of oxygen that could be available as dissolved gas (i.e. N_oT_m measures the maximum amount of $)_2$ that could be taken up by the mitochondria). Since α compares two quantities, we consider it as the size factor. β is the ratio of the maximum rate of O_2 uptake by a respiring cell to the rate of O_2 supply from the tracheoles. β is regarded as a rate factor.

We would expect $\beta \gg 1$ whenever the process of O_2 uptake by mitochondria is much faster than the process of oxygen diffusion. To understand this, the system of equations 3.40−3.42 is analyzed in the phase plane $(p_r, \tilde{S})$. We first let $\alpha = 0$ (i.e $dp_r/d\tau = 1 - p_r$. This gives a non-physiological model and its solution equals $p_r(\tau) = e^{-\tau}(e^{\tau}-1-p_r(o)))$. Then $|d\tilde{x}/d\tau| \gg |dp_r/d\tau|$ until $G(\tilde{x}, p_r) \approx 0$. In this case, the dynamics can be divided into two phases:

- a fast transient where $|d\tilde{x}/d\tau| \gg |dp_r/d\tau|$ when $G(\tilde{x}, p_r) \neq 0$, and
- a slow transient where $G(\tilde{x}, p_r) \approx 0$.

Secondly, when $\alpha \neq 0$ and large enough (as under physiological conditions), the trajectories in the $(p_r, \tilde{S})$ space are trapped between the nullclines $\tilde{x} = p_r/(\gamma + p_r)$ at which $d\tilde{x}/d\tau = 0$ and $\tilde{x} = (p_r(\alpha\beta + 1) - 1)/(\alpha\beta(\gamma + p_r))$ at which $dp_r/d\tau = 0$. For $\alpha\beta \gg 1$, the trajectories in this space move relatively fast towards the nullcline for $\tilde{S}$, and close to this nullcline the dynamics is such that the trajectories follow this nullcline (towards an attractor) as determined by the dynamics of p_r. Therefore, for $\alpha \neq 0$ and $\beta \gg 1$, the transient towards the saturation function is faster than when $\alpha = 0$ and a small β (see C). In other words, the process of O_2 absorption by the mitochondria reaches equilibrium rapidly and remains near equilibrium while the amount of dissolved O_2 in the trachea is above the endotracheal oxygen partial pressure threshold that trigger spiracle opening (perfusion experiments indicate that spiracles open when endotracheal oxygen partial pressure is below a certain threshold that trigger spiracles to open [87, 88, 91]). A plot of the vector field, nullclines, and equilibrium points for $\alpha \neq 0$ is given in figure 3.4.

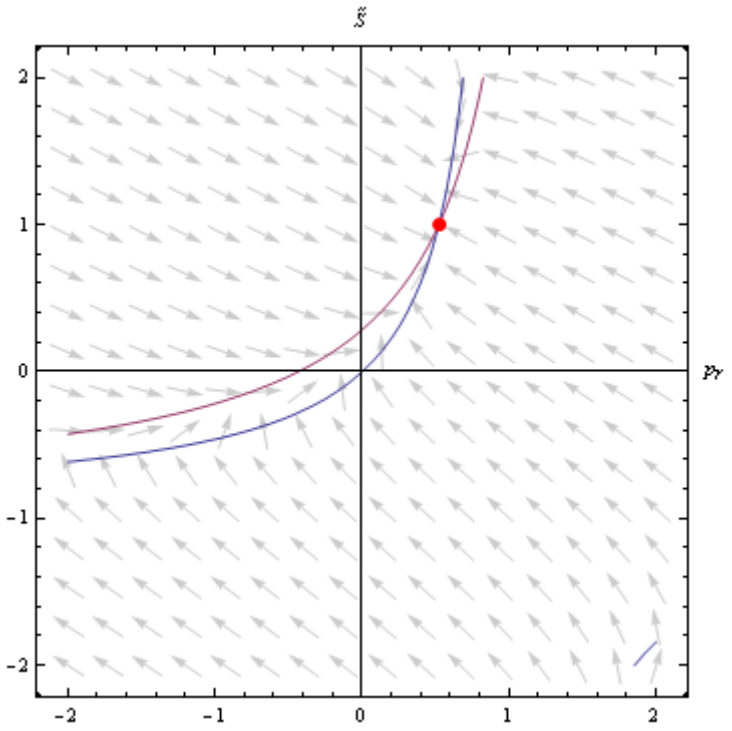

FIGURE 3.4: Vector field, nullclines and equilibrium point for the system of equation 3.40−3.41.

Ignoring the fast transient and taking only the slow transient into account, the solution $\tilde{S}$ can be expressed by another function $\tilde{G}$ in terms of partial pressure as

$$\tilde{S} = \tilde{G}(p_r), \quad \text{and} \tag{3.44}$$

$$\frac{d\tilde{S}}{d\tau} = \frac{d\tilde{G}}{dp_r}\frac{dp_r}{d\tau}. \tag{3.45}$$

Recall that on the nullcline $dfracd\tilde{S}d\tau = 0$, we have

$$\tilde{S} = p_r/(\gamma + p_r) \quad \Longrightarrow \quad \tilde{G} = p_r/(\gamma + p_r). \tag{3.46}$$

Substituting this expression into equation 3.40, the non-dimensional form is given by

$$\frac{dp_r}{d\tau} = 1 - p_r - \alpha\frac{d\tilde{S}}{d\tau}, \tag{3.47}$$

$$= 1 - p_r - \alpha\frac{d\tilde{G}}{dp_r}\frac{dp_r}{d\tau}, \tag{3.48}$$

$$\frac{dp_r}{d\tau} = \left(1 + \alpha\frac{d\tilde{G}}{dp_r}\right)^{-1}(1 - p_r). \tag{3.49}$$

The dimensional form is given by

$$\frac{dp_r}{d\tau} = \left(1 + \alpha \frac{d\tilde{G}}{dp_r}\right)^{-1} (1 - p_r), \tag{3.50}$$

$$\frac{\sigma v_{ct}}{D_o} \frac{1}{p_{to}} \frac{dp_o}{dt} = \left(1 + \frac{N_o T_m}{\sigma} \frac{d\tilde{G}}{dp_o}\right)^{-1} \left(1 - \frac{p_o}{p_{to}}\right), \tag{3.51}$$

$$\Rightarrow \frac{dp_o}{dt} = \frac{D_o}{\sigma v_{ct}} (p_{to} - p_o) \left(1 + \frac{N_o T_m}{\sigma} \frac{d\tilde{G}}{dp_o}\right)^{-1}. \tag{3.52}$$

Recall from equation 3.8 that $p_{to} = f_o(P_T - p_w)$,

$$\therefore \quad \frac{dp_o}{dt} = \frac{D_o}{\sigma v_{ct}} (f_o(P_T - p_w) - p_o) \left(1 + \frac{N_o T_m}{\sigma} \frac{d\tilde{G}}{dp_o}\right)^{-1}, \tag{3.53}$$

where $\tilde{G}(p_o)$ is the mitochondria saturation function as defined previously in equation 3.46. The oxygen partial pressure of the respiring cell is given by the balance between the amount of oxygen that enters the cell from the tracheoles and the amount of oxygen that is absorbed by the mitochondria and is given by equation 3.53.

The dimensional saturation function used in this study is given by

$$G(p_o) = \frac{r\sigma p_o}{l + r\sigma p_o}, \tag{3.54}$$

and

$$\frac{dG(p_o(t))}{dp_o} = \frac{\sigma}{l + r\sigma p_o(t)} - \frac{r^2\sigma^2 p_o(t)}{(l + r\sigma p_o(t))^2}. \tag{3.55}$$

The model of oxygen uptake by the mitochondria as in equation 3.54 is shown in figure 3.5. The kinetics of oxygen absorption was calculated with $\sigma = 3.3\times10^{-5}\ mol\ l^{-1}\ mmHg^{-1}$, $r = 3.6\times10^{6}\ lmol^{-1}s^{-1}$ and $l = 26.8\ s^{-1}$. Figure 3.5 can be regarded as the projection of the phase space into the plane (p_o, S). In fact, the saturation curve in equilibrium is a projection of the curve $g(\mathbf{x}, p_o) = 0$ in equation B.1 (the saturation curve is one of the nullclines in the system). The arrows indicate the direction of time. Figure 3.5 shows that the solution tends rapidly to a region where O_2 absorption by the respiring cell is near equilibrium.

3.2.3.1 Mass balance and Fick's principle based average model of oxygen flux

Define $\mathcal{T}_T$ as the time between each cell's/cytoplasm uptake of O_2 in the trachea (i.e. transit time in the trachea). The average flux of oxygen into the respiring cells can be estimated by

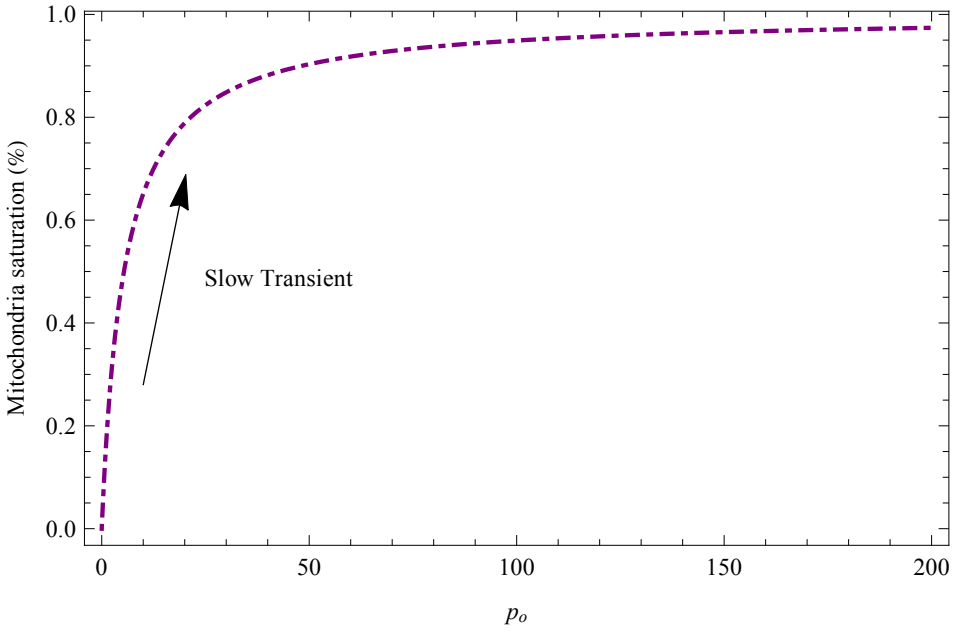

FIGURE 3.5: Kinetics of oxygen absorption by the mitochondria when metabolic activity is minimal during rest at 25^oC. The arrow indicates the direction of time.

(see equation 3.33)

$$\begin{aligned} D_o(\bar{p}_{to} - \bar{p}_o) &\triangleq \frac{1}{\mathcal{T}_T}\int_0^{\mathcal{T}_T} D_o p_{to} dt \\ &= \frac{1}{\mathcal{T}_T}\int_0^{\mathcal{T}_T} v_{ct}\left(\sigma\frac{dp_o}{dt} + N_o T_m \frac{dS}{dt}\right) dt \\ &= \frac{v_{ct}}{\mathcal{T}_T}[\sigma(p_o(\mathcal{T}_T) - p_o(0)) + N_o T_m(S(\mathcal{T}_T) - S(0))]. \end{aligned} \tag{3.56}$$

Further, the saturation function S can be expressed as

$$S = f(\mathbf{x}), \tag{3.57}$$

where $\mathbf{x}$ is a vector of state variables. Then equation 3.56 can be expressed as

$$D_o(\bar{p}_{to} - \bar{p}_o) = \frac{v_{ct}}{\mathcal{T}_T}[\sigma(p_o(\mathcal{T}_T) - p_o(0)) + N_o T_m(\tilde{f}(p_o(\mathcal{T}_T)) - \tilde{f}(p_o(0)))]. \tag{3.58}$$

Equation 3.58 illustrates Fick's principle [94–96] which states that the rate of O_2 uptake by the respiring cells is equal to flow into the cytoplasm (given by $v_{ct}/\mathcal{T}_T$) multiplied by the difference between O_2 content of the tracheoles and the mitochondria.

3.2.4 Carbon dioxide transport

Levenbook and Clarke [70] demonstrated that CO_2 transport in the haemolymph of larva *Gasterophilus intestinals* de Geer (Diptera) occurs largely in the form of bicarbonate. Earlier, Bishop [97] found that 29.2 vol.% CO_2 in bee-larva blood while Babers [98] reported 10.03 vol.% CO_2 in *Prodenia eridamia* blood. In both these cases, it can be calculated that about four-fifth of the total CO_2 was not in solution. Levenbook and Clarke [70] also reported cases where it was hypothesized that it is probable that of the $9.24 - 81.21$ vol.% CO_2 present in the blood of various insects, only a small fraction could be dissolved. These authors further propose that there are more than 5 forms in which CO_2 may be transported in insect blood, viz., dissolved anhydrase, carbonic acid-H_2CO_3, bicarbonate-$BHCO_3$, carbomate-$R.NH.COOH$, and Y-bound CO_2. In our study, we consider the case where CO_2 is transported in the form of a bicarbonate. Levenbook and Clarke [70] showed that the quantity of bicarbonate present in the haemolymph is a function of both the available base and the carbonic acid concentration, with the carbonic acid being directly proportional to the amount of gaseous CO_2 in the blood. At the fluid filled tips of the tracheoles, the bicarbonate (HCO_3^-) is assumed to bind to hydrogen ions (H^+) to produce carbon dioxide (CO_2) and water (H_2O).

The high solubility of CO_2 in an aqueous solution enables insects to accumulate HCO_3^- according to the following reaction

$$CO_2 + H_2O \underset{\delta l_2}{\overset{\delta r_2}{\rightleftharpoons}} H^+ + HCO_3^-, \tag{3.59}$$

where l_2 is the hydration reaction rate and r_2 is the dehydration reaction rate. The buffering capacity of the hemolymph helps in solubilizing CO_2 as bicarbonate and this keeps gaseous CO_2 from building up in the tracheal system [59]. At some point, the relationship between gaseous O_2 and CO_2, and HCO_3^- in solution reaches an equilibrium at which the tracheal tension of CO_2 and O_2, or pH change in the hemolymph, triggers spiracle opening and release of CO_2 from the hemolymph as gas [45, 59]. In the chemical reaction described by (3.59), we introduce a stabilizing parameter $\delta > 0$ which captures the buffering capacity of the hemolymph in solubilizing CO_2 as a bicarbonate.

When diffusion across the tracheole wall and cell membranes is taken into account, we adopt the following system of ordinary differential equations

$$\left.\begin{aligned} \frac{dp_c}{dt} &= \frac{D_c}{\sigma_c v_{ct}}(p_{tc} - p_c) + \frac{\delta l_2}{\sigma_c} hy - \delta r_2 p_c, \\ \frac{dy}{dt} &= \delta r_2 \sigma_c p_c - \delta l_2 hy, \\ p_{tc} &= f_c(P_T - p_w), \end{aligned}\right\} \tag{3.60}$$

p_c is the cytoplasm partial pressure of CO_2, D_c is the diffusion capacity of CO_2, σ_c is the solubility of CO_2, y is the concentration of bicarbonate, h is the concentration of hydrogen ions and p_{tc} as before is the CO_2 tracheal partial pressure. For the open spiracle phase, the rates of change of P_T and f_c are given by equations 3.13 and 3.19. For the closed spiracle phase df_c/dt is given by equation 3.21.

When O_2 uptake by the mitochondria and CO_2 release are considered during the open spiracle phase, the system of ordinary differential equations 3.18, 3.19, 3.25, 3.53 and 3.60 describes gas exchange in a flexible trachea (for the closed spiracle phase we consider equations 3.20, 3.21, 3.25, 3.53 and 3.60). Solving the system of ordinary differential equations for a given set of initial values simulates the movement of the respiratory gases. Gas exchange is a continuous process, and the O_2 and CO_2 partial pressures at the tips of the tracheoles depend on metabolic activity. The concentration of bicarbonate, y, is initialized such that $dy/dt = 0$. This process is illustrated for p_o in figure 3.6(a). Figure 3.6(b) illustrates the time evolution of the bicarbonate.

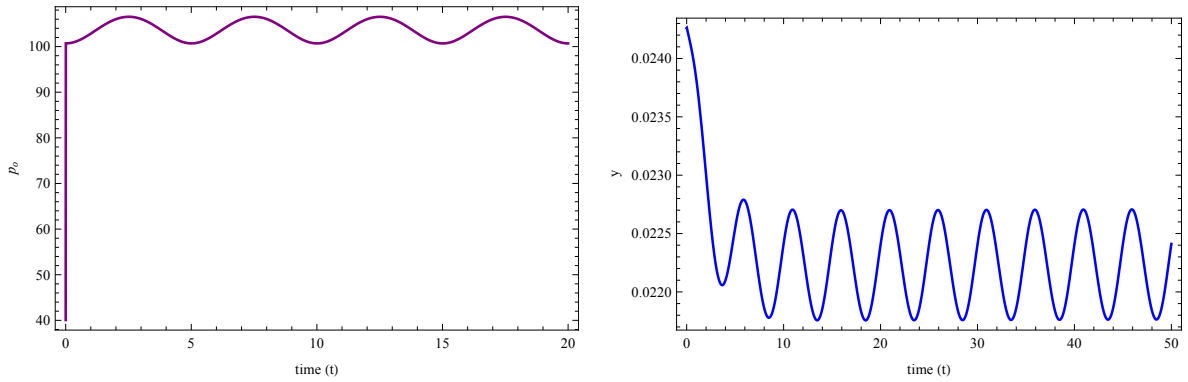

FIGURE 3.6: Kinetics of the cell partial pressures. (a) The values of the cell partial pressures are initialized at the beginning of the *DGC* process. (b) The concentration of the bicarbonate as the process of gas exchange occurs. Note that the oscillations are due to the combined effects of diffusion and ventilation.

3.3 Results

We summarize numerical simulations of the discussed models. We hope the simulations will validate experimental data collected and provide new insights into the physiological system of the insect under study. Unless otherwise stated in the text, the hemocoel/cytoplasm pressure is given by

$$P_B = P_s - 0.2R_s\nu\sin(\nu t) - E_T(2.5 - 0.2\cos(\nu t)), \tag{3.61}$$

where ν is the ventilation frequency.

The parameters and variables that appear frequently in this manuscript are listed in E. All simulations were carried out using *Wolfram Mathematica 9.0*.

3.3.1 Reducing the flexible tracheal model with gas exchange to flexible tracheal model

If $D_o = D_c = 0$, the flexible model with gas exchange (section 3.2.2) reduces to the flexible tracheal model (section 3.2.1). By solving the flexible tracheal model when $D_o = D_c = 0$ we can obtain the tracheal concentrations of O_2 and CO_2. For the open spiracle phase, we then have

$$\frac{df_o}{dt} = \frac{1}{V_T}(f_{oi} - f_o)q_i, \tag{3.62}$$

$$\frac{df_c}{dt} = \frac{1}{V_T}(f_{ci} - f_c)q_i, \tag{3.63}$$

and $df_o/dt = df_c/dt = 0$ for the closed spiracle phase.

For the open spiracle phase, if the concentrations of O_2 in the tracheal air are different from the concentrations in ambient air, we expect the concentrations to equilibrate over time. Also worth noting is that f_o and f_c can be at equilibrium while P_T oscillates.

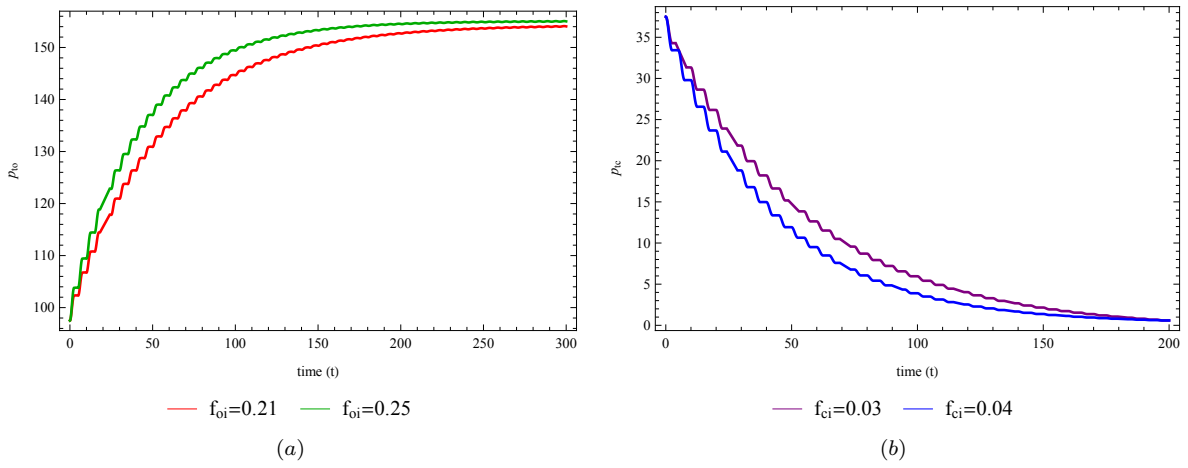

FIGURE 3.7: Flexible tracheal model with gas exchange when $D_o = D_c = 0$. (a) Tracheal pressure of oxygen. Solid line: $f_{oi} = 0.25$, Dashed line: $f_{oi} = 0.21$. (b) Tracheal pressure of carbon dioxide. Solid line: $f_{ci} = 0.04$, Dashed line: $f_{ci} = 0.03$.

Figure 3.7 shows numerical simulations of equations 3.20, 3.21 and 3.25, with $D_o = D_c = 0$. We vary the concentrations of O_2 and CO_2 in ambient air. The tracheal pressure of O_2 and CO_2 during the open spiracle phase is shown in graph (a) and (b), respectively. As expected, the partial pressure of CO_2 converges towards zero during this phase. We would also expect the partial pressure of O_2 to converge to $0.21 \times (P_s - p_w)$ during this open spiracle phase, (note

that the partial pressure oscillates around these values). Also seen is that when the ambient air concentration of O_2 is higher on average, the solutions for p_{to} converge faster towards the steady state solutions. The result serves to validate the flexible tracheal model with gas exchange.

3.3.2 Closed spiracle phase

The closed spiracle phase is the case where there is cellular gas exchange and no external ventilation. Figure 3.8 shows the tracheal partial pressures of oxygen and carbon dioxide when the spiracles are completely sealed as simulated by the flexible tracheal model with gas exchange ($D_c = 5.1 \times 10^{-4}\ mols^{-1}mmHg^{-1}$ and $D_o = 3.7 \times 10^{-4}\ mols^{-1}mmHg^{-1}$). We solve equations 3.20, 3.21 and 3.25 numerically using *NDSolve in Mathematica 9.0*. For this model, p_o and p_c are kept constant. This mimics infinite velocity of the gas molecules with constant metabolism. It can be seen that the partial pressures in the trachea eventually equilibrate with the respiring cell partial pressures.

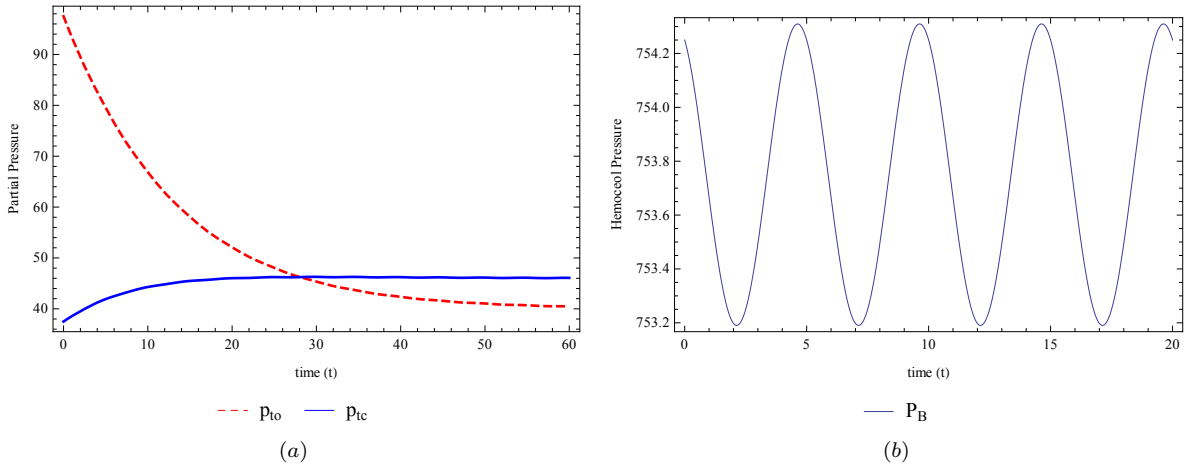

FIGURE 3.8: Closed spiracle phase model with cellular gas exchange. (a) Tracheal pressure of oxygen (p_{to}) and carbon dioxide (p_{tc}). (b) Cytoplasm pressure, $P_B(t)$.

The time it takes for both p_{to} and p_{tc} to reach steady state is shorter in figure 3.8 than it is in figure 3.7. This makes sense since constant cytoplasm partial pressures mimic infinite gas velocity and hence the rate of gas exchange is maximized. These results are consistent with the literature about effects of ventilation and perfusion on the partial pressure of tracheal gases. Forster [85] performed 35 perfusion experiments to estimate spiracle behaviour for most gas mixtures. He found that usually steady-state was reached within the first hour after changing the gas composition. Lighton [45] provides a threshold of 4 kPa (30.0025 $mmHg$) while Levy and Schneiderman [10] cited a threshold of 2-6 kPa for endotracheal p_{tc}. Direct measurement of endotracheal p_{to} with microelectrodes in *Attucus* pupae gave values around 4-5 kPa [86]. Hetz and Bradley [24] further demonstrated active regulation of endotracheal p_{to} down to about

30.0025 $mmHg$ during the closed spiracle phase. The measured p_{to} and p_{tc} thresholds presented in the literature are consistent with our model predictions. If we define $\bar{q}_i$ as the average ventilation and $\bar{Q}_T$ as the average flux of gas into the trachea, then $\bar{q}_i/\bar{Q}_T = 0$ during the closed spiracle phase.

3.3.3 The flexible tracheal model vs the average model and the mass balance model

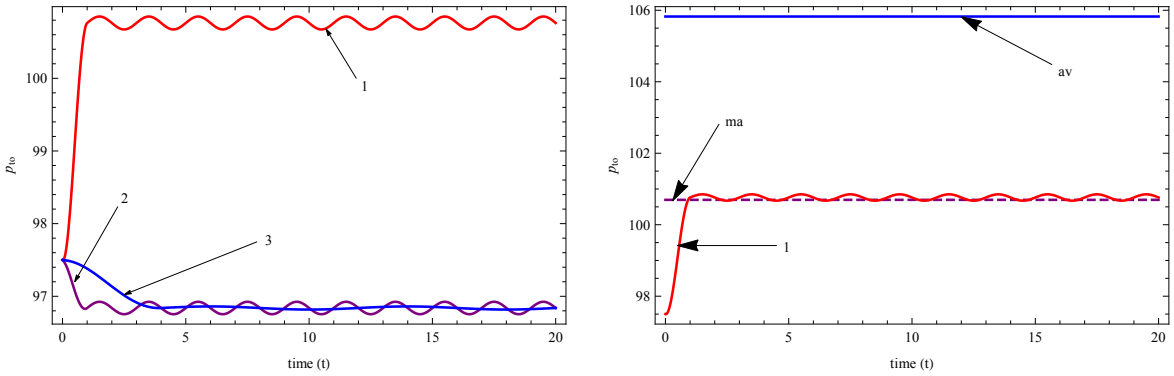

FIGURE 3.9: (a) Effect of ventilation on the partial pressure of oxygen when simulated by the flexible tracheal model with gas exchange. (b) Comparison of steady state solutions of the flexible trachea model with gas exchange with estimated average solutions. **av**-Calculated average solution (equation 3.26). **ma**-Mass balance model (equation 3.30).

The numerical simulations of the flexible tracheal model with gas exchange (section 3.2.2) are shown in figure 3.9(a) for three ventilation rates: Graph **1** - calculated numerically with $f_{oi} = 0.2121$, $\nu = \pi$ and $D_c = 0$; Graph **2** - calculated numerically with $f_{oi} = 0.1071$, $\nu = \pi$ and $D_c = 0$; Graph **3** - calculated numerically with $f_{oi} = 0.1071$, $\nu = \pi/4$ and $D_c = 0$. The average models, equations 3.26 and 3.30, qualitatively explain the results seen in figure 3.9(a). The steady state solutions depend on the balance between the amount of oxygen supplied by ventilation and the amount taken up by the respiring cells.

Figure 3.9(b) shows the quantitative comparison between the models; the standard mass balance model of equation 3.30, the average model of equation 3.26 and the flexible tracheal model with gas exchange. One steady-state solution of the flexible model with gas exchange is shown in figure 3.9(b): Graph **1** - calculated numerically with $f_{oi} = 0.2121$, $\nu = \pi$ and $D_c = 0$. An analytic solution of the average model obtained by using the same parameters as those of Graph **1** is plotted by a solid line marked with "**av**". The analytic solution of the mass balance model (also obtained by using the same parameters as those in Graph **1**) is plotted by a dashed line marked with "**ma**".

As can be seen in figure 3.9(b), the mass balance model (equation 3.30) yields a good approximation of the average partial pressure of tracheal oxygen (at least) for the given function of $P_B(t)$ when $D_c = 0$. However, we would expect the calculated average model to yield a better approximation in the more realistic case when $D_c \neq 0$.

When $D_c \neq 0$, define the respiratory ratio as $D_o(\bar{p}_{to} - p_o)/D_c(\bar{p}_{tc} - p_c)$ where $\bar{p}_{to}$ and $\bar{p}_{tc}$ are the average partial pressures of oxygen and carbon dioxide, respectively. In this case, the respiratory ratio equals 0.273586. The respiratory ratio value determined by the calculated average model is larger than that calculated by the mass balance model.

3.3.4 External conditions and oxygen uptake by the mitochondria

Ambient conditions can shift the chemical process of O_2 absorption by the mitochondria away from the saturation curve. Equally, internal conditions such as the tracheal partial pressure and the diffusion capacity affect the chemical process of O_2 absorption. For the open spiracle phase, the system of equations 3.33, B.1 and B.2 were reduced to a single equation 3.53. In fact, under ideal or normal conditions, the process of oxygen diffusion in the insect tracheal system can best be described by equation 3.53. For simplicity and model simulations, $\beta \approx 3300$ and $\alpha \approx 1$ (values used in the calculation are: $r = 3.6 \times 10^6\ lmol^{-1}s^{-1}$, $\sigma = 1.4 \times 10^{-4}\ moll^{-1}mmHg^{-1}$, $D_o = 1.56 \times 10^{-5}\ mols^{-1}mmHg^{-1}$, $p_{to} = 104\ mmHg$, $v_{ct} = 0.07\ l$ and $T_m = 2 \times 10^{-3}\ moll^{-1}$).

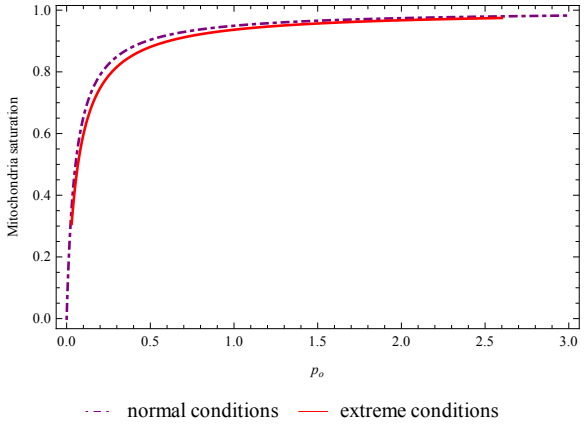

FIGURE 3.10: Dynamics under extreme conditions. Dotted line: solution of the equations 3.33 and B.1 under normal conditions. Solid line: solution under extreme conditions.

Under extreme physiological conditions, it is not clear if equation 3.53 is still valid. Figure 3.10 shows an example of the dynamics under extreme conditions (kinetics of O_2 uptake calculated with $\sigma = 1.1 \times 10^{-4}\ moll^{-1}mmHg^{-1}$, $r = 3.6 \times 10^6\ lmol^{-1}s^{-1}$ and $l = 26.8\ s^{-1}$). The tracheal pressure of O_2 is twice the assumed normal value and the diffusion capacity is about three times the assumed normal value (e.g. when the insect needs to move rapidly to escaper danger).

As seen from figure 3.10, the solution (marked with a solid line) does not follow the equilibrium even though the initial conditions lie on the saturation curve (marked with dashed line). Even though the O_2 uptake by the mitochondria did not change (r and l), the ratio between these rates and tracheal partial pressure plus the diffusion capacity did change. These changes affected the model system dynamics.

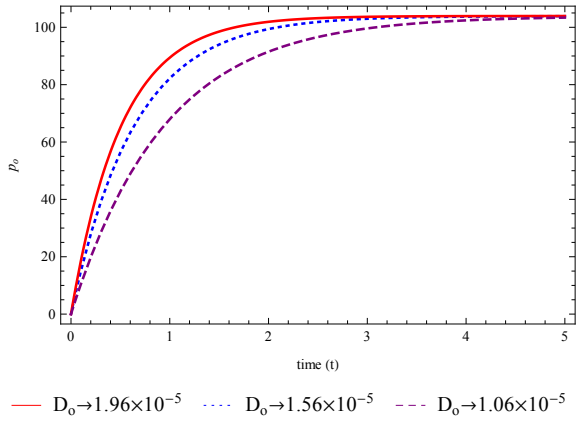

FIGURE 3.11: Shifts in the saturation curve as a result of changes in the oxygen tracial partial pressure. Dotted line: $D_o = 1.56 \times 10^{-3} ls^{-1} mmHg^{-1}$, Solid line: $D_o = 1.96 \times 10^{-3} ls^{-1} mmHg^{-1}$, and Dashed line: $D_o = 1.06 \times 10^{-3} ls^{-1} mmHg^{-1}$. All other parameters are the same as defined before.

In section 3.2.3, the non-dimensionalization analysis was performed by assuming a constant p_{to} (tracheal partial pressure of O_2) and by ignoring the ventilation process. Figure 3.11 indirectly shows shifts from the saturation under extreme conditions in the system of equations 3.18, 3.19, 3.25, 3.33 and B.1 where the kinetics of O_2 absorption by the mitochondria and the mechanics of ventilation are included. Figure 3.11 shows shifts in the respiratory cell partial pressure when the mechanics of ventilation is included. The solution of equation 3.33 where the kinetics of oxygen absorption by the mitochondria was calculated by equation 3.54 is simulated for different values of D_o. As can be seen, for higher values of the diffusion capacity and tracheal partial pressure of O_2, the respiring cell partial pressure quickly reaches steady state.

External conditions such as the tracheal partial pressure and the oxygen diffusion capacity can shift the chemical process of O_2 uptake by the mitochondria away from the saturation curve in equilibrium. It is hypothesized that shifts in the saturation curve also occur as a result of changes in temperature, binding to hydrogen ions and carbon dioxide to the mitochondria, and changes in the concentration of carbonic acid within the respiring cells.

Figure 3.12(a) shows how shifts in the saturation curve affect the tracheal partial pressure of O_2. Equations 3.18, 3.19, 3.25, 3.53 and 3.60 were solved numerically while simulations were carried out by varying the hydration coefficient, l, and dehydration coefficient, r, in the saturation curve (equation 3.54). Saturation curves for different values of l are shown in figure 3.12(b). As can be seen, small shifts in the saturation curve have significant effect on tracheal partial pressure.

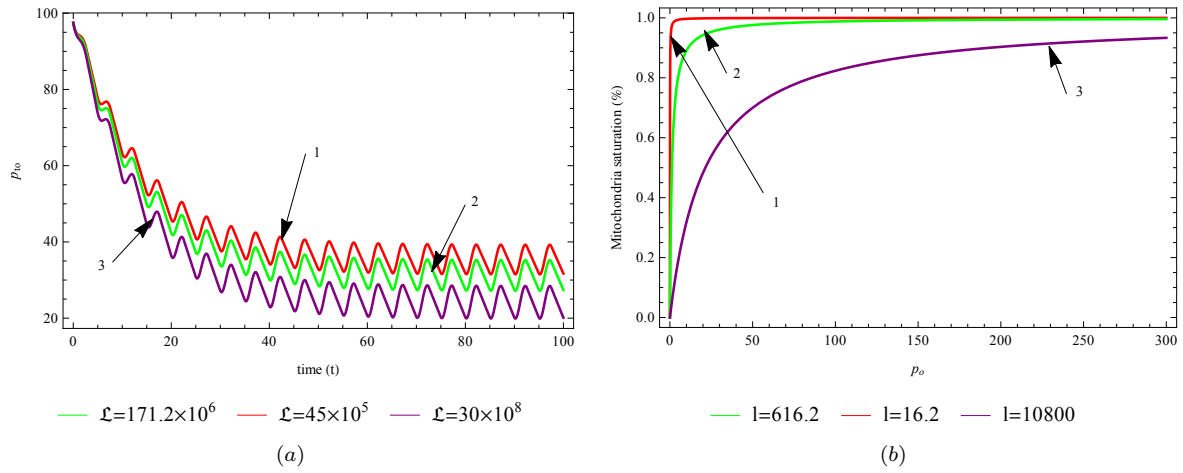

FIGURE 3.12: $\mathfrak{L} = l/r$. (a) Effects of shifts in the saturation curve on tracheal partial pressure of oxygen. (b) The saturation curves. Graph 1: $l/r = 45 \times 10^5$ (reduced temperature); Graph 2: $l/r = 171.2 \times 10^6$; Graph 3: $l/r = 30 \times 10^8$ (increased temperature). Solutions found by numerically solving equations 3.18, 3.19, 3.25, 3.53 and 3.60 using *NDSolve in Mathematica 9.0*.

These results are best explained qualitatively by using the conservation of mass principle and Fick's principle (see equation 3.58). A shift in the mitochondria saturation function changes the amount of O_2 that can be delivered from the tracheoles. Thus, this results in changes in the tracheal oxygen partial pressure. An increase in the uptake of O_2 by the mitochondria results in decreased tracheal oxygen partial pressure. If oxygen uptake by the mitochondria and tracheal oxygen partial pressure are in equilibrium at the tips of the tracheoles, then equation 3.53 can be used even if the chemical process (3.35) is not close to equilibrium all the time.

3.3.5 The role of the closed spiracle phase and carbon dioxide emission time

We solve the system of equations 3.18, 3.19, 3.25, 3.53 and 3.60 to calculate the respiratory cell partial pressure of carbon dioxide for $\delta = 0.3$ as the baseline parameter value. This value has no significant meaning in this context and was chosen for simplicity and model simulations. A better model for carbon dioxide transport still needs to be developed. Nevertheless, equation 3.60 still depicts the dynamics of CO_2 transport.

Figure 3.13 depicts time simulations of the chemical reaction (3.59) when the reaction is not coupled with either the diffusion or to the ventilation process. As can be seen, different values of δ result in different equilibrium times (see D for the calculations of the reaction rates). Time simulations are for $H^+ = 10^{-7.4}\ moll^{-1}$, $r_2 = 0.12\ s^{-1}$, $l_2 = 164{\times}10^3\ ls^{-1}mol^{-1}$, $CO_2(0) = 46\sigma_c\ moll^{-1}$ and $HCO_3^-(0) = (40\sigma_c r_2)/(l_2 H^+)\ moll^{-1}$.

Figure 3.14(a) shows the model simulations when the chemical reaction is coupled with diffusion and ventilation (solving equations 3.18, 3.19, 3.25, 3.53 and 3.60). The numerical simulations

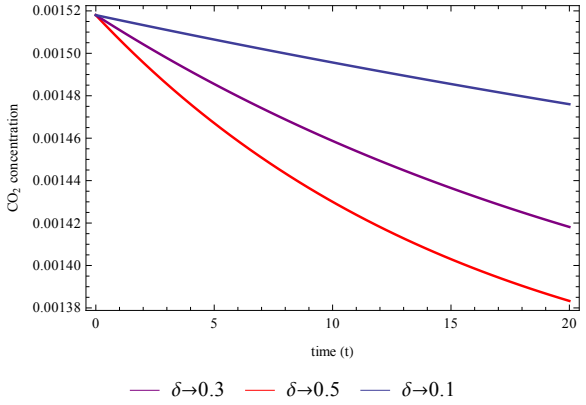

FIGURE 3.13: Time simulations of the chemical reaction (3.59) for different values of δ.

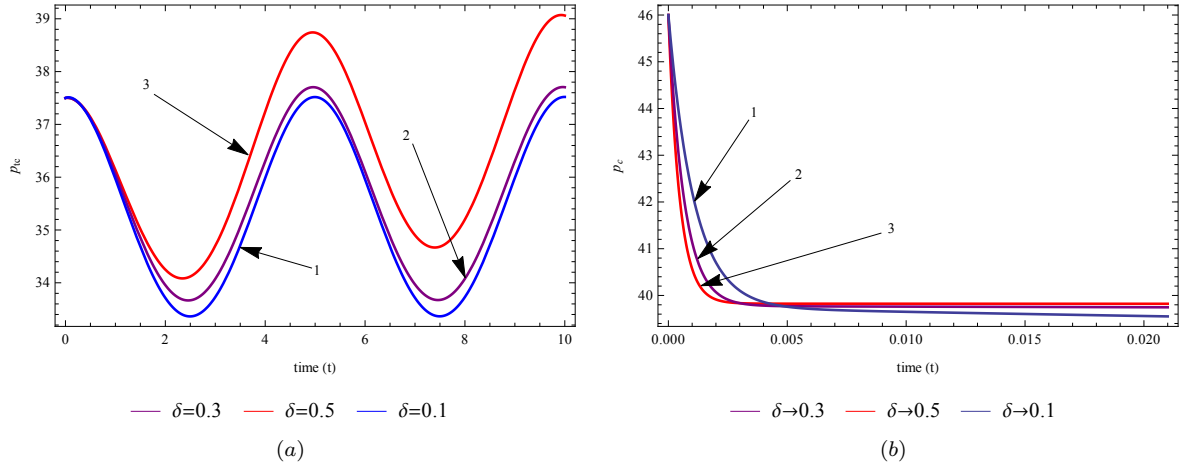

FIGURE 3.14: Simulations of the chemical reaction (3.59). (a) Effects of changes in the reaction rate on the tracheal partial pressure of CO_2. (b) Time simulations of the chemical reaction in equation for different values of δ.

were carried out with three different values of δ (Graph **1**: $\delta = 0.1$, Graph **2**: $\delta = 0.3$ and Graph **3**: $\delta = 0.5$). The tracheal partial pressure of CO_2 is very sensitive to δ and therefore to the duration of the closed spiracle phase. A rapid reaction allows more carbon dioxide to be released into the trachea, resulting in an increase in the tracheal partial pressure of CO_2 and a shortened closed spiracle phase.

Figure 3.14(b) show time simulations of the respiratory cell partial pressure of CO_2 (p_c) when coupled to either diffusion or to the ventilation process (solution of equation 3.60). When the chemical reaction is coupled with diffusion and ventilation, the solution quickly reaches steady state (compare both axes (especially the times) in figures 3.13 and 3.14(b)).

3.4 Discussion and conclusions

This research paper provides simple models of respiratory gas exchange in the insect tracheal system. The models attempt to quantitatively explain the nonlinear phenomena of *DGC* observed in some insects. Although *DGC* is to the best of our knowledge not yet fully understood, we hope this study will lead to even more detailed quantitative investigations into *DGC*.

Section 4.2 presented the mathematical models for the tracheal system. Two models for the trachea were presented; (1) flexible trachea and (2) flexible trachea with gas exchange. We also showed how the models are related to each other and how they are related to Krogh's diffusion equation which is generally used for modeling insect respiration [71, 72]. Section 3.2.2.1 presented a simplified model for a flexible trachea. The idea was that simplified models are easier to understand and provide more insight to the system while detailed models provide more accurate quantitative information as illustrated in section 3.3. The numerical results obtained by the more complex models can be qualitatively explained by the simplified models.

The assumption that the process of O_2 absorption by the mitochondria is near equilibrium was explained in section 3.3.4. It was shown that external conditions such as partial pressure and the diffusion capacity can shift the chemical process of O_2 absorption by the mitochondria away from the saturation curve in equilibrium. However, it was hypothesized that if the process of O_2 absorption by the mitochondria is in equilibrium in the cells adjacent to the tracheoles, then the tracheal partial pressure of oxygen will not be affected even if the chemical process (3.59) is not close to equilibrium.

The derived models were validated both analytically (section 3.2.2.1) and numerically (sections 3.3) by the fact that they can be reduced to simpler known models. The numerical results in section 3.3 were consistent with what is found in the literature. The results in sections 3.3.2 and 3.3.4 were consistent with perfusion experiments (see [24, 45, 85–87]). The numerical results showed the same qualitative effect, of internal control systems that generate *DGC*, as in published data (see [27]). The closed spiracle phase represents $\bar{q}_i/\bar{Q}_T = 0$ while the open spiracle phase presents $\bar{q}_i/\bar{Q}_T = \infty$. Figure 3.8 showed that cases between these extremes were also consistent with experimental data [10, 24, 86]. Figure 3.6 showed that under "normal" conditions, the cell partial pressure of oxygen oscillated around 100 and 110 $mmHg$.

The model parameters all have physiological meanings. However, their physiological values are to the best of our knowledge not all known. For the unknown parameter values, the presented values were chosen for simulation purposes. Parameters δ and $\mathfrak{L} = l/r$ were introduced and can be related to chemical reactions. Changes in molecular level can shift the saturation curve of the mitochondria (variation of $\mathfrak{L} = l/r$). Changes in the length of the closed spiracle phase were simulated by the variation of δ. Sections 3.3.4 and 3.3.5 showed that variations in l and δ affected the tracheal partial pressures considerably.

We have presented two diffusion and convection based models of DGC in the insect trachea. The model for open spiracle phase will also apply to insects which have continuously open spiracles for gas exchange. Models for the human lung were modified for use in insect respiration since the functions of these two systems are similar, i.e gas exchange. In addition, we have developed low-order expressions for the tracheal partial pressures of oxygen and carbon dioxide, the rate of changes of the gas concentrations, and the rate of the tracheal volume change. The expressions clearly showed the effect of the spiracle opening and closing on net flow. The expressions also predicted a transfer of mass from the trachea to the respiring cells.

Better models that rigorously show how the kinetics of oxygen absorption by the mitochondria and how the chemical reactions associated with carbon dioxide release are related to the linear relationship between partial pressure and the total amount of gases in the trachea are still to be investigated. Further, time delays due to the differences in the diffusion rate of oxygen and carbon dioxide are viewed as part of the feedback process and have not been included in the model. Even though our models were limited, some insights about the movement of gases within the trachea were significantly highlighted.

Chapter 4

A mathematical model for insect trachea wall contractions in respiratory gas flow

The work in this chapter has been submitted to *Mathematical Biosciences.*

We present a paradigm for selectively pumping and controlling gases at the microscale in a complex network of channels. The study is inspired by the internal flow distributions of respiratory gases produced by rhythmic wall contractions in insect tracheal networks. Gas is considered as a fluid. Liquids and gases are sometimes grouped together as fluids because they flow very readily under the application of an external force. The concept presented enables fluids to be transported, controlled and directed into specific branches in networks while avoiding other possible branching routes, without the use of any mechanical valves. A two dimensional ($2D$) analysis of the Navier-Stokes equations with the upper wall subjected to prescribed, non-peristaltic, localized moving contractions demonstrates that a thin tube with localized moving contractions on one wall can function as a pump at the microscale. Expressions for the velocity components, pressure gradients, velocity stream function and net flow induced by the wall contractions are presented. This study might help in understanding convection of respiratory gases in insects as well as other features of the respiratory system. Novel devices for microfluidic flow transport may be invented from the results obtained in this study.

4.1 Introduction

Efficient transport of small amounts of respiratory gases within the insect trachea due to contractions observed in insect's respiratory system is an important challenging problem and its

solution can have many scientific applications. For instance, microfluidic devices and micro-electromechanical systems (MEMS) inspired by these physiological systems in insects have in recent years started to gain attention. Microfluidic devices, MEMS and their environments are typically of the order of microns [114]. Microfuidic devices are normally composed of multiple tiny branches that usually move, mix or separate fluids in drug delivery, cell manipulations, DNA chips and inkjet printheads. These applications are usually carried out via transporting of microliter amounts of fluids in a controlled manner from one site to another [116].

Two main techniques are currently used to transport fluids at the microscale. One technique uses conventional pressure-driven flow, which becomes insufficient whenever the channel geometry becomes very small. This is because as the device geometry becomes smaller and smaller, the surface forces become larger and so an excessive amount of pressure drop is required to overcome these emerging surface forces. The other technique includes valveless mechanisms such as electro-osmotic, peristaltic and impedance-mismatch. The valveless mechanisms are commercially viable and preferred because they require fewer moving parts and hence lower maintenance [117]. However, they also have some functional drawbacks. For instance, peristaltic pumping relies on wave dynamics induced by the elasticity of the tube walls [118]. With the current microfabrication techniques, it is difficult to manufacture an entire elastic microfluidic device. Many systems and processes from life sciences, such as the insect respiratory system, can be imitated in the design of such improved microdevices.

Many physiological structures and processes are uniquely found in insects, one being the air-filled respiratory system which uses both diffusion and convection for efficient distribution of respiratory gases [44–46]. The insect respiratory system is composed of a complex network of tubes, called the tracheal system, which transports gases to the tissues. The trachea generally consists of gas filled tubes that bifurcate into all parts of the body delivering oxygen and removing carbon dioxide [59, 60]. Lateral pores, called the spiracles, in the external cuticle connect the tracheal system to the outside [61]. These pores have a constricting muscle which opens and closes to regulate gas exchange. The action of these muscles affects the changes in diffusive and convective conductance. Upon entering through a spiracle, air enters a longitudinal tracheal trunk diffusing throughout a complex branching network of tracheal tubes that subdivide into smaller and smaller diameters reaching every part of the body. The large trachea (which is about $0.2mm$ in diameter) is supported by the thickening of the cuticle [59] and the entire network is suspended in the hemolymph (insect blood). At the end of the smallest tracheal tube (about 2 to 5 μm in diameter) are the tracheoles, each less than 1 μm in diameter, whose tips provide an interface for gas exchange with a living cell [59].

The insect respiratory gas exchange process involves both convective and diffusive transport modes, with convection a result of internal pressure gradients that are responsible for producing or enhancing both directed and tidal airflows [122]. Insect abdominal contractions are

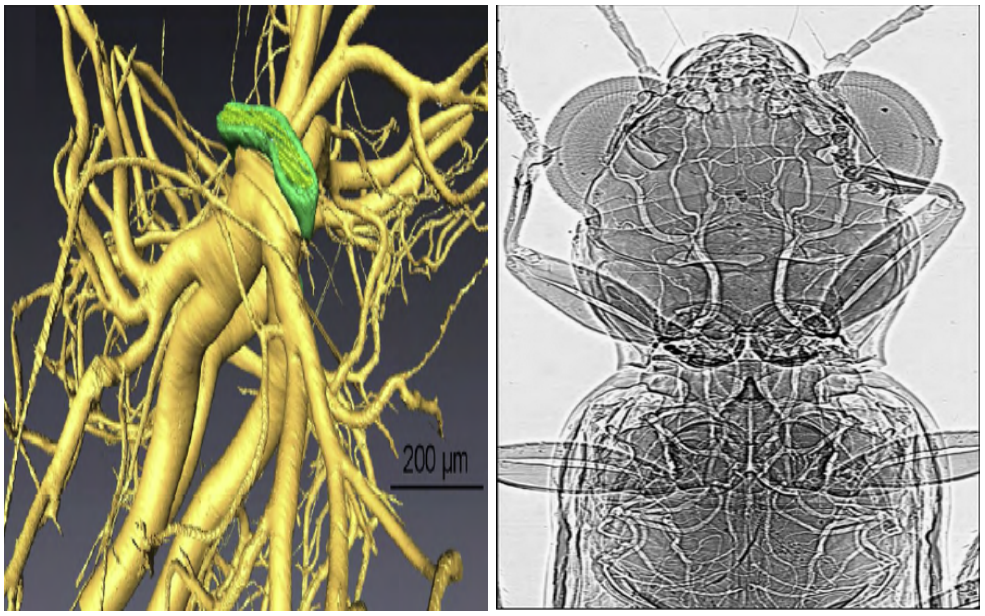

FIGURE 4.1: Tracheal system and synchrotron x-ray image of the tracheal system of a carabid beetle (Socha *et al* (2010) [61]).

hypothesized to induce changes in the insect's hemolymph pressure. Changes in hemolymph pressure are hypothesized to produce multiple rhythmic tracheal wall contractions which in turn are hypothesized to produce changes in the internal tracheal tube pressure [123]. Hence, the insect tracheal system operates efficiently via a passive mechanism whereby a single input actuates multiple contraction sites along the network. Abdominal contractions prompted new investigations into their role in gas exchange and gas transport. Recent studies in ground beetle respiratory systems have revealed that the tracheal tubing network undergoes periodic localized collapses and re-inflations [47–49]. These motions are known as rhythmic compressions and are characterized using synchrotron X-ray imaging to visualize the respiratory systems [47, 49, 61]. The flow transport induced by these wall contractions can either be peristaltic (propagative) or non-peristaltic (non-propagative). Peristaltic flows are induced by longitudinal traveling waves while non-propagative flows are induced by stationery or non-propagative contractions. This class of wall motions as described by Socha *et al* [61] has not been fully investigated and is thus the motivation for developing our model. and might explain important phenomena in many biological systems at the microscale flow regime. Figure 4.1 shows a three dimensional rendering of the trachea and synchrotron X-ray image of the tracheal system of a carabid beetle (see Socha *et al* [61] for more visuals).

Several detailed studies have been carried out in an effort to explain insect gas exchange phenomena (see [8–10, 52–54, 57]). Airflow in the respiratory system of insects under varying conditions is complex and unsteady because of the tracheal wall's rhythmic contractions [61]. Several studies have been proposed to model unsteady flow fields within a channel with moving walls, and so we use these models to understand and model the kinematics of the insect's air

transport mechanism. A two-dimensional analysis of the Navier-Stokes equations with a first order slip boundary condition is used to describe the airflow. In the field of fluid mechanics, air is treated as a fluid because all gases meet the definition of a fluid [124, 125]. Uchida and Aoki [126] presented a similarity solution for unsteady viscous flow in a semi-infinite channel with either contractions or expansions. The solution obtained in that study, where the radius of the pipe is evenly collapsed, is general and valid for a fully collapsed pipe. Secomb [127] discussed the two dimensional flow field for an incompressible viscous flow within an infinitely long tube. Skalak and Wang [128] presented an analytical solution for the unsteady squeezing of a viscous fluid from a uniformly shrinking or expanding tube. Singh *et al* [129] studied the squeezing flow problem between parallel plates using a similarity transformation which reduced the Navier-Stokes equations to a nonlinear ordinary differential equation. Earlier, Wang [130] studied the squeezing of a viscous fluid from a tube at an arbitrary squeezing rate. The solution derived was restricted to low squeezing numbers where viscous effects overcame the unsteadiness caused by wall contractions. Recently, lubrication theory based analyses that studied microscale airflow transport within a tube and channel with localized contractions was presented in Aboelkassem and Staples [133, 134], and Aboelkassem *et al* [135]. Aboelkassem and Staples [122] presented an insect-style microscale flow transport model and went on to use the Stokeslets-meshfree method to solve the Navier-Stokes equations that govern the flow motions. Efforts to manufacture microfluidic devices that mimic the insect respiratory system in the guise of simple channels with membranes attached at different locations along their length to act as pumping actuators have been carried out [133, 139].

The present study is inspired by observed rhythmic tracheal compressions of beetles, which are assumed to be a naturally efficient pumping mechanism in a complex network of microscale channels. We propose a paradigm for pumping, controlling and transporting respiratory gases in the beetle's tracheal network of channels at the microscale. We investigate the possibility of using these rhythmic contractions as a pumping mechanism. We hope results of this study can assist in designing and improving valveless microfluidic pumping devices. We present a theoretical model of fluid transport within a channel at the microscale accompanied by wall contractions. Results include that at least two contractions with a phase difference in actuation times are required to produce a simplex flow.

4.2 The model system

4.2.1 Formulation

In this section we formulate and present the mathematical model for respiratory gas flow in the beetle's trachea and tracheoles. Consider two-dimensional (2D) incompressible viscous flow

in a tiny channel/tube with finite length L and width B, with single or multiple moving wall contractions. The rendering in the thorax of a real insect is complex and three-dimensional (3D). For simplicity, a 2D geometry with two moving wall contractions is used for the theoretical analysis. The lower wall, W_1, is kept stationary and straight at all times while the upper wall, W_2, undergoes two localized contractions (see figure 4.2). The wall contractions are allowed to move independently along the lateral direction with or without a time lag θ with respect to each other to produce the pumping effect. We also assume a zero pressure drop, $\triangle p = 0$, along the channel length. The net gas flow produced by the rhythmic wall contraction-expansion protocol as well as the velocity field, pressure gradient and wall shear stress are derived. The effects of the collapse amplitudes, time lags and the allowable travel contraction distance are given. The objectives of this study include investigating the possibility of using such a channel as a pumping mechanism at the microscale. We also aim to identify the geometric and temporal parameters that maximize (minimize) both the induced net flow and shear stress.

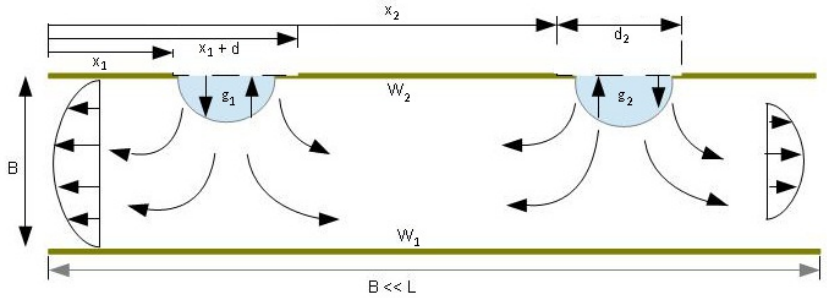

FIGURE 4.2: Problem schematic: 2D channel with a moving upper wall contraction W_2. W_1 and W_2 are the lower and upper wall profiles, respectively, g_1 and g_2 are the motion protocols assigned to the first and second contractions, respectively, L is the channel length, B is the channel width, x_i is the beginning of each collapse region, and d_i is the collapse distance.

4.2.2 Mathematical model for fluid flow

Define the width-to-length ratio (aspect ratio) as δ^{-1} which is assumed to be very large ($\delta = B/L \ll 1$). We then follow lubrication theory, which describes the flow of fluids in a geometry in which one dimension is significantly smaller than the others [137, 138], for viscous incompressible flow at low Reynolds number. The flow is assumed to be Newtonian and incompressible. The flow is isothermal with constant viscosity μ and has a velocity field $\mathbf{V} = (u, v, 0)$. The governing Navier-Stokes equations for incompressible flow, ignoring body forces, in Cartesian coordinates are given by

$$\left.\begin{aligned}
\frac{\partial \tilde{u}}{\partial \tilde{x}} + \frac{\partial \tilde{v}}{\partial \tilde{y}} &= 0 \\
\tilde{\rho}\left(\frac{\partial \tilde{u}}{\partial \tilde{t}} + \tilde{u}\frac{\partial \tilde{u}}{\partial \tilde{x}} + \tilde{v}\frac{\partial \tilde{u}}{\partial \tilde{y}}\right) &= -\frac{\partial \tilde{p}}{\partial \tilde{x}} + \tilde{\rho}\tilde{g}_x + \mu\left(\frac{\partial^2 \tilde{u}}{\partial \tilde{x}^2} + \frac{\partial^2 \tilde{u}}{\partial \tilde{y}^2}\right) \\
\tilde{\rho}\left(\frac{\partial \tilde{v}}{\partial \tilde{t}} + \tilde{u}\frac{\partial \tilde{v}}{\partial \tilde{x}} + \tilde{v}\frac{\partial \tilde{v}}{\partial \tilde{y}}\right) &= -\frac{\partial \tilde{p}}{\partial \tilde{y}} + \tilde{\rho}\tilde{g}_y + \mu\left(\frac{\partial^2 \tilde{v}}{\partial \tilde{x}^2} + \frac{\partial^2 \tilde{v}}{\partial \tilde{y}^2}\right)
\end{aligned}\right\}, \tag{4.1}$$

and the shear stress expression is given by

$$\tilde{\tau}_{xy} = \mu\left(\frac{\partial \tilde{v}}{\partial \tilde{x}} + \frac{\partial \tilde{u}}{\partial \tilde{y}}\right). \tag{4.2}$$

Define $\tilde{u}$ as the velocity component along the horizontal direction $\tilde{x}$ and $\tilde{v}$ as the component along the vertical direction, $\tilde{y}$. u_0 is an arbitrary reference velocity, $\tilde{p}$ is the static pressure, μ is the viscosity and $\tilde{Q}$ is the volumetric flow rate. R_e is the Reynolds number which is constant in x, while S_t is the Strouhal number describing the oscillating flow mechanisms. For $1 \ll S_t$, viscosity dominates fluid flow resulting in a collective oscillating movement of the fluid. $\tilde{t}$ is the time scale for the motions, and f is the contractions frequency. We then introduce the following non-dimensional parameters $x = \tilde{x}/L$, $y = \tilde{y}/B$, $W_1 = \tilde{W}_1/B$, $W_2 = \tilde{W}_2/B$, $t = \tilde{t}u_0/L$, $u = \tilde{u}/u_0$, $v = \tilde{v}/(\delta u_0)$, $p = \tilde{p}B^2/(\mu u_0 L)$, $\tau_{xy} = \tilde{\tau}_{xy}B/(\mu u_0)$, $Q = \tilde{Q}/(\mu B)$, $S_t = fL/u_0$, $R_e = \tilde{\rho}u_0 B/\mu$.

Substituting the above non-dimensional parameters into the system 4.1, the $2D$ Navier-Stokes equations reduce to

$$\left.\begin{aligned}
\frac{\partial u}{\partial x} + \frac{\partial v}{\partial y} &= 0 \\
Re\delta\left(\frac{\partial u}{\partial t} + u\frac{\partial u}{\partial x} + v\frac{\partial u}{\partial y}\right) &= -\frac{\partial p}{\partial x} + \delta^2\frac{\partial^2 u}{\partial x^2} + \frac{\partial^2 u}{\partial y^2} \\
Re\delta^3\left(\frac{\partial v}{\partial t} + u\frac{\partial v}{\partial x} + v\frac{\partial v}{\partial y}\right) &= -\frac{\partial p}{\partial y} + \delta^4\frac{\partial^2 v}{\partial x^2} + \delta^2\frac{\partial^2 v}{\partial y^2}
\end{aligned}\right\}, \tag{4.3}$$

and

$$\tau_{xy} = \delta^2\frac{\partial v}{\partial x} + \frac{\partial u}{\partial y}. \tag{4.4}$$

Since the channel geometry is restricted to a very high aspect ratio ($1 \ll \delta^{-1}$) and the flow is at the microscale, we are dealing with a low Reynolds number flow regime. Choosing the Reynolds number to be of the same order as the reciprocal of the channel aspect ratio, i.e. $R_e \in [0, \delta]$, classical lubrication theory then becomes applicable. Since $\delta \ll 1$, we discard all terms that are

of order δ^2 and higher in system 4.3. System 4.3 simplifies to

$$\frac{\partial u}{\partial x} + \frac{\partial v}{\partial y} = 0, \tag{4.5}$$

$$-\frac{\partial p}{\partial x} + \frac{\partial^2 u}{\partial y^2} = 0, \tag{4.6}$$

$$\frac{\partial p}{\partial y} = 0. \tag{4.7}$$

The non-dimensional shear stress expression in Cartesian coordinates is then given by

$$\tau_{xy} = \frac{\partial u}{\partial y}. \tag{4.8}$$

The flow of a fluid on the micro- and nanoscale is different from the macroscopic flow of the corresponding fluid [136]. To address the scaling effect at the sub-micron scale, the convectional no-slip boundary condition for viscous flow may not be applicable to the fluid flow and must be replaced by a slip boundary condition. The slip boundary condition reflects the interfacial interaction between a liquid and a solid, as well as contributions from surface roughness and intermolecular interaction. Thus, for flows through microchannels, the Navier-Stokes equations are applicable if a boundary slip condition is used. For simplicity, we use use the common approximation of fluid slip. However, later we deal with the slip boundary condition and its implication in micro- and nanofluid flow. Therefore, the boundary conditions are that the vertical velocity component v vanishes at the lower solid wall and that the streamwise velocity u is equal to the slip velocity, such that

- at $y = W_1 : u = u_{wall} + \phi\dfrac{\partial u}{\partial y}$ and $v = 0$,
- at $y = W_2 : u = u_{wall} - \phi\dfrac{\partial u}{\partial y}$ and $v = \dfrac{\partial W_2}{\partial t}$,
- at $x = 0 : p = p_0(t)$,
- at $x = 1 : p = p_L(t)$,

where $\phi = 1.15\ell$ and ℓ is the mean free path. u_{wall} is the local velocity of the solid wall and is assumed to be zero for both wall surfaces.

The static pressure is uniform along y and varies only with x ($p = p(x,t)$) since $\partial p/\partial y = 0$ (see equation 4.7). Equation 4.6 can then be integrated twice with respect to y and the related boundary conditions applied. The axial velocity component is then found to be

$$u(x,y,t) = \frac{1}{2}\frac{\partial p}{\partial x}(y^2 - (W_1 + W_2)y + W_1W_2 + \phi(W_1 - W_2)). \tag{4.9}$$

From the conservation of mass in equation 4.5 and using the related boundary conditions, the vertical velocity component v is given by

$$v(x,y,t) = (W_1 - y)\left(\frac{1}{4}\left(\frac{\partial p}{\partial x}\frac{\partial W_2}{\partial x} + W_2\frac{\partial^2 p}{\partial x^2}\right)D_1 - \frac{1}{12}\frac{\partial^2 p}{\partial x^2}D_2\right), \tag{4.10}$$

where $D_1 = W_1 - y - 2\phi$ and $D_2 = W_1^2 + W_1 y - 2y^2 - 6\phi W_1$.

The relationship between the pressure derivatives $\frac{\partial p}{\partial x}$, $\frac{\partial^2 p}{\partial x^2}$ and the rate at which W_2 moves $\left(\frac{\partial W_2}{\partial t}\right)$ is found by using equation 4.10 and the boundary condition at $y = W_2$ where $v = \frac{\partial W_2}{\partial t}$. Hence,

$$\frac{\partial W_2}{\partial t} = \frac{1}{12}(W_1 - W_2)\left(3\frac{\partial p}{\partial x}\frac{\partial W_2}{\partial x}(W_1 - W_2 - 2\phi) - \frac{\partial^2 p}{\partial x^2}((W_1 - W_2)^2 + 6\phi(W_2 - W_1))\right). \tag{4.11}$$

Integrating equation 4.11 once with respect to x, we have

$$\int \frac{\partial W_2}{\partial t}dx = \frac{1}{12}\frac{\partial p}{\partial x}(W_1 - W_2)^2(W_2 - W_1 + 6\phi) + C(t), \tag{4.12}$$

where $C(t)$ is a function of integration which depends only on t. Rearranging terms in equation 4.12, an expression for the pressure gradient is

$$\frac{\partial p}{\partial x} = \frac{1}{(W_1 - W_2)^2(W_2 - W_1 + 6\phi)}\left(C(t) + 12\int_o^x \frac{\partial W_2(s,t)}{\partial t}ds\right). \tag{4.13}$$

The expression for the static pressure can be found after integrating equation 4.13 and is given by

$$p(x,t) = p(0,t) + \int_0^x \frac{\partial p(s,t)}{\partial x}ds. \tag{4.14}$$

An expression for $C(t)$ can be found by evaluating equation 4.14 at $x = L$ where $p = p_L(t)$ and is given by

$$C(t) = \frac{p_L(t) - p_0(t) - 12\int_0^L((W_1 - W_2)^2(W_2 - W_1 + 6\phi))^{-1}\left(\int_0^x \frac{\partial W_2(s,t)}{\partial t}ds\right)dx}{\int_0^L((W_1 - W_2)^2(W_2 - W_1 + 6\phi))^{-1}dx}. \tag{4.15}$$

In equation 4.10, we need to use $\frac{\partial^2 p}{\partial x^2}$ so as to calculate the vertical velocity component explicitly. Hence, from equation 4.11, $\frac{\partial^2 p}{\partial x^2}$ is given as

$$\frac{\partial^2 p}{\partial x^2} = \frac{1}{W_2 - W_1 + 6\phi}\left[\frac{12}{(W_2 - W_1)^2}\frac{\partial W_2}{\partial t} + 3\frac{\partial p}{\partial x}\frac{\partial W_2}{\partial x}\frac{(W_1 - W_2 - 2\phi)}{(W_2 - W_1)}\right]. \tag{4.16}$$

An expression for the stream function $\psi(x, y)$ can be obtained using the fact that

$$u = \frac{\partial \psi}{\partial y} \quad \text{and} \quad v = -\frac{\partial \psi}{\partial x}.$$

Recalling u and v in equations 4.9 and 4.10, respectively, and integrating by parts, we obtain the stream function given by

$$\psi(x, y, t) = \frac{1}{12}\frac{\partial p}{\partial x}(2y^3 - 3(W_1 + W_2)y^2 + 6W_1W_2y + W_1^3 - 3W_1^2W_2 + 6\phi(W_2 - W_1)(W_1 - y)). \tag{4.17}$$

From equation 4.8 and taking the first derivative of the axial velocity component u (equation 4.9) with respect to the vertical variable y, we obtain the shear stress as

$$\tau_{xy}(x, y, t) = \frac{1}{2}\frac{\partial p}{\partial x}(2y - W_2 - W_1). \tag{4.18}$$

The flow shear stress varies linearly with the vertical direction and obtains its maximum value at the walls, and has zero values at locations where the pressure gradient is zero. The value of the shear stress at the upper wall is evaluated by setting $y = W_1$ and is given by

$$\tau_{xy}^{up}(x, t) = \frac{1}{2}\frac{\partial p}{\partial x}(W_1 - W_2). \tag{4.19}$$

At the lower wall, set $y = W_2$ and

$$\tau_{xy}^{low}(x, t) = \frac{1}{2}\frac{\partial p}{\partial x}(W_2 - W_1). \tag{4.20}$$

Thus

$$\tau_{xy}^{up} \mid_{y=W_2} = -\tau_{xy}^{low} \mid_{y=W_1} = \frac{1}{2}\frac{\partial p}{\partial x}(W_2 - W_1). \tag{4.21}$$

Lastly, the volumetric flow rate induced by the wall contractions assigned to the upper wall is derived as

$$Q(x, t) = \int_{W_1}^{W_2} u(x, y, t)dy, \tag{4.22}$$

$$= -\frac{1}{12}\frac{\partial p}{\partial x}(W_2 - W_1)^2(W_2 - W_1 + 6\phi). \tag{4.23}$$

The flow rate increases with the pressure gradient and decreases as the inner dimension $a = (W_2 - W_1)$ becomes smaller and smaller. To ascertain if the model system indeed produces unidirectional flow, equation 4.23 is integrated over a complete contraction-expansion cycle,

$t = T$. The time-averaged volumetric flow is given by

$$Q_T(x) = \frac{1}{T}\int_0^T Q(x,t)dt, \tag{4.24}$$

where $T = 1/S_t$ is the time period. The focus on the produced flow motions is during compression, when $t = T/4$, and expansion, $t = 3T/4$, times. If the model does produce unidirectional flow, then it can be adopted as a pumping mechanism.

4.3 Results and discussion

We present the geometry as well as the kinematics of the upper wall contractions as governed by the expression $W_2(x,t)$. The upper wall is allowed to undergo multiple contractions that propel forward with similar or with different amplitudes. The contractions can move with or without phase lags relative to each other. We then present the structure and evolution of the flow field produced by two specified wall contractions which undergo cyclic compression and expansion motions. The profiles of the velocity components, pressure, pressure gradients, and wall shear stress are presented and compared at $t = T/4$ (compression phase) and $t = 3T/4$ (expansion phase). Lastly, we study the time-averaged volumetric flow rate over a complete T cycle for various phase lag values.

4.3.1 Moving wall profile

We adopt a mathematical model describing the kinematics and shape of contractions from the upper wall as derived by Aboelkassem and Staples [122] and is given by

$$W_2(x,t) = \frac{1}{2} + \sum_{i=1}^{N_c} A_i f_i(x) g_i(t), \tag{4.25}$$

where

- $f_i(x) \in C^r[0,1]$ represents the spatial distribution of the upper wall shape,
- $g_i(t) \in C^r[0,T]$ represents the temporal distribution of $W_2(x,t)$ ($T = 1/S_t$ is the period of the contraction-expansion cycle),
- N_c defines the number of contractions ($N_c = 2$ in this study),
- A_i is the amplitude assigned to each contraction.

The spatial form $f_i(x)$ is assumed to imitate the geometry of the upper wall contractions as

$$f_i(x) = \tanh(\alpha(x - x_i)) - \tanh(\alpha(x - (x_i + d_i))), \tag{4.26}$$

where $\alpha = 2\pi/\delta$. x_i defines the beginning of each collapse region, and $d_i \in (0, 1 - x_i]$ marks the end of each region. Consider two contractions, i.e. $N_c = 2$ which move according to the profiles

$$g_1(t) = \begin{cases} \frac{1}{2}(1 - \cos(2\pi\beta S_t t)), & \forall \quad 0 \leq t \leq 1/\beta S_t \\ 0, & \forall \quad 1/\beta S_t < t \leq 1/S_t \end{cases} \tag{4.27}$$

$$g_2(t) = \frac{1}{2}(1 - \cos(2\pi S_t t)), \quad \forall \quad 0 \leq t \leq 1/S_t, \tag{4.28}$$

where β is a dimensionless parameter that is related to the phase lag between the first and second contractions according to the assigned motion protocol. Define T_c to be the travel collapse distance of each contraction. During the compression phase, both contractions are allowed to move together. The motion protocol is designed such that the first contraction is allowed to reach the maximum specified T_c than the second contraction (see figure 4.3(b) where the first contraction returns to its initial position first than the second). Thereafter, during the expansion phase, the first contraction returns to to its original position and continues with zero amplitude until the second contraction completes its own cycle. Once the second contraction return to zero amplitude, the two contractions start the second cycle together with the protocol shown in figures 4.3(a) and 4.3(b). Hence, there will be a time lag T_{lag} between the two collapse motions. $T_{lag} = (1 - 1/\beta)(2S_t)^{-1}$ which is equal to the phase lag $\theta = \pi(1 - 1/\beta)$. In this case, both contractions have the same time period $T = 1/S_t$ and there is a phase lag whenever $\beta \neq 1$. The adopted motion protocol ensures that after each cycle, the wall returns to its initial position and there will be no net flow due to volume deformation. Now that the kinematics of $W_2(x, t)$ are prescribed, all the flow parameters can then be calculated analytically and using simple integration techniques. The model simulations are carried out in Mathematica and MATLAB.

4.3.2 $W_2(x, t)$ induced flow field

We analyze the flow field induced by the contractions of $W_2(x, t)$ according to the motion protocol presented by equations 4.25–4.28 above. A zero pressure drop, $\triangle p(t) = 0$ is assumed along the channel length, and hence all the fluid flow will be induced as a result of the wall motions only. We consider two contractions in the upper wall, $N_c = 2$, located at $x_1 = 0.2$, $d_1 = 0.1$, $x_2 = 0.6$ and $d_2 = 0.1$. Now that W_2 is fully described, we can then evaluate the velocity components using equations 4.9-4.10, the static pressure using equation 4.14, the pressure gradient using equations 4.13-4.15, volumetric flow rate using equation 4.23, and the wall shear stress using equation 4.18. We present the flow structures at $t = T/4$ (compression) and $t = 3T/4$ (expansion) where the contractions move with different phase lags.

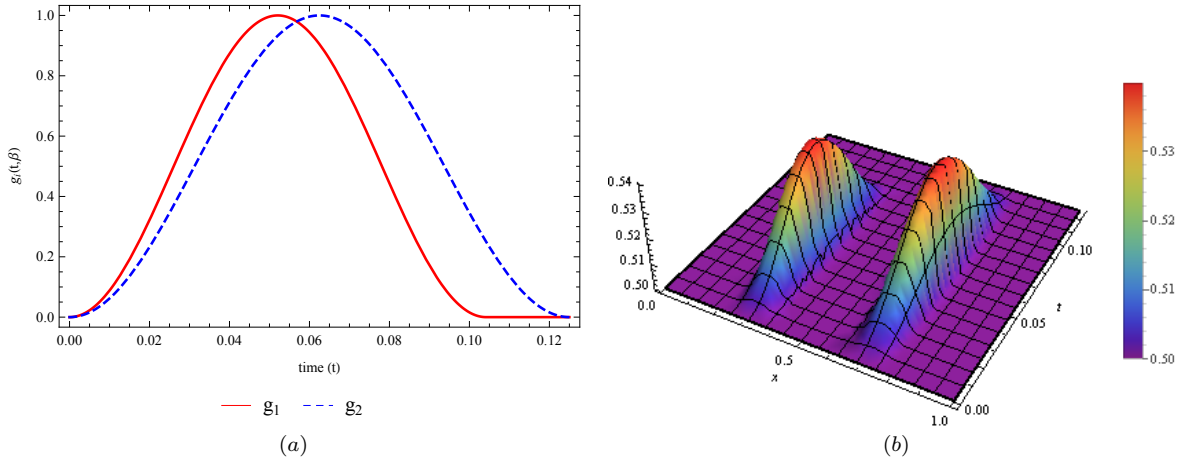

FIGURE 4.3: (a) The temporal distributions, $g_1(t)$ and $g_2(t)$, assigned to the first and second contractions, respectively, when $\beta \neq 1$. (b) 3D view of the motion protocols with a phase lag $\theta \neq 0$.

4.3.2.1 Velocity streamlines and shear stress

Typical snapshots for the induced flow motions during compression and expansions time ($t = T/4$ and $t = 3T/4$) are shown in figure 4.4. Figure 4.4 show the shear stress, streamwise and wall normal velocity components during $t = T/4$ and $t = 3T/4$ for $\theta = 30^o$. These model simulations are given to support the pumping hypothesis. The results show that as the wall contractions undergo the compression phase and start to move towards the bottom wall, the axial velocity component increases near the contraction regions and the flow is displaced, bifurcated and exits the channel from both directions at $t = T/4$. When $\theta = 30^o$, there is no stagnation zone as would be expected if the phase lag was zero. There will be flow transport within the region between the two contractions as shown by the axial velocity contour lines calculated analytically and given in figures 4.4(a-1) and 4.4(b-1) for $t = T/4$ and $t = 3T/4$, respectively. The contour lines for the vertical component are also shown in figure 4.4(a-2) and 4.4(b-2) and are characterized by two circulation zones with opposite directions (opposite functional values) underneath each contractions. Moreover, there is a nonzero pressure gradient in the region between the two contractions, which indicate that there is flow transport in this region.

Equation 4.18 shows that the flow shear stress attains its maximum value at the channel wall boundaries and has zero values at the locations where the pressure gradient is zero. Contour lines for the shear stress in figure 4.4(3) have maximum values at the contractions regions as shown. The contour lines for the shear stress during the compression time $t = T/4$ as well as during the expansion time $t = 3T/4$ are shown in figures 4.4(a-3) and 4.4(b-3), respectively. With the contractions moving with a nonzero phase lag, asymmetric flow behaviour is observed

and a unidirectional flow is produced. The results show that there appears to be a strong dependence between motion protocol and flow transport between these wall contractions.

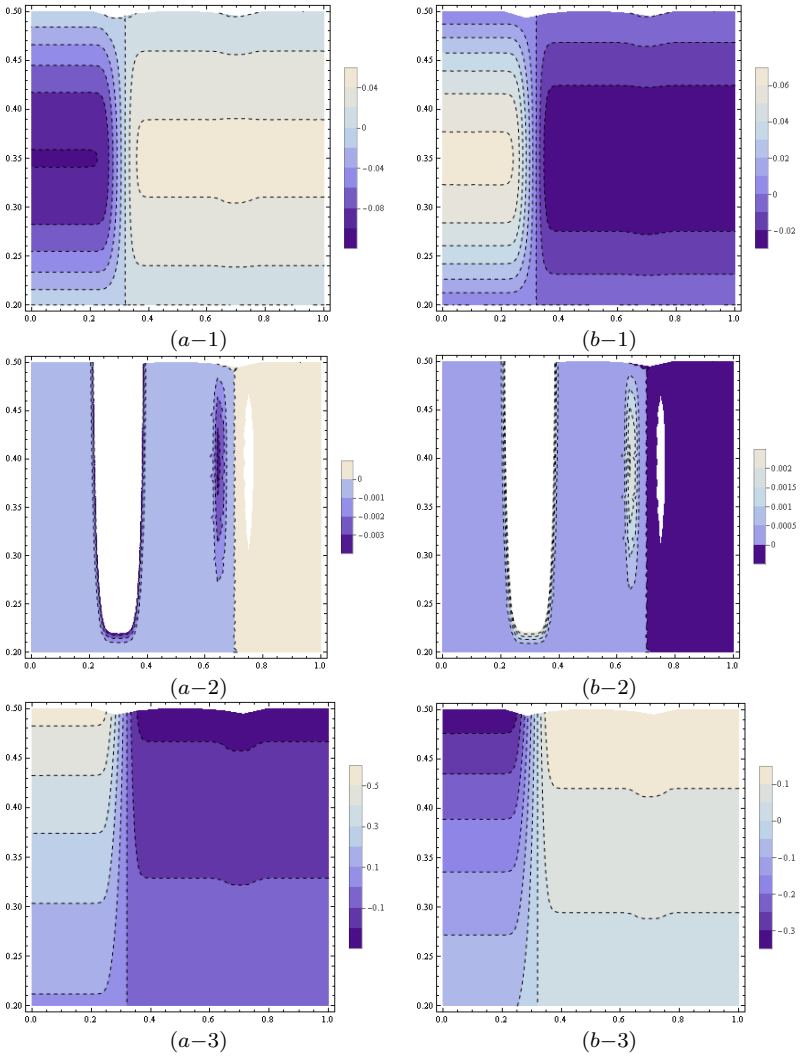

FIGURE 4.4: Velocity components and shear stress during **a** compression at $t = T/4$ and **b** expansion at $t = 3T/4$ for $\theta = 30^o$: (1) u-contours, (2) v-contours, and (3) τ_{xy}-contours.

4.3.2.2 Flow components along the axial direction

In figures 4.5 and 4.6 we plot different flow parameter distributions along the channel length to better understand the flow field produced by the motion of the wall contractions. We compare the results for different cases where the wall contractions move with a slight phase lag $\theta = 0^o$ and $\theta = 30^o$.

Figures 4.5(a) and 4.5(b) show the pressure gradient distributions along the axial direction x-axis at $\theta = 0^o$ when $t = T/4$ and $t = 3T/4$, respectively. The pressure attains a maximum constant value in the region between the two collapses while the pressure gradient in the region

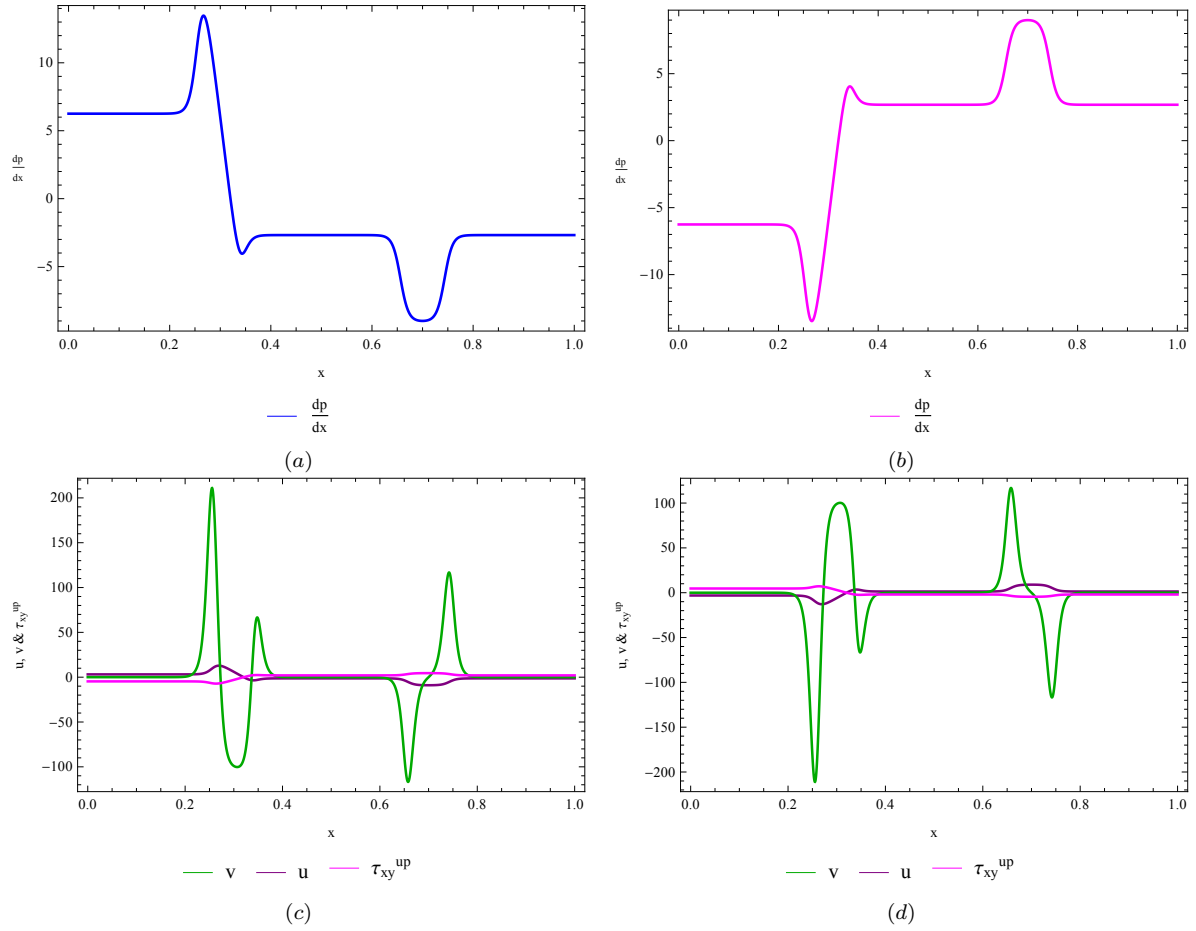

FIGURE 4.5: Distribution of the flow components along the axial direction at $y = 0$ for $\beta = 1$ (i.e $\theta = 0^o$) when $t = T/4$ and $t = 3T/4$.**(a)** The pressure gradient at $t = T/4$, **(b)** Pressure gradient at $t = 3T/4$, **(c)** wall shear stress, axial and vertical components at $t = T/4$, **(d)** wall shear stress, axial and vertical components at $t = 3T/4$.

between the contractions sites attains a constant small negative value ($dp/dx = -0.06985$ when $t = T/4$ and $dp/dx = -2.477$ when $t = 3T/4$). The pressure gradient then attains constant values with opposite signs at regions away from the contraction sites. The observed pressure gradient characteristic forces a bigger portion of the flow to bifurcate and exits from both sides. However, since $dp/dx \neq 0$ in the region between the two sides, not all the fluid exits in the lateral ends. Figure 4.5(a) shows that during the compression phase, an unfavorable pressure gradient, $dp/dx > 0$, forms on the left and neighborhood of the first contraction region, while a favorable pressure gradient, $dp/dx < 0$, forms around the second contraction region. The region between the two contractions is characterized by a favorable pressure gradient. Figure 4.5(b) shows that during the expansion phase at $t = 3T/4$, the favorable pressure gradient, $dp/dx > 0$, occurs in the neighborhood of, and to the right of the second contraction site.

In figures 4.5(c) and 4.5(d), the velocity components, both axial and vertical, and the shear stress at the upper wall, τ_{xy}^{up}, monitored at the center line $y = 0$ are shown for $t = T/4$ and

$t = 3T/4$. When $t = T/4$, the wall shear stress due to the flow motions induced by the pressure gradient variations exhibited by the wall contractions has equal and constant values away from the contraction sites. The wall shear stress is exactly zero in the region between the two contraction sites due to the existence of the inactive zone with zero net velocities. At the contraction sites, the wall shear stress attains a maximum value. This suggest that the axial velocity is zero in the region between the two contractions due to flow cancellation and attains a maximum value at the channel center line.

The axial velocity component, u, in figure 4.5(c) shows that there will be flow away from the contraction sites that exits the channel from both directions. The vertical velocity component, v, shows that as the first contraction begins, a compact region with positive vertical velocity surrounded by a negative vertical velocity region lies near that contraction region. At the second contraction region, a negative vertical velocity surrounded by a positive vertical velocity counterpart region is observed near the second contraction region. A similar scenario occurs during the expansion phase at time $t = 3T/4$ (see figure 4.5(d)) but with opposite and negative values. Comparing figures 4.5(c) and 4.5(d) highlights a key result. When $\beta = 1$, i.e. the phase lag $\theta = 0^o$, the flow behaviour when $t = T/4$ and $t = 3T/4$ is identically the same but with opposite signs.

Figure 4.6 presents plots for the pressure gradient, wall shear stress and center line velocity components along the x direction when $\beta = 1.2$. Figures 4.6(a) and 4.6(c) present results for the pressure gradient, shear stress and velocity components for $t = T/4$ while figures 4.6(b) and 4.6(d) show these for $t = 3T/4$. The key result of figure 4.6 is the fact that as the wall contractions move with a phase lag $\theta \neq 0^o$, flow is induced between the two contraction sites as well. Figures 4.6(a) and 4.6(b) present the pressure gradient distributions for both the compression and expansion times. dp/dx shows that the pressure, $p(x,t)$, is maximum at the first contraction region and minimum at the second contraction region for $t = T/4$. Further, $dp/dx \neq 0$ implies that the pressure is not constant in the region between the two contraction sites and hence, there will be flow transported from the first contraction site to the second site. For $t = 3T/4$, the scenario is reversed with a rather distinct asymmetric behaviour (see figure 4.6(b)).

Figures 4.6(c) and 4.6(d) present the response of the wall shear stress and velocity components to the pressure gradient variations. A nonzero wall shear stress ($\tau_{xy}^{up} = 5.524$ for $t = T/4$ and $\tau_{xy}^{up} = -1.788$ for $t = 3T/4$) in the region between the two contractions is observed because of the flow motion. u and v at center line, $y = 0$, are presented to show the flow movements produced by the pressure gradient variations against the shear stress behaviour.

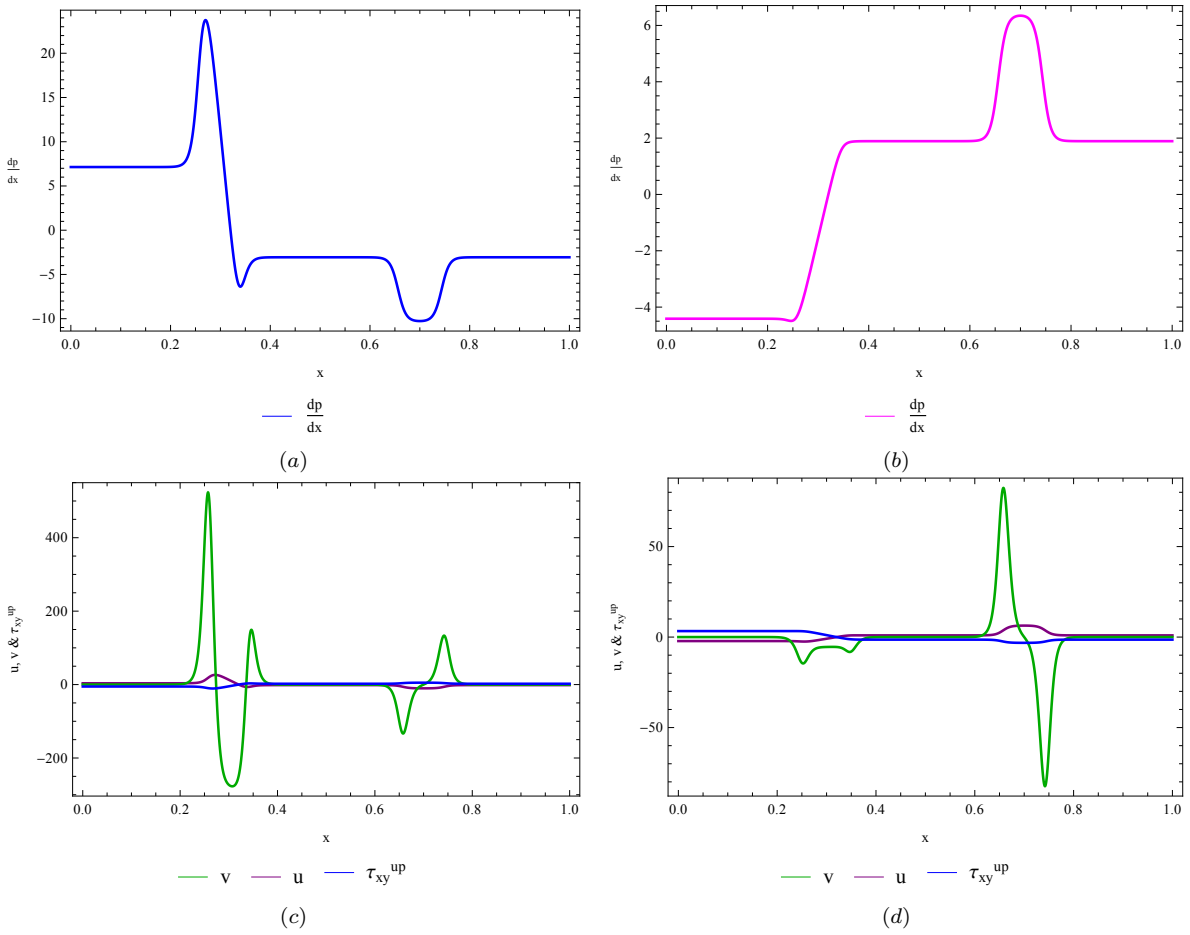

FIGURE 4.6: Distribution of the flow components along the axial direction at $y = 0$ for $\beta = 1.2$ (i.e $\theta = 30^o$) when $t = T/4$ and $t = 3T/4$.**(a)** The pressure gradient at $t = T/4$, **(b)** Pressure gradient at $t = 3T/4$, **(c)** wall shear stress, axial and vertical components at $t = T/4$, **(d)** wall shear stress, axial and vertical components at $t = 3T/4$.

4.3.2.3 Flow components along the vertical direction

In figures 4.7 and 4.8 we present the streamwise and wall normal velocity profiles along the vertical direction for both cases when $\theta = 0^o$ and $\theta = 30^o$. Profiles for the streamwise velocity component u along the vertical direction at five locations $(x = 0, 0.25, 0.5, 0.75, 1)$ are given for $\beta = 1$ at both $t = T/4$ and $t = 3T/4$ in figures 4.7(a) and 4.7(b), respectively. The velocity profiles are parabolic with the maximum value occurring away from both the upper and lower walls.

Likewise, figures 4.7(c) and 4.7(d) present the wall normal velocity component profiles along the vertical direction at the same five locations. As can be seen, for $x = 0$, 0.5, and 1, the vertical velocity is zero. The zero velocities occur because flow cancellations occur between the two contraction regions as each contraction sends flow to the right and to the left. For $\theta = 0^o$, the velocity profiles during a contraction phase at $t = T/4$, shown in figures 4.7(a) and 4.7(c), are

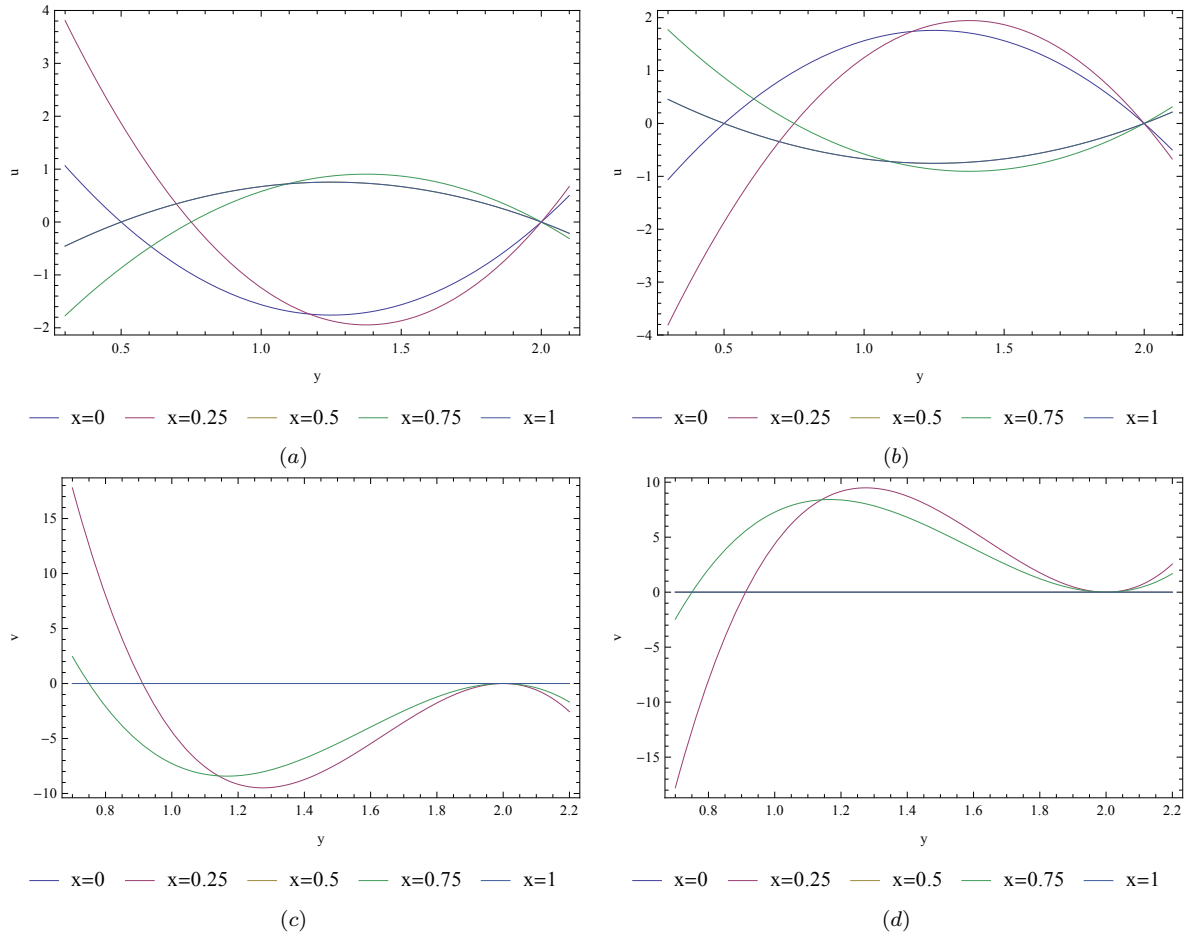

FIGURE 4.7: u and v profiles along the vertical direction at five locations ($x = 0.25, 0.5, 0.75, 1$) when $t = T/4$ and $t = 3t/4$ for $\theta = 0^o$. **(a)** Compression at $t = T/4$, **(b)** expansion at $t = 3T/4$, **(c)** compression at $t = T/4$, **(d)** expansion at $t = 3T/4$.

a mirror image of the profiles in figures 4.7(b) and 4.7(d) for the expansion phase at $t = 3T/4$. We can then conclude that when there is no phase lag between the contractions, the behaviour for the produced flow by the compressions and expansions is symmetric.

Figure 4.8 presents the profiles for velocity components u and v along the vertical direction at x =0, 0.25, 0.5, 0.75 and 1 for $\theta = 30^o$ at both $t = T/4$ and $t = 3T/4$, respectively. The profiles are characterized by the existence of flow transport between the two contractions. Also worth noting, unlike for $\theta = 0^o$, there is no symmetry in the velocity profiles in the compression time when compared with the profiles in the expansion time. Therefore, when the wall contractions move with $\theta \neq 0$, the compression and expansion process is not completely symmetric and so net flow is produced due to the wall contraction motions. This highlights that a net flow out of the tracheal system can be produced by using slight time lags between contractions motion protocols. Finding the critical phase lag θ that ensures flow transport and net flow is key to the design of the pumping devices.

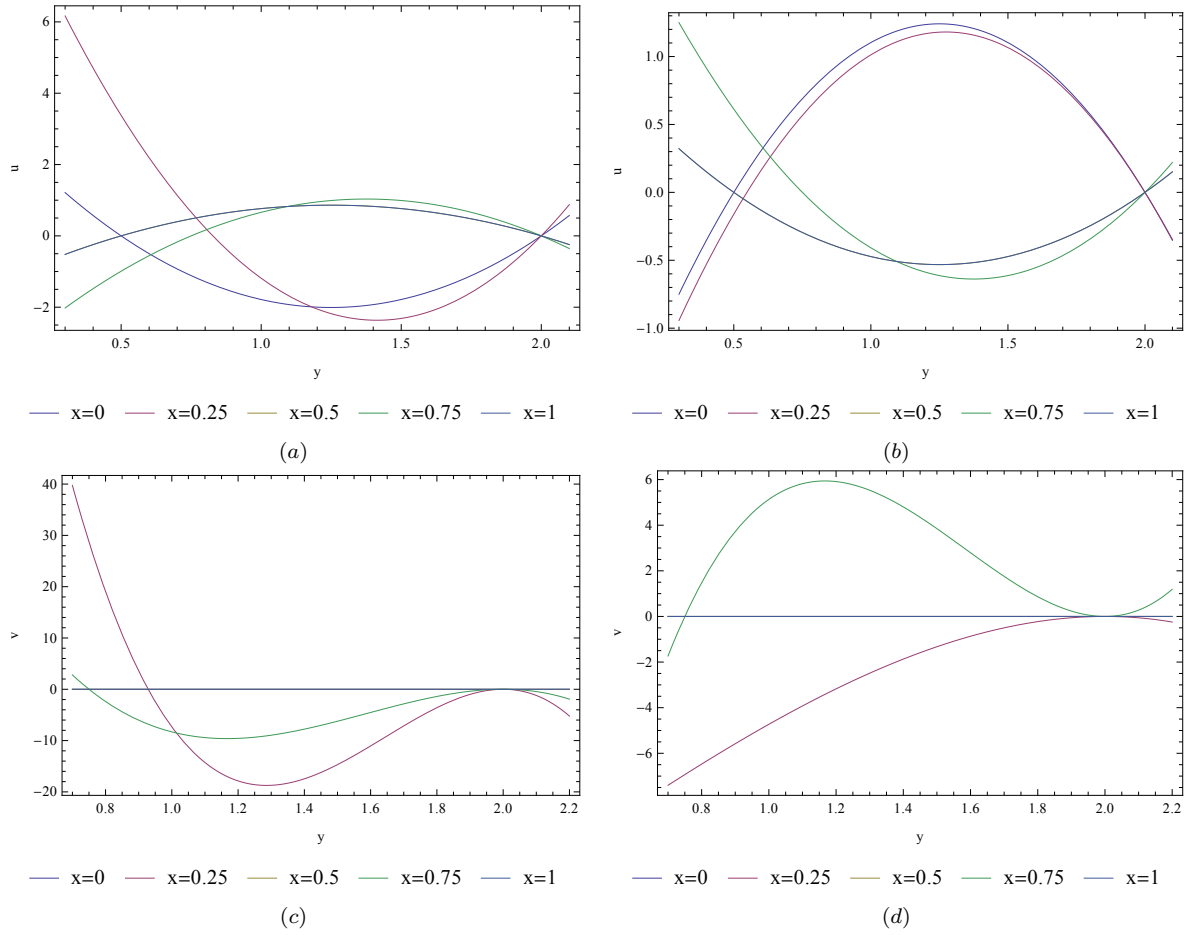

FIGURE 4.8: u and v profiles along the vertical direction at five locations ($x = 0.25, 0.5, 0.75, 1$) when $t = T/4$ and $t = 3t/4$ for $\theta = 30^o$. **(a)** Compression at $t = T/4$, **(b)** expansion at $t = 3T/4$, **(c)** compression at $t = T/4$, **(d)** expansion at $t = 3T/4$.

4.3.3 $W_2(x,t)$ induced net flow

The role of the phase lag θ and its effect on the flow transport regime within the developed mathematical system is investigated in detail. We hope to identify the requirements vital for the developed model to induce unidirectional flow without imposing any pressure drop along the channel length.

Figure 4.9(a) presents the profile of the first collapse function $g_1(t)$, which is given by equation 4.27, at different values of the phase lag parameter. Remember that the first contraction is forced to move with $g_1(t)$ while the second contraction is forced to move with $g_2(t)$ given by equation 4.28. As highlighted in the previous section, there is a lag θ between $g_2(t)$ and $g_2(t)$ that induces net flow. The phase lag θ ultimately affects the volumetric flow rate $Q(x,t)$ (see equation 4.23). We monitor the volumetric flow rate at the middle of the channel where $x = 0.5$. In figure 4.9(b), we plot $Q(0.5,t)$ over a complete cycle. It can be seen that for $\theta = 0^o$, the

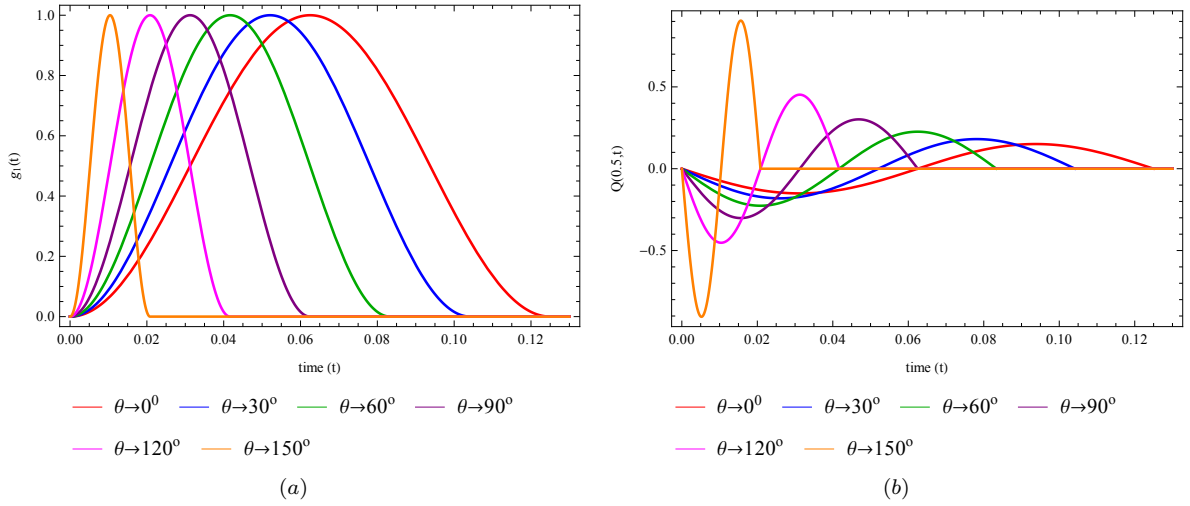

FIGURE 4.9: The motion protocol of the first contraction, $g_1(t)$, and the instantaneous volumetric flow rate, Q_T over a single cycle for different values of θ. **(a)** Different protocols of $g_1(t)$, **b** the instantaneous flow rate.

volumetric distribution is symmetric in time and so no net flow is produced. However, if $\theta \neq 0$, $Q(0.5, t)$ is not symmetric in time hence a net flow will be produced. This can be further investigated by calculating the time-averaged volumetric flow rate. By integrating the instance volumetric flow over a complete cycle, the time-average volumetric flow Q_T is obtained (see equation 4.24). In figure 4.10, we show the effect of the phase lag and travel collapse distance on the time-averaged volumetric flow rate. For all the results above, the travel collapse distance was chosen to be $T_c = 60\%$ of the original channel width. That is, the contractions are allowed to move until they reach 60% of the channel width.

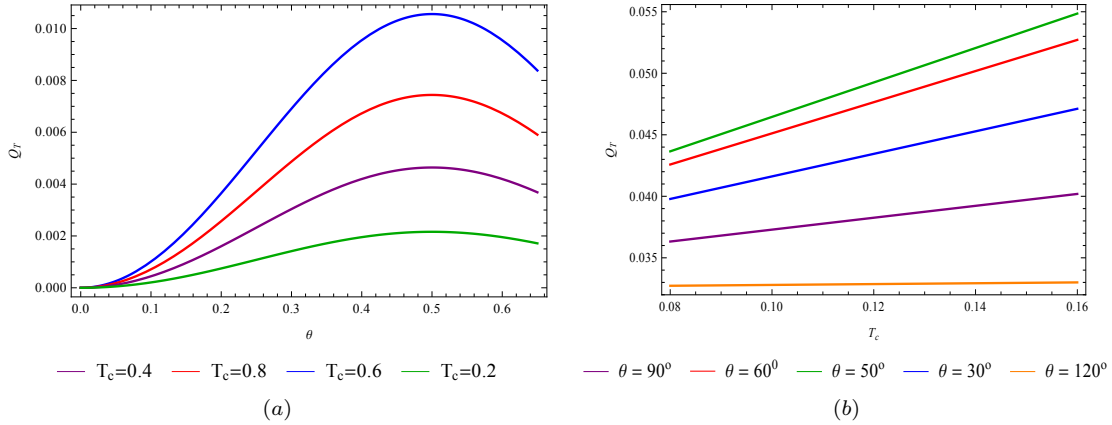

FIGURE 4.10: The time-averaged net flow rate over a single contraction cycle as a function of the phase lag, θ, and maximum travel collapse distance, T_c. **(a)** $(Q_T - \theta)$ plane, **(b)** $(Q_T - T_C$ plane

The volumetric flow rate as a function of the phase lag at different values of the allowable travel

collapse distance is given in figure 4.10(a). The plots show that, as the phase lag between the motion of the two contraction increases, the time-averaged net flow is increased until it reaches an optimum value of about $\theta_{opt} = 50^o$, afterwards the net flow starts to decay. Further, in figure 4.10(b) we plot the volumetric flow rate over a complete contraction-expansion cycle as a function of the travel collapse distance for different values of the phase lag. As the travel collapse distance increases, the net flow increases as well. However, there is maximum travel collapse distance T_c of the original channel width that maximizes the net flow.

4.4 Conclusion

We have used lubrication theory to model incompressible viscous flow in a thin tube at low Reynolds number, $R_e \in [0, \delta]$, where $\delta = B/L$. Analytical expressions for the flow dynamics including the velocity field, static pressure, pressure gradient and wall shear stress in the thin channel are given. The mathematical model presented is very simple and can be extended to include contractions from both the upper and lower walls. For net flow to be induced, there should be a phase lag between the two contractions. We presented results of the effects of the contraction amplitudes and phase lag on the instantaneous and time-averaged volumetric flow.

The obtained results from the model suggest that a thin tube such as the trachea with localized contractions on one wall can function as a pump at the microscale. The results suggest that using a non-elastic channel, at least two contractions on one wall moving with a slight phase lag with respect to each other are required to induce unidirectional flow. There also exists an optimum phase lag value with which net flow is maximized. This study may produce guidelines for the development of novel microfluidic pumping devices applicable in other biological settings.

Chapter 5

Optimization of the derived tracheal pumping model

The optimal design parameters for the derived pumping model for efficient induced net flow motions, described in Chapter 4, are derived. The constrained optimization technique based on the global minima approach to determine the optimum spatial and temporal parameters is employed. The following question needs to be answered, under what geometric and temporal configurations is our model optimal? We aim to optimize the net flow along the trachea for efficient net flow production.

5.1 Constrained optimization

The main goal of constrained optimization is to determine optimal solutions to the presented problem where the cost function is minimized or maximized with respect to certain constraints [99]. Typically, in a constrained optimization problem formulation, one is required to minimize or maximize a real valued function $f(\mathbf{x})$ of N design variables. $f(\mathbf{x})$ is the objective function and a vector $\mathbf{x}^*$ such that $f(\mathbf{x}^*)$ is the minimum or maximum value needs to be found. We say a minimum value $f(\mathbf{x}^*)$ is attained at $\mathbf{x}^*$ if a local minimizer $\mathbf{x}^*$ exists.

Thus, the problem is to minimize $f(\mathbf{x})$ over a set $U \subset R^N$. A local minimizer is a vector $\mathbf{x}^* \subset U$ such that

$$\min_{x \in U} f(\mathbf{x}) \qquad \text{which can be expressed as,} \tag{5.1}$$

$$f(\mathbf{x}^*) < f(\mathbf{x}) \quad \forall \quad \mathbf{x} \in U \quad \text{near} \quad \mathbf{x}^*. \tag{5.2}$$

A global minimizer is a vector $\mathbf{x}^* \subset U$ such that

$$f(\mathbf{x}^*) < f(\mathbf{x}) \quad \forall \quad \mathbf{x} \in U. \tag{5.3}$$

The induced time averaged net flow rate and wall shear stress in the tracheal channels with two moving wall contractions are chosen to be our objective functions. These two flow characteristics need to be optimized according to a set of geometrical and temporal constrained parameters. The geometrical constraints outline the wall contractions profile while the temporal constraints govern how the wall contractions propagate with respect to each other.

5.2 Optimization of the tracheal pumping model

The tracheal pumping model derived in section 4.2 shows that at least two contractions are required to produce unidirectional flow in the trachea. The contractions act as a pumping device.

The problem schematic is depicted in figure 4.2. Consider the trachea with two contraction sites marked by distances x_1 and x_2 with each collapse site of length d_1 and d_2 , respectively. $x_2 = x_1 + d_1 + l$ where l marks the spacing between the two contractions.

Now, recall the tracheal tube wall profile

$$W_2(x,t) = \frac{1}{2} + A_1 f_1(x, x_1, d_1) g_1(\beta, S_t, t) + A_2 f_2(x, x_2, d_2) g_2(S_t, t), \tag{5.4}$$

where f_1, f_2, g_1 and g_2 are

$$f_1(x) = \tanh(\alpha(x - x_1)) - \tanh(\alpha(x - (x_1 + d_1))) \tag{5.5}$$

$$f_2(x) = \tanh(\alpha(x - x_2)) - \tanh(\alpha(x - (x_2 + d_2))) \tag{5.6}$$

$$g_1(t) = \begin{cases} \frac{1}{2}(1 - \cos(2\pi\beta S_t t)), & \forall \quad 0 \le t \le 1/\beta S_t \\ 0, & \forall \quad 1/\beta S_t < t \le 1/S_t \end{cases} \tag{5.7}$$

$$g_2(t) = \frac{1}{2}(1 - \cos(2\pi S_t t)), \quad \forall \quad 0 \le t \le 1/S_t \tag{5.8}$$

and β is related to the time lag between the two contractions.

The objective functions for the induced net flow and wall shear stress at the lower wall, as derived in section 4.2, are

$$\tau_{xy}(x,t) = \frac{1}{2}\frac{\partial p}{\partial x}(W_2 - W_1) \tag{5.9}$$

$$Q(x,t) = -\frac{1}{12}\frac{\partial p}{\partial x}(W_2 - W_1)^2(W_2 - W_1 + 6\phi) \tag{5.10}$$

where

$$\frac{\partial p}{\partial x} = \frac{1}{(W_1 - W_2)^2 (W_2 - W_1 + 6\phi)} \left(C(t) + 12 \int_o^x \frac{\partial W_2(s,t)}{\partial t} ds \right) \quad \text{and} \tag{5.11}$$

$$C(t) = \frac{p_L(t) - p_0(t) - 12 \int_0^L ((W_1 - W_2)^2 (W_2 - W_1 + 6\phi))^{-1} \left(\int_0^x \frac{\partial W_2(s,t)}{\partial t} ds \right) dx}{\int_0^L ((W_1 - W_2)^2 (W_2 - W_1 + 6\phi))^{-1} dx}. \tag{5.12}$$

The aim is to determine optimal design parameters f_1, f_2, g_1, g_2 and θ that maximize the induced net flow $Q(x,t)$ and minimize the wall shear stress $\tau_{xy}(x,t)$.

5.2.1 Effect of the spatial and temporal variable

The net flow behaviour as a function of each spatial and temporal variable is investigated, i.e., the percentage travel collapse distance T_c (defined as a percentage of the channel width), the time (phase) lag between the two contractions θ, the start position of the first contraction x_1, length of the first contraction d_1, end of the second contraction $x_3 = x_2 + d_2$ and the distance between the two contractions $l = x_2 - x_1 - d_1$. The objective is to show the effect of each of these variables on net mass flow distribution produced by the respiratory gases tracking model presented in section 4.2.

The effects of the phase lag and travel collapse distance on the time-averaged net flow are shown in figure 5.1. Figure 5.1(a) is a plot of the time-averaged net flow Q_T as a function of the phase lag θ at different T_c values, where T_c is the travel collapse distance. The plot shows that as the phase lag θ between the two contractions increases for a given T_c value, the contraction induced net flow increases to a maximum value at about $\beta \simeq 1.18034$, where β is related to the time lag between the two contractions as previously defined in Chapter 4. The induced net flow then decreases back with zero net flow observed for $\theta \simeq 180^0$. Figure 5.1(b) shows the plot of time-averaged net flow as a function of the travel collapse distance T_c for given values of the phase lag θ. As the travel collapse distance increases, the net flow increases. However, the net flow increases until a certain maximum value for $T_c \in (0.4, 0.8)$ is attained (see figure 5.1(a) where the net flow for $T_c = 0.6$ is greater than the net flow for $T_c = 0.4$ and $T_c = 0.8$).

Parametric analysis is implemented to study the effect of the start of the first contraction x_1 on net flow. Figure 5.2 shows the distribution of the net flow as a function of x_1 for different values of the phase lag θ. The time averaged net flow increases as the phase lag increases until it reaches a maximum for $\theta \in (30^o, 60^o)$. For all cases of the phase lag θ, the time averaged net flow attains maximum values at $x_1 = 0.1$. This shows that as the start of the first collapse increases, the net flow induced by the flexible tracheal walls decreases linearly as depicted in figure 5.2.

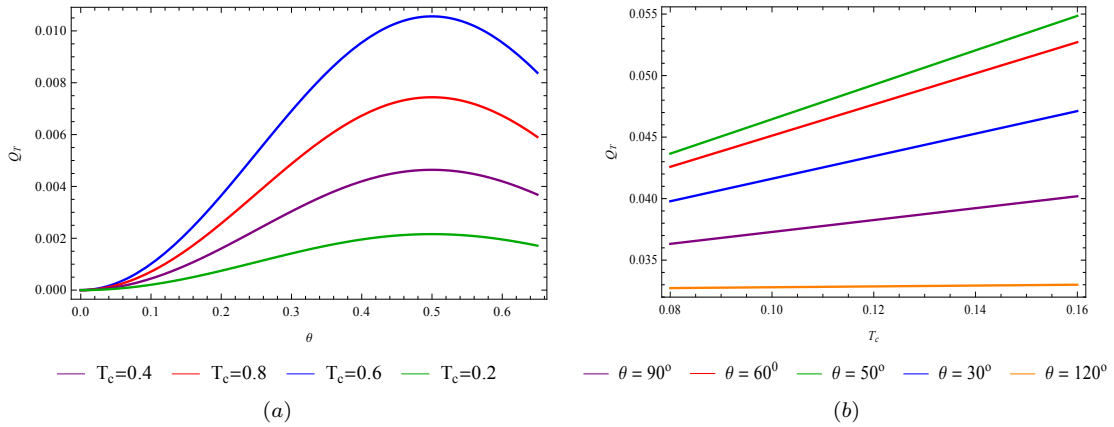

FIGURE 5.1: Time-averaged net flow rate over a single contraction cycle as a function of the phase lag, θ, and maximum travel collapse distance, T_c. **(a)** $(Q_T - \theta)$ plane, **(b)** $(Q_T - T_C$ plane

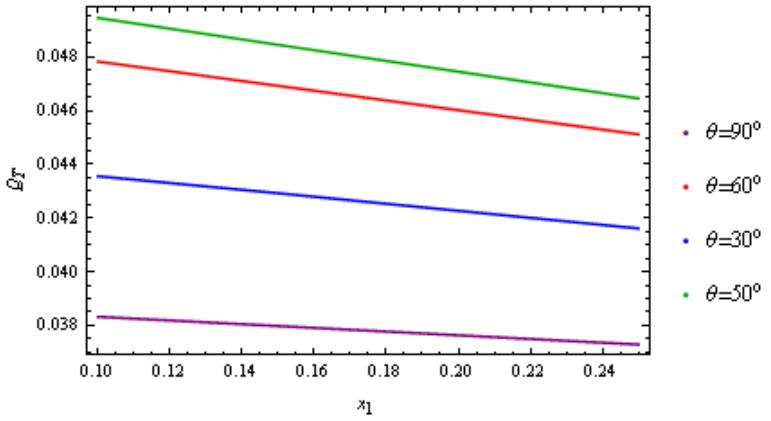

FIGURE 5.2: Effect of the beginning of the first contraction distance x_1 on the time averaged net flow for different values of the phase lag θ.

In figure 5.3, parametric analysis is implemented to study the effect of the collapse distance of the first contraction, d_1, on the time averaged net flow at different values of the time (phase) lag θ. The time averaged net flow increases as the phase lag increases until it reaches maximum and then begins to drop. Unlike x_1's case, as the width of the first contraction increases, the net flow induced by the tracheal wall motions increases nonlinearly as shown in figure 5.3. The time averaged net flow is enhanced whenever a wider collapse distance d_1 is used.

Figure 5.4 shows the effect of extending the second contraction site by using a larger collapse distance. In this case, while varying x_3, the configurations of the first collapse are kept fixed. Figure 5.4 shows that using larger collapse regions in the second contraction will increase the time averaged net flow. For the given plot, maximum net flow occurs when the second collapse distance $x_3 = 0.4$ is used and $\theta = 60^o$. Increasing the phase lag between the two contractions will increase net flow for each given second contraction collapse distance x_3.

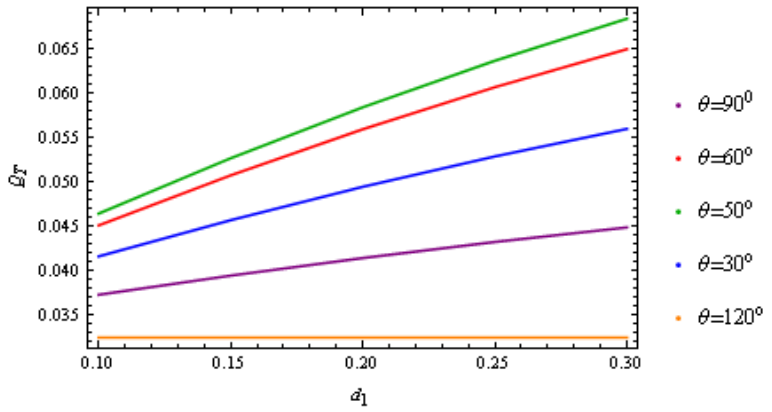

FIGURE 5.3: Effect of the collapse distance of the first contraction d_1 on the time averaged net flow for different values of the phase lag θ.

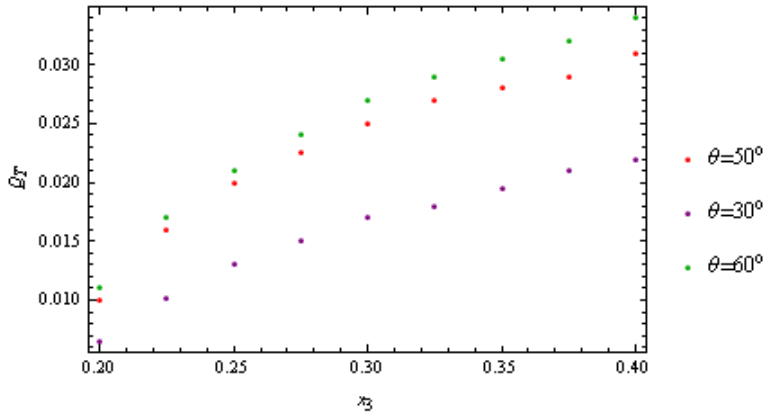

FIGURE 5.4: Effect of the second contraction distance $x_3 = x_2 + d_2$ on the time averaged net flow for different values of the phase lag θ.

Finally, the effect of the spacing distance l between the two contractions on the time averaged net flow is shown in figure 5.5. For the test case, the two contraction configurations are kept identical and l is varied. Figure 5.5 shows that for all θ values, the maximum time averaged net flow is obtained when $l = 0.1$. This means that higher net flow takes place when the two identical contractions are set close to each. For this case, maximum net flow occurs at a phase lag of about $\theta \in [60^o, 180^o)$. In summary, using two identical contractions located very close to each other results in increased net flow.

Based on the parametric analysis in figures 5.1-5.5, it can be concluded that the time averaged net flow induced by the observed insect tracheal contractions depends strongly on the geometrical and temporal parameters that shape and govern the movement of the two contractions. For contractions very close to each other, wider collapse regions coupled with larger collapse ratios and moving with different phase lag will result in increased net flow.

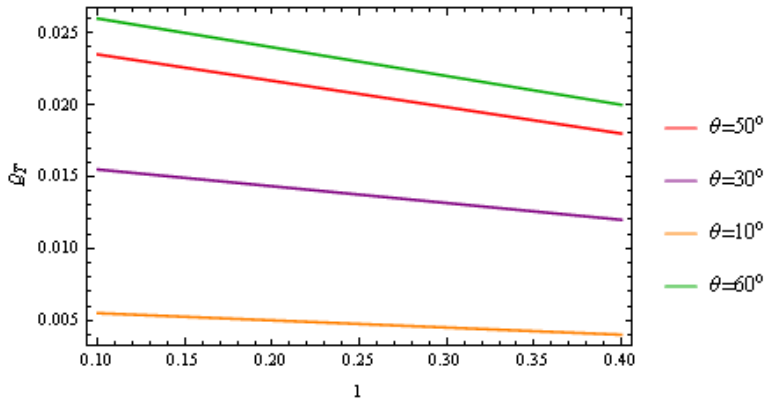

FIGURE 5.5: Effect of the spacing distance l between the two contractions on the time averaged net flow for different values of the phase lag θ.

5.2.2 Optimization functions

In the previous section, the relation of each parameter variation to net flow was analyzed. Even though each parameter variation resulted in increased net flow values, determining optimum configurations that produce ultimate net flow would be ideal. This section describes an attempt to determine these ultimate configurations.

Constrained optimization is used as a complementary analysis of the results obtained in the previous section. The aim is to determine improved optimal pumping conditions for the derived model tracking respiratory gas movement within the insect tracheal system. The aim is to solve

$$\text{minimize:} \quad F_1(\bar{x}) = -Q_T = -\frac{1}{T}\int_0^T Q(x,t)dt \tag{5.13}$$

$$\text{minimize:} \quad F_2(\bar{x}) = \tau_T = \frac{1}{T}\int_0^1\int_0^T \tau(x,t)dtdx \tag{5.14}$$

subject to

$$\bar{x} = \begin{cases} 0^o \leq \theta \leq 180^o \\ 0.1 \leq d_1 \leq 0.3 \\ 0.1 \leq d_2 \leq 0.3 \\ 0.2 \leq l \leq 0.4 \\ x_1 = L/2 - l/2 - d_1 \\ x_2 = L/2 + l/2 \end{cases} \tag{5.15}$$

with the parameters x_1, x_2, l, d_1, d_2 and θ as previously defined. The aim is to determine the optimum vector $\bar{x}^* = [d_1, l, d_2, \theta]$ that optimizes the induced time averaged net flow. The baseline configuration has $x_1 = 0.2$, $l = 0.25$, $d_1 = 0.1$ and $d_2 = 0.1$. Mathematica optimization toolbox is used to perform the calculations. Global minima constrained optimization techniques

are used to determine the optimal parameters. Two cases are investigated namely symmetric and non-symmetric configurations and are compared with the baseline configurations, i.e.,

- Symmetric configuration: both contractions have the same geometries and the tracheal channel is symmetric about $x = 0.5$.
- Non-symmetric configuration: the contractions are not required to be identical.

The results of the time averaged net flow implemented as an optimization function are shown in figure 5.6. Table 5.1, shows the minimizer vector for both symmetric and non-symmetric configurations as compared with the baseline configuration. The net flow produced by the non-symmetric configuration is slightly higher than the baseline and symmetric cases. Interestingly, the optimal values for all the cases occur at a very similar phase lag value (see Table 5.1). Thus, it can be concluded that the non-symmetric configuration is the optimum case efficiently producing higher net flow when compared to the baseline and symmetric configurations.

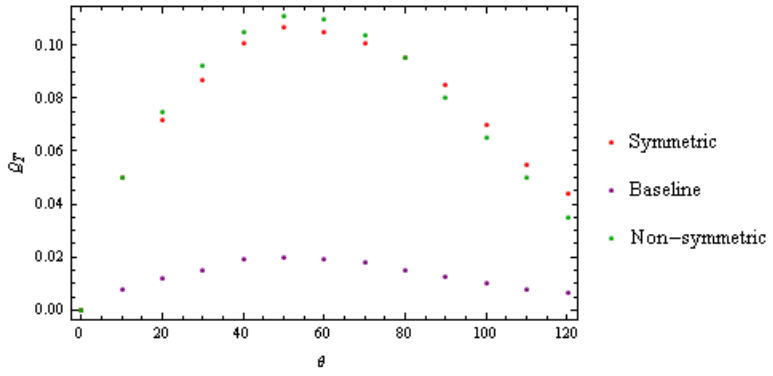

FIGURE 5.6: Tracheal channel net flow optimization function. The time averaged net flow distribution as a function of the phase lag θ.

TABLE 5.1: Time averaged net flow optimization configurations for the tracheal channel.

Contraction configurations	θ	d_1	d_2	l	Q_T
Baseline	48.922	0.100	0.100	0.250	0.01104
Optimum symmetric	49.290	0.300	0.300	0.150	0.10733
Optimum non-symmetric	48.165	0.402	0.280	0.150	0.11028

Table 5.2 and Figure 5.7 present results for the tracheal wall shear stress when implemented as an optimization function (see equation 5.14). The optimal values of the shear stress for the baseline, symmetric and non-symmetric configurations are given in Table 5.2. The optimal values for all the configurations occur at almost the same phase lag value. The symmetric and non-symmetric optimal values are almost identical but significantly higher than the adopted baseline case.

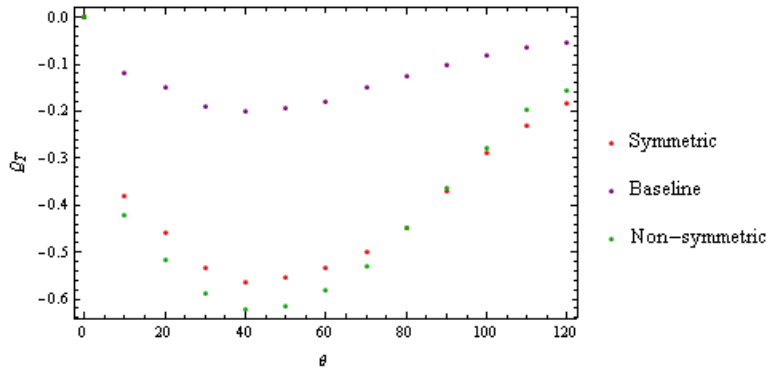

FIGURE 5.7: Tracheal wall shear stress optimization function. Tracheal wall shear stress distribution as a function of the phase lag θ.

TABLE 5.2: Tracheal wall shear stress optimization configurations for the tracheal channel.

Contraction configurations	θ	d_1	d_2	l	Q_T
Baseline	40.38	0.100	0.100	0.250	-0.0198
Optimum symmetric	41.97	0.300	0.300	0.150	-0.5709
Optimum non-symmetric	42.34	0.402	0.280	0.150	-0.6186

5.3 Concluding remarks

In this chapter a parametric study to investigate the effect of both geometrical and temporal parameters on efficient pumping was performed. Constrained nonlinear optimization analysis was presented for the baseline, symmetric and non-symmetric geometrical configurations. Optimal geometric and spatial variables for efficient pumping were presented. For both net flow and wall shear stress optimization, the non-symmetric configuration was the optimum scenario and works more efficiently when compared with both symmetric and baseline configurations.

Chapter 6

Numerical validation using the Differential Transform Method

Systems of nonlinear partial differential equations ($PDEs$) arise in scientific fields such fluid dynamics, mathematical biology, solid state physics and chemical kinetics. A variety of numerical as well as exact approximate methods are available for the solution of systems of nonlinear $PDEs$. Most of these methods are trial-and-error in nature hence computationally intensive, and need complicated symbolic computations. In this chapter, the Differential Transform Method (DTM), a numerical method based on Taylor series expansion, is used to validate the derived models for movement of respiratory gases in the insect trachea discussed in Chapter 3. The numerical validation process covers the model that considers the trachea as a single flexible compartment with gas exchange.

6.1 Basic idea of the one-dimensional and two-dimensional DTM

The concept of differential transform method was first introduced by Zhou [105] in solving linear and nonlinear initial value problems in electrical circuit analysis. DTM is an iterative procedure that is described by transformed equations of original functions for solution of ordinary differential equations. It is in fact a numerical method based on a Taylor expansion. DTM constructs an analytical solution in the form of a polynomial [102]. Unlike the high order Taylor series method which requires many symbolic computations, the DTM is an iterative procedure to obtain Taylor series solutions. Advantages of this DTM include less computation time when applied to nonlinear systems, fewer symbolic computations and that it gives an analytic solution in the form of a polynomial. DTM is a universal method in that it is able to solve various kinds of functional equations. It has been applied to fractional differential equations [110], to the KdV and $mKdV$ equations [111], to the quadratic Riccati equation [109], to the linear and

nonlinear Klein-Gordon equation [107], to differential-algebraic equations [112] and to two point boundary value problems [113]. Determining exact solutions for nonlinear systems is difficult and so DTM provides an alternative to approximating such solutions.

6.1.1 One-dimensional DTM:

Here, the system of ordinary differential equations is considered by the differential transformation technique. The basic definitions of the differential transform may be found in Chen and Liu [100]. More definitions are also given by Chen and Ho [108]. The definitions are introduced as follows:

Definition The differential transform of the derivative of a function is defined as

$$U(k) = \frac{1}{k!}\left[\frac{d^k u(x)}{dx^k}\right]_{x=x_0}, \tag{6.1}$$

where $u(x)$ is the original function and $U(k)$ is the transformed function. The inverse differential transform is defined as

$$u(x) = \sum_{k=0}^{\infty} U(k)(x - x_0)^k, \tag{6.2}$$

in a real application, and when x_0 is taken to be zero, then the function $u(x)$ is expressed by a finite series and equation 6.2can be written as

$$u(x) = \sum_{k=0}^{\infty} U(k)x^k. \tag{6.3}$$

The fundamental mathematical operations performed by one-dimensional differential transform method are as follows:

Theorem 6.1.2. *If the original function,* $u(x) = f(x) \pm g(x)$*, then* $U(k) = G(k) \pm H(k)$.

Theorem 6.1.3. *If* $u(x) = cf(x)$*, then* $U(k) = cG(k)$.

Theorem 6.1.4. *If* $u(x) = \dfrac{df(x)}{dx}$*, then* $U(k) = (k+1)G(k+1)$.

Theorem 6.1.5. *If* $u(x) = \dfrac{d^n f(x)}{dx^n}$*, then* $U(k) = (k+1)(k+2)\dots(k+n)G(k+n)$.

Theorem 6.1.6. *If* $u(x) = f(x)g(x)$*, then* $U(k) = \sum_{r=0}^{k} F(r)G(k-r)$.

Theorem 6.1.7. *If* $u(x) = f(x)g(x)h(x)$*, then* $U(k) = \sum_{s=0}^{k}\sum_{r=0}^{s} F(r)G(s-r)H(k-s)$.

Theorem 6.1.8. *If* $u(x) = x^n$*, then* $U(k) = \delta(k-n)$.

The Kronecker delta function $\delta(k-n)$ is given by

$$\delta(k-n) = \begin{cases} 1, & \text{if} \quad k = n, \\ 0, & \text{if} \quad k \neq n. \end{cases}$$

Theorem 6.1.9. *If* $u(x) = exp(ax)$, *then* $U(k) = \dfrac{a^k}{k!}$.

Theorem 6.1.10. *If* $u(x) = (1+x)^n$, *then* $U(k) = \dfrac{s(s-1)\dots(s-k+1)}{k!}$.

Theorem 6.1.11. *If* $u(x) = sin(\omega x + c)$, *then* $U(k) = \dfrac{\omega^k}{k!} sin\left(\dfrac{\pi k}{2!} + c\right)$.

Theorem 6.1.12. *If* $u(x) = cos(\omega x + c)$, *then* $U(k) = \dfrac{\omega^k}{k!} cos\left(\dfrac{\pi k}{2!} + c\right)$.

6.1.13 Two-dimensional DTM:

The basic definitions of the $2D$ DTM may be found in Jafari *et al.* [103], and Kanth and Aruna [106, 107]. Based on the $1D$ DTM, the basic definitions are defined below. Consider a function of two variables $w(x,y)$, represented by one series whose centre at is located at (x_0, y_0). The differential transform of the function $w(x,y)$ is of the form

$$W(k,h) = \frac{1}{k!h!}\left[\frac{\partial^{k+h} w(x,y)}{\partial x^k \partial y^h}\right]_{(x_0,y_0)}, \tag{6.4}$$

where $w(x,y)$ is the original function and $W(k,h)$ is the transformed function. The inverse differential transform is defined as

$$w(x,y) = \sum_{k=0}^{\infty}\sum_{h=0}^{\infty} W(k,h)(x-x_0)^k (y-y_0)^h. \tag{6.5}$$

In real applications, and when (x_0, y_0) is taken as $(0,0)$, the original function $w(x,y)$ is expressed by a finite series given by

$$w(x,y) = \sum_{k=0}^{\infty}\sum_{h=0}^{\infty} \frac{1}{k!h!}\left[\frac{\partial^{k+h} w(x,y)}{\partial x^k \partial y^h}\right]_{(0,0)} x^k y^h. \tag{6.6}$$

Theorem 6.1.14. *If the original function,* $w(x,y) = u(x,y) \pm v(x,y)$, *then* $W(k,h) = U(k,h) \pm V(k,h)$.

Theorem 6.1.15. *If* $w(x,y) = cu(x,y))$, *then* $W(k,h) = cU(k,h)$.

Theorem 6.1.16. *If* $w(x,y) = \dfrac{\partial u(x,y)}{\partial x}$, *then* $W(k,h) = (k+1)U(k+1,h)$.

Theorem 6.1.17. *If* $w(x,y) = \dfrac{\partial u(x,y)}{\partial y}$, *then* $W(k,h) = (h+1)U(k,h+1)$.

Theorem 6.1.18. *If* $w(x,y) = \dfrac{\partial^{r+s} u(x,y)}{\partial x^r \partial y^s}$, *then* $W(k,h) = (k+1)(k+2)\dots(k+r)(h+1)(h+2)\dots(h+s)U(k+r,h+s)$.

Theorem 6.1.19. *If* $w(x,y) = x^m y^n$, *then* $W(k,h) = \delta(k-m,h-n) = \delta(k-m)\delta(h-n)$.

where

$$\delta(k-m) = \begin{cases} 1, & \text{if} \quad k=m, \quad h=n \\ 0, & \text{otherwise.} \end{cases}$$

Theorem 6.1.20. *If* $w(x,y) = u(x,u)v(x,y)$, *then* $W(k,h) = \sum_{r=0}^{k}\sum_{s=0}^{h} U(r,h-s)V(k-r,s)$.

Theorem 6.1.21. *If* $w(x,y) = \dfrac{\partial u(x,u)}{\partial x}\dfrac{\partial v(x,y)}{\partial x}$, *then* $W(k,h) = \sum_{r=0}^{k}\sum_{s=0}^{h}(r+1)(k-r+1)U(r+1,h-s)V(k-r+1,s)$.

Theorem 6.1.22. *If* $w(x,y) = x^m sin(\omega y + c)$, *then* $W(k,h) = \dfrac{\omega^k}{h!}\delta(k-m)sin\left(\dfrac{\pi h}{2!} + c\right)$.

Theorem 6.1.23. *If* $w(x,y) = x^m cos(\omega y + c)$, *then* $W(k,h) = \dfrac{\omega^k}{h!}\delta(k-m)cos\left(\dfrac{\pi h}{2!} + c\right)$.

Theorem 6.1.24. *If* $w(x,y) = x^m exp(ay)$, *then* $W(k,h) = \dfrac{a^k}{h!}\delta(k-m)$.

6.2 Numerical validation of the flexible trachea models

Using the DTM method, this section numerically validates the flexible trachea models presented previously in Chapter 3, section 3.2. Initially, I will recall and list briefly the flexible trachea model formulation and analysis, then I will proceed with the numerical validation details. Lastly, detailed comparisons between both theoretical and DTM will be given.

6.2.1 Formulation and theoretical analysis

Recall the models for movement of respiratory gases in the insect trachea, presented in Chapter 3. The first model considers the tracheal system as a single rigid compartment, the second model considers the trachea as a flexible compartment, while the third model considers the trachea as a single flexible compartment with gas exchange. The last two models showed that changes in body pressure caused the trachea pressure to change, resulting in airflow in and out of the trachea. The total volume of the trachea is given by V_T while P_T is the total pressure averaged

over all the trachea in the different regions of the tracheal system. Abdominal contractions have been observed in some insects at rest and we denote the body pressure as P_B. The pressure exerted by spiracle muscles and that by ambient air during the open spiracle phase is given by P_s. The overall resistance to overall airflow in the conducting airways is denoted as R_s while elastance of the trachea is given as E_T. Figures 3.2 and 3.3 describe a flexible trachea which can hold air and a flexible trachea with gas exchange, respectively.

The main objective of this formulation was to investigate how changes in the insect body pressure caused the tracheal pressure to change, thus allowing inward or outward movement of respiratory gases in the trachea. The mathematical modelling and equations that govern this gas exchange problem formulation were derived based on assuming that air inside the trachea behaves as an ideal gas, assuming a constant temperature, conservation of mass and that gas flow in the trachea was laminar. Equations that govern gas exchange in a flexible trachea during the open spiracle phase were given in section 3.2.2 as a system of nonlinear ordinary differential equations,

$$\frac{df_o}{dt} = \frac{1}{V_T}\left(D_o(p_o - p_{to}) + (f_{oi} - f_o)q_i - f_o(D_o(p_o - p_{to}) + D_c(p_c - p_{tc}))\right), \tag{6.7}$$

$$\frac{df_c}{dt} = \frac{1}{V_T}\left(D_c(p_c - p_{tc}) + (f_{ci} - f_c)q_i - f_c(D_o(p_o - p_{to}) + D_c(p_c - p_{tc}))\right), \tag{6.8}$$

$$\frac{dP_T}{dt} = \frac{E_T}{R_s}(P_s - P_T) + \frac{dP_B}{dt}, \tag{6.9}$$

$$R_s\frac{dV_T}{dt} + V_T E_T = P_s - P_B, \tag{6.10}$$

where $q_i = (P_s - P_T)/R_s$, $p_{to} = f_o(P_T - p_w)$ and $p_{tc} = f_c(P_T - p_w)$. Equations 6.7–6.10 show the rate of change of tracheal concentration of O_2, rate of change of tracheal concentration of CO_2, rate of change of tracheal pressure, and rate of change of tracheal volume, respectively.

These equations are subject to the following initial conditions

$$f_o(0) = 0.1368, \quad f_c(0) = 0.05263, \tag{6.11}$$

$$P_T(0) = 760, \quad V_T(0) = V_0. \tag{6.12}$$

For the closed spiracle phase, equations 6.7 and 6.8 are given by

$$\frac{df_o}{dt} = \frac{1}{V_T}\left(D_o(p_o - p_{to}) - f_o(D_o(p_o - p_{to}) + D_c(p_c - p_{tc}))\right), \tag{6.13}$$

$$\frac{df_c}{dt} = \frac{1}{V_T}\left(D_c(p_c - p_{tc}) - f_c(D_o(p_o - p_{to}) + D_c(p_c - p_{tc}))\right). \tag{6.14}$$

The system of nonlinear equations 6.7 to 6.10 along with the above initial conditions were solved in Chapter 3, where the kinetics of the cell partial pressure, tracheal partial pressure of oxygen

and carbon dioxide, cytoplasm pressure, effect of ventilation on the tracheal partial pressures of both oxygen and carbon dioxide, oxygen uptake by mitochondria, and effects of spiracle opening net gas flow were presented.

6.2.2 *DTM* approach

The Differential Transform Method approach based on Taylor series expansion constructs a solution in the form of a polynomial is developed here to solve the system of equations 6.7−6.10 that describe gas exchange in a flexible trachea during the open spiracle phase. The same method is then employed to solve gas exchange during the closed spiracle phase.

Applying *DTM* to the system of equations 6.7−6.10, one obtains the following recurrence relations

$$\begin{aligned}\sum_{r=0}^{k}\bar{V}_T(r)(k-r+1)\bar{F}_o(k-r+1) &= D_o(p_o-\bar{P}_{to}(k))+\frac{f_{oi}}{R_s}(P_s-\bar{P}_T(k))\\ &-\frac{P_s}{R_s}\bar{F}_o(k)+\frac{1}{R_s}\sum_{r=0}^{k}\bar{P}_T(r)\bar{F}_o(k-r)-(D_op_o+D_cp_c)\bar{F}_o(k)\\ &+D_o\sum_{s=0}^{k}\sum_{r=0}^{s}\bar{F}_o(r)\bar{F}_o(s-r)\bar{P}_T(k-s)-D_op_w\sum_{r=0}^{k}\bar{F}_o(r)\bar{F}_o(k-r)\\ &+D_c\sum_{s=0}^{k}\sum_{r=0}^{s}\bar{F}_o(r)\bar{F}_c(s-r)\bar{P}_T(k-s)-D_cp_w\sum_{r=0}^{k}\bar{F}_o(r)\bar{F}_c(k-r),\end{aligned}\tag{6.15}$$

$$\begin{aligned}\sum_{r=0}^{k}\bar{V}_T(r)(k-r+1)\bar{F}_c(k-r+1) &= D_c(p_c-\bar{P}_{tc}(k))+\frac{f_{ci}}{R_s}(P_s-\bar{P}_T(k))\\ &-\frac{P_s}{R_s}\bar{F}_c(k)+\frac{1}{R_s}\sum_{r=0}^{k}\bar{P}_T(r)\bar{F}_c(k-r)-(D_op_o+D_cp_c)\bar{F}_c(k)\\ &+D_o\sum_{s=0}^{k}\sum_{r=0}^{s}\bar{F}_c(r)\bar{F}_o(s-r)\bar{P}_T(k-s)-D_op_w\sum_{r=0}^{k}\bar{F}_c(r)\bar{F}_o(k-r)\\ &+D_c\sum_{s=0}^{k}\sum_{r=0}^{s}\bar{F}_c(r)\bar{F}_c(s-r)\bar{P}_T(k-s)-D_cp_w\sum_{r=0}^{k}\bar{F}_c(r)\bar{F}_c(k-r),\end{aligned}\tag{6.16}$$

$$(k+1)\bar{P}_T(k+1)=\frac{E_T}{R_s}(P_s-\bar{P}_T(k))+(k+1)\bar{P}_B(k+1),\tag{6.17}$$

$$R_s(k+1)\bar{V}_T(k+1)+E_T\bar{V}_T(k)=P_s-\bar{P}_B(k).\tag{6.18}$$

The tracheal partial pressures of oxygen and carbon dioxide are transformed as

$$p_{to} = f_o(P_T - p_w) \Longrightarrow \sum_{r=o}^{k} \bar{F}_o(r)\bar{P}_T(k-r) - p_w\bar{F}_o(k), \tag{6.19}$$

$$p_{tc} = f_c(P_T - p_w) \Longrightarrow \sum_{r=o}^{k} \bar{F}_c(r)\bar{P}_T(k-r) - p_w\bar{F}_c(k). \tag{6.20}$$

The transformed initial conditions are

$$\bar{F}_o(0) = 0.1368, \quad \bar{F}_c(0) = 0.05263, \tag{6.21}$$

$$\bar{P}_T(0) = 760, \quad \bar{V}_T(0) = V_0. \tag{6.22}$$

The cytoplasm pressure is given as (see equation **??**)

$$P_B = P_s - 0.2R_s\nu\sin(\nu t) - E_T(2.5 - 0.2\cos(\nu t)), \tag{6.23}$$

where ν is the ventilation frequency. Applying DTM to equation 6.23, one obtains

$$\bar{P}_B(k) = P_s - 0.2R_s\frac{\nu^{k+1}}{k!}sin\left(\frac{\pi k}{2!}\right) - E_T\left(2.5 - 0.2\frac{\nu^k}{k!}cos\left(\frac{\pi k}{2!}\right)\right). \tag{6.24}$$

For the closed spiracle phase, equations 6.13 and 6.14 are transformed into

$$\begin{aligned}
\sum_{r=0}^{k} \bar{V}_T(r)(k-r+1)\bar{F}_o(k-r+1) &= D_o(p_o - \bar{P}_{to}(k)) - (D_op_o + D_cp_c)\bar{F}_o(k) \\
&+ D_o\sum_{s=0}^{k}\sum_{r=0}^{s} \bar{F}_o(r)\bar{F}_o(s-r)\bar{P}_T(k-s) - D_op_w\sum_{r=0}^{k}\bar{F}_o(r)\bar{F}_o(k-r) \\
&+ D_c\sum_{s=0}^{k}\sum_{r=0}^{s} \bar{F}_o(r)\bar{F}_c(s-r)\bar{P}_T(k-s) - D_cp_w\sum_{r=0}^{k}\bar{F}_o(r)\bar{F}_c(k-r),
\end{aligned} \tag{6.25}$$

$$\begin{aligned}
\sum_{r=0}^{k} \bar{V}_T(r)(k-r+1)\bar{F}_c(k-r+1) &= D_c(p_c - \bar{P}_{tc}(k)) - (D_op_o + D_cp_c)\bar{F}_c(k) \\
&+ D_o\sum_{s=0}^{k}\sum_{r=0}^{s} \bar{F}_c(r)\bar{F}_o(s-r)\bar{P}_T(k-s) - D_op_w\sum_{r=0}^{k}\bar{F}_c(r)\bar{F}_o(k-r) \\
&+ D_c\sum_{s=0}^{k}\sum_{r=0}^{s} \bar{F}_c(r)\bar{F}_c(s-r)\bar{P}_T(k-s) - D_cp_w\sum_{r=0}^{k}\bar{F}_c(r)\bar{F}_c(k-r).
\end{aligned} \tag{6.26}$$

The system of equations 6.15–6.20 is an iterative formula for constructing a series solution as follows in table 6.1:

k	$k+1$	$\bar{F}_o(k+1)$	$\bar{F}_c(k+1)$	$\bar{P}_T(k+1)$	$\bar{V}_T(k+1)$
0	1	-0.00848	0.00267	757.960	0.43999
1	2	208.250	79.9253	758.875	0.36391
2	3	-486.241	-560.122	759.032	0.15293
3	4	159172.51	61873.457	758.80875	0.0965727
4	5	-728448.83	-852184.91	758.78124	0.0953058
⋮	⋮	⋮	⋮	⋮	⋮

TABLE 6.1: Differential transformation values for $k = 0, 1, 2, \ldots$

The terms in table 6.1 may be taken as far as desired. However, it has been shown in the literature that after a certain number of iterations, the approximate solutions converge to the exact solutions for some systems of differential equations. Substituting the entries of table 6.1 into equation 6.2, one obtains the following system of equations

$$P_T(t) = \sum_{k=0}^{\infty} \bar{P}_T(k)t^k = 760 + 757.960t + 758.875t^2 + 759.032t^3 + 758.80875t^4 + \ldots \tag{6.27}$$

$$V_T(t) = \sum_{k=0}^{\infty} \bar{V}_T(k)t^k = 0.001 + 0.43999t + 0.36391t^2 + 0.15293t^3 + 0.0965727t^4 + \ldots \tag{6.28}$$

$$f_o(t) = \sum_{k=0}^{\infty} \bar{F}_o(k)t^k = 0.1368 - 0.00848t + 208.250t^2 - 486.241t^3 + \ldots \tag{6.29}$$

$$f_c(t) = \sum_{k=0}^{\infty} \bar{F}_c(k)t^k = 0.05263 + 0.00267t + 79.9253t^2 - 560.122t^3 + \ldots \tag{6.30}$$

The series solution for the closed spiracle phase can be constructed from the entries in table 6.2:

k	$k+1$	$\bar{F}_o(k+1)$	$\bar{F}_c(k+1)$
0	1	-0.0084890237	0.0026700243
1	2	0.0161095443	0.0200880765
2	3	-0.0390045773	-0.0374027063
3	4	0.1017760659	0.1043272009
4	5	-0.2833129326	-0.2843764947
5	6	0.8192412634	0.8253339407
6	7	-2.4357311004	-2.4478955007
7	8	7.38831474308	7.4227321453
⋮	⋮	⋮	⋮

TABLE 6.2: Closed phase differential transformation values for $k = 0, 1, 2, \ldots$

Substituting the entries from table 6.2 into equation 6.2, we obtain

$$f_o(t) = \sum_{k=0}^{\infty} \bar{F}_o(k)t^k = 0.1368 - 0.008489t + 0.016109t^2 - 0.039004t^3 + \dots \tag{6.31}$$

$$f_c(t) = \sum_{k=0}^{\infty} \bar{F}_c(k)t^k = 0.05263 + 0.002670t + 0.020088t^2 - 0.037402t^3 + \dots \tag{6.32}$$

6.2.3 Results and discussion

In this section, results are presented from the DTM computations and compared with the cases for open and closed spiracle phases. In Table 6.3 the DTM solutions are shown for the closed spiracle phase and compared with $NDSolve$ in Mathematica. Furthermore, the DTM solutions are plotted in Figure 6.1.

t	$DTM\ f_o$	$NDSolve\ f_o$	Error	$DTM\ f_c$	$NDSolve\ f_c$	Error
0.05	0.1363	0.1359	0.000400	0.05280	0.05294	0.000140
0.10	0.1360	0.1357	0.001357	0.05299	0.05299	0.000000
0.15	0.1357	0.1355	0.000199	0.05342	0.05304	0.000380
0.20	0.1354	0.1354	0.000000	0.05378	0.05308	0.000699
0.25	0.1352	0.1352	0.000000	0.05427	0.05312	0.001150
0.30	0.1348	0.1351	0.000299	0.05488	0.05317	0.001710
0.35	0.1339	0.1350	0.001100	0.05605	0.05320	0.002850
0.40	0.1308	0.1348	0.004400	0.05831	0.05324	0.005070

TABLE 6.3: Results of the DTM for the closed spiracle phase for oxygen and carbon dioxide concentration.

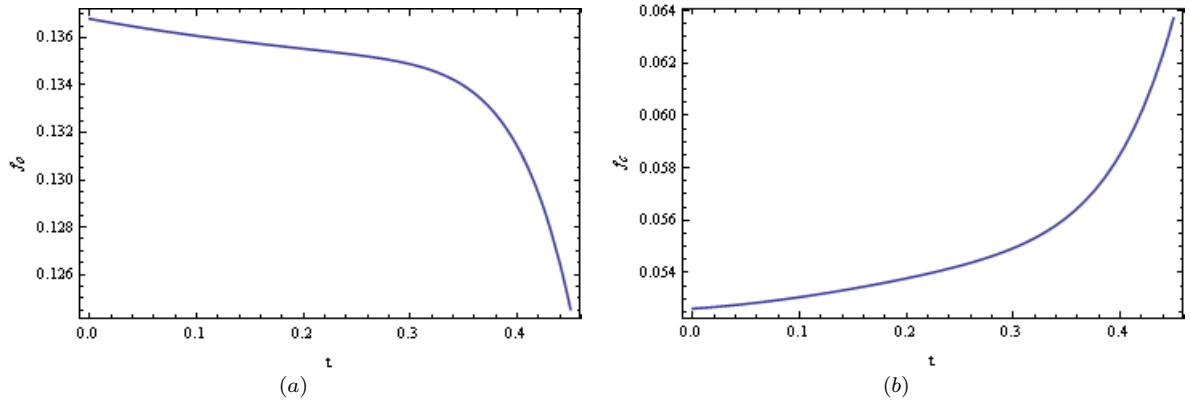

(*a*) (*b*)

FIGURE 6.1: DTM results for the gas concentrations for the closed spiracle phase. (a) Oxygen concentration. (b) Carbon dioxide concentration.

The results from the DTM are very interesting and consistent with the biology interpretation. There is agreement between the DTM results and $NDSolve$ solver as shown in Table 6.3. For the oxygen concentration during the closed spiracle phase, an absolute error of approximately

10^{-4} produced by DTM for $\mathcal{O}(8)$. This further confirms that the DTM converges faster compared to $NDSolve$. It also provides good results with minimum computational work. With the DTM performing better in terms of accuracy and effectiveness for the closed spiracle phase, we then solve the other problems for which constructing exact solutions would be hard.

In Figure 6.1(a), we observe that the tracheal oxygen concentration decreases with prolonged spiracle closure. During the closed spiracle phase, oxygen stored in the trachea and tracheoles is depleted as a result of cellular respiration. Carbon dioxide is produced as a result of this cellular respiration, and so there is a build up of carbon dioxide in the trachea during this phase. Figure 6.1(b) shows this build up of tracheal carbon dioxide. Carbon dioxide continues building up in the trachea until a certain threshold that triggers spiracle opening is reached. The results of the DTM analysis are consistent with processes in insect respiration.

In Chapter 2, it was shown that water loss in the trachea scales positively to carbon dioxide emission/build up. In fact, it was shown that $0.013ml$ of water is lost per unit of carbon dioxide emitted through the spiracles. Water is only lost when the spiracles open to release carbon dioxide. A DTM solution for the water expression in system 2.4 would show a build up of water in the trachea during the closed spiracle phase. A plot of this solution would be similar to Figure 6.1(b).

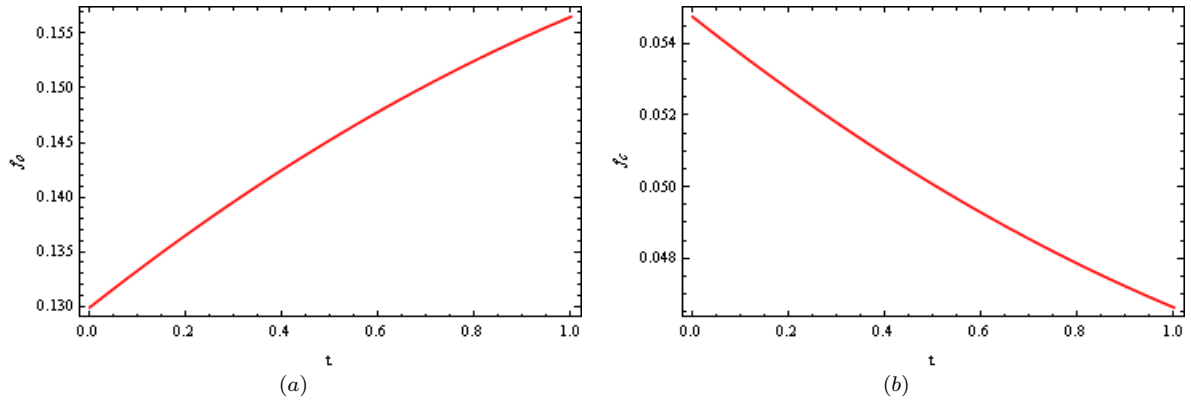

FIGURE 6.2: DTM results for the gas concentrations for the closed spiracle phase. (a) Oxygen concentration. (b) Carbon dioxide concentration.

In Figure 6.2, the DTM solution is shown for the gas concentrations during the open spiracle phase. Likewise, the DTM results are consistent with biological observations. During the open spiracle phase, there is an outward elimination of carbon dioxide from the trachea (see section 1.2.2). Figure 6.2(b) shows that the tracheal concentration of carbon dioxide decreases with extended open spiracle phase. Figure 6.2(a) shows the dynamics of oxygen concentration during the open phase. There is a build up of oxygen reserves in the trachea and tracheoles, hence the observed upward slope of f_o. A DTM plot of the water content in the trachea during this phase shows a decline in water levels during this phase. Excessive water loss during this phase

may lead to dessication and so the spiracle must close quickly in order for the insect to remain hydrated. The exact carbon dioxide or oxygen value that triggers spiracle closure is, to the best of my knowledge, not yet fully understood. Studying the dynamics of both f_o and f_c as $t \to \infty$ during either phase might lead to a breakthrough in determining the O_2 and CO_2 thresholds that trigger both spiracle closure and opening.

6.3 Numerical validation of the tracheal induced pumping model

Applying DTM to validate the tracheal induced pumping model is not considered in this thesis, but forms part of ongoing research.

6.4 Concluding remarks

In this chapter, DTM was applied successfully to obtain numerical solutions for nonlinear systems of ordinary differential equations describing movement of respiratory gases in a flexible trachea. DTM is an effective and reliable tool for deriving solutions of systems of nonlinear ordinary differential equations. The method gives rapidly converging series solutions, which can be written in exact closed form. The accuracy of the obtained solution can be improved by including more terms in the solution. DTM reduces the computational difficulties associated with other traditional methods and all the calculations can be performed from simple manipulations. The rapid convergence show that the method is reliable and introduces a significant improvement in solving differential equations over existing methods. DTM results are consistent with biological observations. This correlation further substantiates that our model system correctly traces the dynamics of respiratory gases. DTM can be utilized as an alternative approach to current techniques being employed to a wide variety of physical problems.

Chapter 7

Microscale gaseous slip flow in the insect trachea and tracheoles

The work in this chapter has been submitted to *Applied Mathematics and Computation.*

An analytical investigation into compressible gas flow with slight rarefactions through the insect trachea and tracheoles during the closed spiracle phase is undertaken, and a complete set of asymptotic analytical solutions is presented. We first obtain estimates of the Reynolds and Mach numbers at the channel terminal ends where the tracheoles directly deliver respiratory gases to the cells, by comparing the magnitude of the different forces in the compressible gas flow. The 2D Navier-Stokes equations with a slip boundary condition are used to investigate compressibility and rarefied effects in the trachea and tracheoles. Expressions for the velocity components, pressure gradients and net flow inside the trachea are then presented. Numerical simulations of the tracheal compressible flow are performed to validate the analytical results from this study. Novel devices for microfluidic compressible flow transport may be invented from results obtained in this study.

7.1 Introduction

Transport of fluids within a complex network of microchannels is a challenging and important problem in many scientific applications. Microchannels are important components for microfluidic devices and in recent years research topics studying gas flows in these microchannels have gained more attention. These channels are typically of the order of microns with applications in drug delivery, DNA chips and inkjet printheads [114]. In these applications, the microchannels are used to efficiently move, mix or separate small amounts of fluids [116].

Current techniques used in microscale fluid transport include conventional pressure-driven flow and valveless mechanisms such as electro-osmotic and peristaltic. The drawback with pressure-driven flows is that they are insufficient whenever the channel geometry becomes small, since an excessive pressure drop is required to overcome emerging surface forces. Although commercially viable, functional drawbacks of valveless mechanisms are that they are heavily reliant on elastic wall tube induced wave dynamics [117, 118]. With current technology, manufacturing an entire elastic microfluidic device is difficult.

In designing these microfluidic devices, many unexpected phenomena have been observed due to the small size of the gas flow tubes. Chaotic phenomena have been observed in experimental measurements by Arkilic *et al*, [114]. They found that a velocity slip exists on the channel wall and that the pressure distribution inside a microchannel is nonlinear. Pong *et al*. [147] showed empirically that compressibility is an important feature for microscale. Arkilic *et al*. [114] and Zohar *et al*. [148] went on to find analytical solutions for flow distributions along the channel with an isothermal assumption. Over and above the analytical solutions presented, numerical solutions of the Navier-Stokes equations for flows with slight slip flows have been presented. Note that for flows in microchannels, the Navier-Stokes equations are applicable if a slip boundary condition is used [143]. Beskok and Karniadikis [149] numerically showed that mass flow within a tube may be enhanced by both slip and thermal creep effects. Other numerical simulations of compressible flows in a microchannel include the direct simulation Monte Carlo (DSMC) method [154, 155], the BGK-Burnett method [157], and the information preserving method [156]. The DSMC approach has been shown to be valid for the full range of flow regimes.

The present study is motivated by phenomena observed in insect respiratory systems. The insect respiratory system is composed of a complex network of gas filled tubes, called the trachea, that bifurcate into all parts of the insect body delivering oxygen and removing carbon dioxide [52–54, 57, 59, 60]. Oxygen enters the insect through spiracles, flows in the trachea and at the end of the smallest tracheal tube (about 2 to 5 μm in diameter) are the tracheoles, each less than 1 μm in diameter, that penetrate the cell to provide an interface for gas exchange with a living cell [59]. Oxygen flows through the trachea by a combination of ventilation and diffusion along a concentration gradient. The insect respiratory gas exchange process involves both convective and diffusive transport modes at the microscale, convection as a result of internal pressure gradients that are responsible for producing or enhancing both directed and tidal airflows [122]. Recent studies have observed rhythmic wall contractions at multiple locations in the insect tracheal tubes [47–49, 61, 133–135]. The rapid cycles of compression and expansion are believed to be the main driving force for transporting air [49, 61]. They are assumed to be a naturally efficient pumping mechanism in a complex network of microscale channels. Flow transport induced by these wall contractions can either be peristaltic (propagative) or non-peristaltic (non-propagative).

During periods of inactivity, the spiracles of some insects, such as the dung beetle, are mostly shut only opening periodically [52–54, 57, 146]. Thus, external exchange of respiratory gases is discontinuous. When the spiracles are closed, cellular respiration in the body causes oxygen partial pressure within the trachea to drop until a certain threshold level is reached at which the spiracles rapidly open [146]. The rapid cycles of compression and expansion have been observed in insects at rest. During the compression phase, respiratory gases are compressed in the confined tracheal spaces. The flow is hypothesized to be fast so as the gases can be squeezed to the distal ends of the insect body parts. That is, the density within these microchannels is a non-constant function of pressure, temperature, phase and composition. For the flow in the trachea and tracheoles when the spiracles are completely closed, it is hypothesized that pressure and density change rapidly through the region space where the fluid is flowing while temperature does not change significantly.

In this manuscript we first use the Navier-Stokes equations with a slight slip boundary condition to model the observed phenomena. We then develop a nondimensionalization of the governing equations. Based on the fact that momentum changes along the flow direction, we then perform an order estimation for the Reynolds and Mach numbers at the terminal ends of the tracheoles. Viscous force and pressure drop must be balanced everywhere in the space in which the fluid flows. With a quasi-isothermal assumption, we then obtain expressions for the velocity components, pressure gradients and net flow inside the trachea and tracheoles. Lastly, numerical simulations of compressible gas flow inside the microchannel are carried out to validate the analytical conclusions obtained. Motivated by the insect respiratory system [47, 53, 54, 61] a bioinspired paradigm for flow transport in a complex network of channels is proposed. The possibility of using this setup as a microscale fluid transport mechanism is investigated. We hope the results can be used in the fabrication of commercially viable and efficient microfluidic devices for compressible flow.

7.2 The model system

7.2.1 Formulation

In this section we formulate and present a mathematical model for compressible fluid flow in the insect trachea during the closed spiracle phase. Consider two-dimensional (2D) compressible flow in a channel of length L and breadth B, without any wall movement. The rendering in the thorax of an insect is complex and three-dimensional (3D). The 2D geometry without any wall contractions is used to simplify the theoretical analysis. Define the aspect ratio (width-to-length ratio) as δ^{-1} which is assumed to be very large ($\delta = B/L \ll 1$). For a channel that has a very high aspect ratio, neglecting variations in the z direction is valid and it can be shown

that the error from neglecting these variations is only proportional to the inverse of the square of the aspect ratio [114]. Both the lower wall, W_1, and upper wall, W_2, are kept stationary and straight at all times. The geometry for our channel analysis is shown in figure 7.1.

Due to the small size of the insect, we assume that tracheal flow is quai-isothermal instead of the exact thermal assumption used by many researchers. This is because for microscale flow, pressure and density change rapidly through the flow region space while temperature actually does not change significantly. For this model, we assume the inlet pressure is several times larger than the outlet pressure, i.e a nonzero pressure drop, $\triangle p \neq 0$, along the channel length. The averaged outlet quantities are used to normalize the governing equations in system 7.1 and boundary conditions. The compressible Newtonian flow is quasi-isothermal with constant viscosity μ and velocity field $\mathbf{V} = (u, v, 0)$.

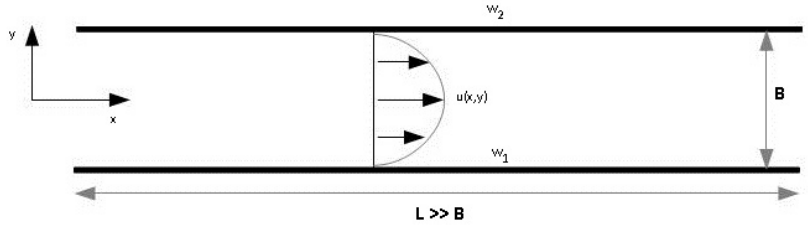

FIGURE 7.1: Problem schematic: geometry for 2D channel analysis, with a flow profile at a given position. The streamwise velocity profile and the slip velocity changes as flow proceeds downstream.

7.2.2 Mathematical model for the microscale fluid flow

Define u as the streamwise velocity component along the x direction and v as the wall-normal component along the vertical direction, y. The time-invariant constant-viscosity 2D Navier-Stokes equations for compressible flow, ignoring body forces, in Cartesian coordinates are given by

$$\left.\begin{aligned} \frac{\partial(\rho u)}{\partial x} + \frac{\partial(\rho v)}{\partial y} &= 0 \\ \rho\left(u\frac{\partial u}{\partial x} + v\frac{\partial u}{\partial y}\right) &= -\frac{\partial p}{\partial x} + \mu\left(\frac{\partial^2 u}{\partial x^2} + \frac{\partial^2 u}{\partial y^2} + \frac{1}{3}\left(\frac{\partial^2 u}{\partial x^2} + \frac{\partial^2 v}{\partial x \partial y}\right)\right) \\ \rho\left(u\frac{\partial v}{\partial x} + v\frac{\partial v}{\partial y}\right) &= -\frac{\partial p}{\partial y} + \mu\left(\frac{\partial^2 v}{\partial x^2} + \frac{\partial^2 v}{\partial y^2} + \frac{1}{3}\left(\frac{\partial^2 v}{\partial y^2} + \frac{\partial^2 u}{\partial x \partial y}\right)\right) \end{aligned}\right\}. \tag{7.1}$$

The equation of state for an ideal gas is given by

$$p = \rho \mathcal{R} T = nkT, \tag{7.2}$$

while the shear stress expression is given by

$$\tau_{xy} = \mu \left(\frac{\partial v}{\partial x} + \frac{\partial u}{\partial y} \right). \tag{7.3}$$

p is the pressure, μ is the gas viscosity, ρ is the density and $\mathcal{R}$ is the specific gas constant. The energy balance equation is given by

$$\rho C_p \left(u\frac{\partial T}{\partial x} + v\frac{\partial T}{\partial y} \right) = u\frac{\partial p}{\partial x} + v\frac{\partial p}{\partial y} + k\left(\frac{\partial^2 T}{\partial x^2} + \frac{\partial^2 T}{\partial y^2} \right) + \mu \left(2\left(\frac{\partial u}{\partial x} \right)^2 + 2\left(\frac{\partial v}{\partial y} \right)^2 + \left(\frac{\partial v}{\partial x} + \frac{\partial u}{\partial y} \right)^2 - \frac{2}{3}\left(\frac{\partial u}{\partial x} + \frac{\partial v}{\partial y} \right)^2 \right), \tag{7.4}$$

where C_p is the specific heat at constant pressure and k is the Boltzmann constant.

The boundary conditions are that the vertical component v vanishes at the solid walls and the streamwise velocity u is equal to the slip velocity,

$$v_{w_i} = 0, \quad y = \pm B/2 \tag{7.5}$$

$$u_{W_i} = \mp\sigma\lambda \left. \frac{\partial u}{\partial y} \right|_{W_i} + \frac{3}{4}\frac{\mu}{\rho T_{w_i}} \left. \frac{\partial T}{\partial x} \right|_{W_i}, \quad y = \pm B/2 \tag{7.6}$$

$$p(0) = p_i, \qquad p(L) = p_o, \tag{7.7}$$

where λ is the mean free path and $\sigma = (2 - \sigma_m)/\sigma_m$. σ is the streamwise momentum accommodation and σ_m is the tangential momentum accommodation coefficient ($0 \leq \sigma_m \leq 1$. For specular or zero accommodation, $\sigma = 0$, while for full accommodation, $\sigma = 0$).

We also consider a temperature jump on the top and bottom walls such that

- at $y = B/2 : T - T_{W_2} = -\left(\frac{2 - \sigma_T}{\sigma_T} \right) \frac{2\gamma}{Pr(\gamma + 1)} \lambda \left. \frac{\partial T}{\partial y} \right|_{W_2}$,
- at $y = -B/2 : T - T_{W_1} = \frac{2 - \sigma_T}{\sigma_T} \frac{2\gamma}{Pr(\gamma + 1)} \lambda \left. \frac{\partial T}{\partial y} \right|_{W_1}$,

where σ_T is the energy accommodation coefficient, Pr is the Prandtl number and γ is the specific heat ratio.

We introduce the following non-dimensional parameters $\tilde{x} = x/L$, $\tilde{y} = y/B$, $\tilde{W}_1 = W_1/B$, $\tilde{W}_2 = W_2/B$, $\tilde{v} = v/u_o$, $\tilde{u} = u/u_o$, $\tilde{\rho} = \rho/\rho_o$, $\tilde{T} = T/T_o$, $\tilde{p} = p/p_o$, $\tilde{\tau}_{xy} = \tau_{xy}B/(\mu u_o)$, $Ma = u_o/\sqrt{\gamma \mathcal{R} T}$, $Re = (B u_o \rho_o)/\mu$, $Pr = C_p \mu/k$ and $Kn = \lambda/B$. u_o, p_o, T_o and ρ_o are the average outflow gas properties of streamwise velocity, pressure, temperature and density at the tips of the tracheoles, respectively. Ma, Re, Pr and Kn are the Mach number, Reynolds number, Prandtl number and Knudsen number or the ratio of the mean-free path to the characteristic

channel dimension B, respectively. The degree of rarefaction is conventionally expressed through this overall Knudsen number [145]. Substituting the above non-dimensional parameters into the system 7.1, the governing equations reduce to

$$\left.\begin{aligned}
\delta\frac{\partial(\tilde{\rho}\tilde{u})}{\partial\tilde{x}}+\frac{\partial(\tilde{\rho}\tilde{v})}{\partial\tilde{y}} &= 0\\
\tilde{\rho}\left(\delta\tilde{u}\frac{\partial\tilde{u}}{\partial\tilde{x}}+\tilde{v}\frac{\partial\tilde{u}}{\partial\tilde{y}}\right) &= -\frac{\delta}{\gamma Ma^2}\frac{\partial\tilde{p}}{\partial\tilde{x}}+\frac{1}{Re}\left(\delta^2\frac{\partial^2\tilde{u}}{\partial\tilde{x}^2}+\frac{\partial^2\tilde{u}}{\partial\tilde{y}^2}+\frac{1}{3}\left(\delta^2\frac{\partial^2\tilde{u}}{\partial\tilde{x}^2}+\delta\frac{\partial^2\tilde{v}}{\partial\tilde{x}\partial\tilde{y}}\right)\right)\\
\tilde{\rho}\left(\delta\tilde{u}\frac{\partial\tilde{v}}{\partial\tilde{x}}+\tilde{v}\frac{\partial\tilde{v}}{\partial\tilde{y}}\right) &= -\frac{1}{\gamma Ma^2}\frac{\partial\tilde{p}}{\partial\tilde{y}}+\frac{1}{Re}\left(\delta^2\frac{\partial^2\tilde{v}}{\partial\tilde{x}^2}+\frac{\partial^2\tilde{v}}{\partial\tilde{y}^2}+\frac{1}{3}\left(\frac{\partial^2\tilde{v}}{\partial\tilde{y}^2}+\delta\frac{\partial^2\tilde{u}}{\partial\tilde{x}\partial\tilde{y}}\right)\right)\\
\tilde{p} &= \tilde{\rho}\tilde{T}
\end{aligned}\right\}, \tag{7.8}$$

The non-dimensional velocity slip and boundary conditions on the wall at $\tilde{y}=\pm 0.5$

$$\tilde{u}_{w_i}=\mp\sigma Kn\left.\frac{\partial\tilde{u}}{\partial\tilde{y}}\right|_{W_i}+\frac{3}{4}\frac{\delta}{Re\tilde{\rho}\tilde{T}_{w_i}}\left.\frac{\partial\tilde{T}}{\partial\tilde{x}}\right|_{W_i}, \tag{7.9}$$

$$\tilde{T}-\tilde{T}_{W_i}=\mp\left(\frac{2-\sigma_T}{\sigma_T}\right)\frac{2\gamma}{Pr(\gamma+1)}Kn\left.\frac{\partial\tilde{T}}{\partial\tilde{y}}\right|_{W_i}, \tag{7.10}$$

$$\tilde{p}(0)=P, \qquad \tilde{p}(1)=1. \tag{7.11}$$

A value of $\sigma=1$ has been used for most engineering problems although values for $\sigma<1$ have been reported under controlled test conditions [114, 140–142]. Also, condition (7.9) is commonly used in rarefied gas flows and represents the first-order correction to the Navier-Stokes equations to account for nonequilibrium effects [114].

7.2.3 Control of the flow regime

Based on the work of Cai *et al*. [143], taking a small slice of the region in which the fluid flows, as shown in figure 7.2, the momentum, pressure drop and viscous force change through this small control volume must be such that

$$\frac{B}{2}\frac{\partial p}{\partial x}\triangle x+\frac{B}{2}\rho_o u_o\frac{\partial u}{\partial x}\triangle x\simeq\mu\left.\frac{\partial u}{\partial x}\right|_{W_i}. \tag{7.12}$$

We express the gradient terms as

$$\frac{\partial p}{\partial x}\sim\frac{p_o-p_i}{L}, \qquad \frac{\partial u}{\partial x}\sim\frac{u_o-u_i}{L}, \qquad \frac{\partial u}{\partial y}\sim\frac{u_o-u_{W_i}}{B}\sim\frac{u_o}{B}, \tag{7.13}$$

where the subscripts o, i and W_i represent quantities at the tips of the tracheoles, at the inlet (spiracula opening) and at the channel wall respectively. We make the assumption that the streamwise velocity component at the walls is significantly smaller than at the inlet and that

the velocity component u has a profile close to a linear relation along x-direction. Since the channel geometry is restricted to a very high aspect ratio ($1 \ll \delta^{-1}$) and flow is at the microscale, we are dealing with a low Reynolds number flow regime. The above relations are more fitting for laminar flow than for turbulent flow. The Reynolds number is therefore limited to $Re < 300$.

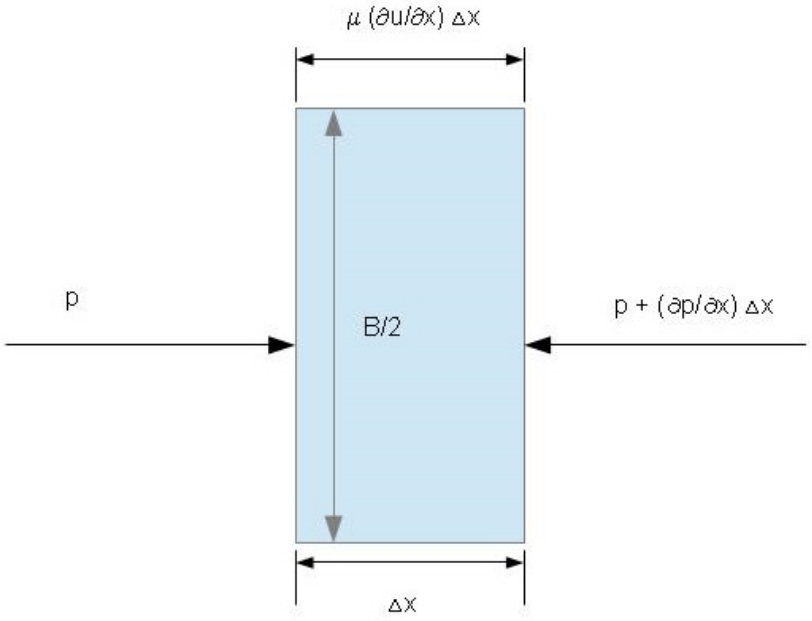

FIGURE 7.2: A slice of the flow region showing the pressure drop and momentum change in the tracheoles.

We also assume that the inlet pressure is several times larger than the pressure at the tips of the tracheoles, i.e. $p_i \gg p_o$, then

$$u_i^2 = u_o^2 \left(\frac{p_o}{p_i}\right)^2 \ll u_o^2. \tag{7.14}$$

Using this relation (7.14) and substituting the linear relations in (7.13) while neglecting $u_i u_o$, equation 7.12 can be written as

$$\delta(p_o - p_i) + \rho_o \delta u_o^2 \simeq 2\mu \left(\frac{u_o}{B}\right). \tag{7.15}$$

Defining the ratio between the inlet pressure and the pressure at the tracheole tips as $P = p_i/p_o$, equation 7.15 can further be simplified to

$$\underbrace{\mathcal{O}(\delta Ma^{-2}(1-P))}_{\text{pressure drop term}} \sim \underbrace{\mathcal{O}(\delta\gamma)}_{\text{convection term}} + \underbrace{\mathcal{O}(\gamma/Re)}_{\text{viscous term}}. \tag{7.16}$$

From equation 7.16, the two nondimensional parameters, Re and Ma, control the flow regime, and within the context of perturbation expansion, they can independently have three values, $\mathcal{O}(\delta)$, $\mathcal{O}(1)$ and $\mathcal{O}(1/\delta)$, leading to nine independent flow regimes [114]. Using the fact that for microchannels, the reciprocal of the aspect ratio is significantly less than unity i.e. $\delta \in [10^{-5}, 10^{-1}]$, we explore the possibilities that may arise from the three terms in equation 7.16.

Case 1:

The convection term balances with the pressure drop term while the viscous term is of order δ^2 or higher, i.e. $\delta Ma^{-2}(1-P) \sim \gamma\delta$ while $\gamma/Re = \mathcal{O}(\gamma\delta^2)$ or higher. From this relation, we obtain that $Ma \sim \mathcal{O}(1)$ while $Re \sim \mathcal{O}(\delta^{-2})$ or higher. $Re \sim \mathcal{O}(\delta^{-2}) \Rightarrow Re > 300$ and as such suggesting turbulent flow. A turbulent flow state in the trachea or tracheoles invalidates the linear assumption of the velocity profiles and so for our model, this case is invalid.

Case 2:

The viscous term balances the convection term and the pressure drop is smaller, i.e. $\gamma\delta \sim \gamma/Re$ while $\delta Ma^{-2}(1-P) = \mathcal{O}(\gamma\delta^2)$ or $\delta Ma^{-2}(1-P) = \mathcal{O}(\gamma\delta^3)$.

$$\delta Ma^{-2}(1-P) = \gamma\delta^2 \tag{7.17}$$

$$Ma^2 = \frac{1-P}{\gamma\delta}. \tag{7.18}$$

From the above relations, we obtain that $Re \sim \mathcal{O}(\delta^{-1})$ while $Ma \sim \mathcal{O}(\delta^{-1/2})$ or $Ma \sim \mathcal{O}(\delta^{-1})$. Values of the Mach number between $1.2 < Ma < 5$ involves supersonic flows while $5 < Ma < 10$ involve hypersonic flow. This case is also neglected for our analysis because such flows are not physically possible inside the trachea and tracheoles without electric or magnetic effects.

Case 3:

The viscous term and pressure drop terms balance while the convection term is small, i.e. $\delta Ma^{-2}(1-P) \sim \gamma/Re$ while the convection term is small.

$$\delta Ma^{-2}(1-P) = \frac{\gamma}{Re} \tag{7.19}$$

$$Ma = \sqrt{\frac{Re\delta(1-P)}{\gamma}}. \tag{7.20}$$

From the above relation, we obtain that

1. $Ma \sim \mathcal{O}(\delta^{1/2})$ iff $Re \sim \mathcal{O}(1)$,
2. $Ma \sim \mathcal{O}(\delta)$ iff $Re \sim \mathcal{O}(\delta)$,
3. $Ma \sim \mathcal{O}(\delta^{3/2})$ iff $Re \sim \mathcal{O}(\delta^2)$.

Abobelkassem and Staples [133–135], Arkilic *et al.* [114] and Cai *et al.* [143] all adopted the case where $Ma \sim \mathcal{O}(\delta)$ and $Re \sim \mathcal{O}(\delta)$ in their analysis.

Case 4:

The pressure drop, convection and viscous terms are of the same order, i.e. $\delta Ma^{-2}(1-P) \sim \gamma\delta \sim \gamma/Re$. This yields $Ma \sim \mathcal{O}(1)$ while $Re \sim \mathcal{O}(\delta^{-1})$. This case represents transonic Fanno flow in which there exists a balance between viscous pressure and inertial forces.

With kinetic gas theory, the Knudsen number can also be expressed in terms of Re and Ma as

$$Kn = \sqrt{\frac{\pi\gamma}{2}}\frac{Ma}{Re}. \tag{7.21}$$

Using this equation, Table 7.1 summarizes the four cases above and shows the combinations of Ma and Re with the corresponding Kn values.

Ma	Re	Kn	Comments
$\mathcal{O}(1)$	$\mathcal{O}(\delta^{-2}$	$\mathcal{O}(\delta^2)$	Invalid as it violates the linear assumption of the velocity profiles, i.e. $Re > 300 \Rightarrow$ turbulent flow .
$\mathcal{O}(\delta^{-1/2})$	$\mathcal{O}(\delta^{-1})$	$\mathcal{O}(\delta^{1/2})$	This case involves supersonic flow.
$\mathcal{O}(1)$	$\mathcal{O}(\delta^{-1})$	$\mathcal{O}(\delta)$	Transonic Fanno flow and is best analyzed by assuming a friction factor and solving integral forms of the momentum equations [114, 144].
$\mathcal{O}(\delta)$	$\mathcal{O}(\delta)$	$\mathcal{O}(1)$	Creeping microscale flow inside the trachea.
$\mathcal{O}(\delta^{1/2})$	$\mathcal{O}(1)$	$\mathcal{O}(\delta^{1/2})$	Moderate microscale flow inside the trachea.
$\mathcal{O}(\delta^{3/2})$	$\mathcal{O}(\delta^2)$	$\mathcal{O}(\delta^{-/2})$	Extremely slow gas flow inside the trachea .

TABLE 7.1: The different Mach and Reynolds numbers with corresponding flow regimes.

Table 7.1 shows one case of not strictly continuum flow where the flow has a Knudsen number of $\mathcal{O}(1)$. The pressure drop, $\triangle p$, is the only driving force of the compressible flow down the trachea and tracheoles without any wall movement. The flow down the trachea may only be slowed down by the viscous force on the walls. We assume there are no electric or magnetic field effects on the flow and so we neglect cases of supersonic flow. We also neglect the case producing an extremely slow gas flow inside the trachea. We then focus on the cases where $Re = \mathcal{O}(\delta)$ and $Re = \mathcal{O}(1)$, i.e.,

1. Group 1: $Ma \sim \mathcal{O}(\delta^{1/2})$, $Re \sim \mathcal{O}(1)$, $Kn \sim \mathcal{O}(\delta^{1/2})$
2. Group 2: $Ma \sim \mathcal{O}(\delta)$, $Re \sim \mathcal{O}(\delta)$, $Kn \sim \mathcal{O}(1)$

For both these cases

$$\delta Ma^{-2}(1-P) = \frac{\gamma}{Re} \quad \text{and so,} \tag{7.22}$$

$$\frac{Re}{Ma^2} = \frac{\gamma}{\delta(1-P)}, \tag{7.23}$$

$$\frac{Re}{Ma^2} \sim \mathcal{O}(\delta^{-1}). \tag{7.24}$$

The ratio of the inlet spiracula pressure and outlet pressure, P, and the viscous friction force are of the same leading order in these two cases.

7.2.4 Solutions

From the continuity equation in system 7.8, we see that the highest order v term that is required to satisfy the equation is $\mathcal{O}(\delta)$. For the case where the Reynold's number is of the same order as the reciprocal of the channel aspect ration, i.e. $Re \in [0, \delta]$ (case where $Ma \sim \mathcal{O}(\delta)$, $Re \sim \mathcal{O}(\delta)$ and $Re/Ma^2 \sim \mathcal{O}(1/\delta)$), we discard all terms that of order δ^2 in system 7.8 and higher since $\delta \ll 1$. The y-momentum equation then becomes

$$\tilde{\rho} Re \tilde{v} \frac{\partial \tilde{v}}{\partial \tilde{y}} = -\frac{Re}{\gamma Ma^2} \frac{\partial \tilde{p}}{\partial \tilde{y}} + \frac{4}{3} \frac{\partial^2 \tilde{v}}{\partial \tilde{y}^2} + \frac{1}{3} \delta \frac{\partial^2 \tilde{u}}{\partial \tilde{x} \partial \tilde{y}}. \tag{7.25}$$

From equation 7.25, we see that at $\mathcal{O}(1/\delta)$ the static pressure is uniform along y and varies only with x, i.e.

$$\tilde{p} = \tilde{p}(\tilde{x}). \tag{7.26}$$

If we ignore terms of $\mathcal{O}(\delta^2)$ or higher, the x-momentum equation becomes

$$\tilde{\rho} Re \tilde{v} \frac{\partial \tilde{u}}{\partial \tilde{y}} = -\frac{\delta Re}{\gamma Ma^2} \frac{\partial \tilde{p}}{\partial \tilde{x}} + \frac{\partial^2 \tilde{u}}{\partial \tilde{y}^2} + \frac{1}{3} \left(\delta \frac{\partial^2 \tilde{v}}{\partial \tilde{x} \partial \tilde{y}} \right). \tag{7.27}$$

Using the fact that the highest order v component is $\mathcal{O}(\delta)$, equation 7.27 at $\mathcal{O}(1)$ can be written as

$$0 = -\frac{\delta Re}{\gamma Ma^2} \frac{\partial \tilde{p}}{\partial \tilde{x}} + \frac{\partial^2 \tilde{u}}{\partial \tilde{y}^2}. \tag{7.28}$$

Equation 7.28 can be directly integrated twice with respect to y and the associated boundary conditions can be applied. An explicit formula for the axial velocity component u is

$$\tilde{u}(\tilde{x},\tilde{y}) = \frac{1}{8}\frac{\delta Re}{\gamma Ma^2}\frac{d\tilde{p}}{d\tilde{x}}(4\tilde{y}^2 - 1 - 4\sigma Kn). \tag{7.29}$$

The axial velocity component is based on the overall Knudsen number Kn at the tips of the tracheoles. However, it can also be expressed as a function of the local Knudsen number defined by Glowinski and Lichnewsky [145] as $Kn = (\lambda/\alpha)(\partial\alpha/\partial x)$. x is the linear dimension while α is any macroscopic flow variable such as density, velocity or temperature. We define this local Knudsen number as $Kn = Kn/\tilde{\rho}$. Using the non-dimensional ideal gas law in system 7.8 and the value of $\tilde{T}$ as discussed below, the local Knudsen number can also be defined as $Kn = Kn/\tilde{p}_1$. As such, the axial velocity component in equation 7.29 can the be written as a function of the local Knudsen number Kn.

Following the work of Arkilic *et al.* [114], we can expand

$$\tilde{u} = \tilde{u}_1 + \delta\tilde{u}_2 + \delta\tilde{u}_3 + \ldots \tag{7.30}$$

$$\tilde{v} = \delta\tilde{v}_2 + \delta^2\tilde{v}_3 + \ldots \tag{7.31}$$

$$\tilde{p} = \tilde{p}_1 + \delta\tilde{p}_2 + \delta^2\tilde{p}_3 + \ldots \tag{7.32}$$

$$\tilde{\rho} = \tilde{\rho}_1 + \delta\tilde{\rho}_2 + \delta^2\tilde{\rho}_3 + \ldots \tag{7.33}$$

$$\tilde{T} = \tilde{T} + \delta\tilde{T}_2 + \delta^2\tilde{T}_3 + \ldots \tag{7.34}$$

Using the continuity equation is system 7.8, it is clear that the v term that is required to satisfy the differential continuity equation is $\mathcal{O}(\delta)$. Based on the work of Cai *et al.* [143], we assume that $T = 1$ as well because for fluid flow in a microchannel, temperature does not change significantly while pressure and density change rapidly through the region of flow i.e. $\tilde{T} = 1 + \delta\tilde{T}_2 + \delta^2\tilde{T}_3 + \ldots$.

Using this and the state equation that $\tilde{p} = \tilde{\rho}\tilde{T}$, we have from the continuity equation,

$$\delta\frac{\partial(\tilde{\rho}\tilde{u})}{\partial\tilde{x}} + \frac{\partial(\tilde{\rho}\tilde{v})}{\partial\tilde{y}} = 0, \tag{7.35}$$

$$\delta\frac{\partial(\tilde{p}_1\tilde{u}_1)}{\partial\tilde{x}} + \delta\frac{\partial(\tilde{p}_1\tilde{v}_2)}{\partial\tilde{y}} = 0, \tag{7.36}$$

$$\frac{\partial(\tilde{p}_1\tilde{u}_1)}{\partial\tilde{x}} + \frac{\partial(\tilde{p}_1\tilde{v}_2)}{\partial\tilde{y}} = 0. \tag{7.37}$$

By using the principle of conservation of mass given in system 7.37 and using the related boundary conditions, the vertical velocity component $\tilde{v}_2(\tilde{x},\tilde{y})$ is given as

$$\tilde{v}_2(\tilde{x},\tilde{y}) = -\frac{1}{\tilde{p}_1}\int \frac{\partial(\tilde{p}_1\tilde{u}_1)}{\partial\tilde{x}}d\tilde{y}, \tag{7.38}$$

$$= -\frac{1}{\tilde{p}_1}\frac{\delta Re}{24\gamma Ma^2}\tilde{y}\left(\frac{d^2\tilde{p}_1}{d\tilde{x}^2}\left(\left(4\tilde{y}^2-3\right)\tilde{p}_1 - 12\mathrm{Kn}\sigma\right) + \left(4\tilde{y}^2-3\right)\left(\frac{d\tilde{p}_1}{d\tilde{x}}\right)^2\right). \tag{7.39}$$

Along the wall surfaces where $y = \pm 1/2$, $\tilde{v} = 0$ and so evaluating equation 7.39 at the wall results in

$$0 = \frac{d^2\tilde{p}_1}{d\tilde{x}^2}\left(\tilde{p}_1 + 6\sigma\mathrm{Kn}\right) + \left(\frac{d\tilde{p}_1}{d\tilde{x}}\right)^2. \tag{7.40}$$

We obtain the zeroth-order pressure distribution by solving equation 7.40 and using boundary condition (7.11). This yields

$$\tilde{p}_1(\tilde{x}) = -6\mathrm{Kn}\sigma + \sqrt{36\mathrm{Kn}^2\sigma^2 + 12\mathrm{Kn}P\sigma - 12\mathrm{Kn}P\sigma\tilde{x} + 12\mathrm{Kn}\sigma\tilde{x} - P^2\tilde{x} + P^2 + \tilde{x}}, \tag{7.41}$$

$$= -6\mathrm{Kn}\sigma + \sqrt{-12\mathrm{Kn}P\sigma(\tilde{x}-1) + 12\mathrm{Kn}\sigma(3\mathrm{Kn}\sigma+\tilde{x}) - (\tilde{x}-1)P^2 + \tilde{x}}. \tag{7.42}$$

The pressure gradient is given by

$$\frac{\partial\tilde{p}_1}{\partial\tilde{x}} = -\frac{(P-1)(12Kn\sigma + P + 1)}{2\sqrt{36Kn^2\sigma^2 + 12Kn\sigma(P+\tilde{x}-\tilde{x}P) + P^2 + \tilde{x} - \tilde{x}P^2}}. \tag{7.43}$$

The temperature distribution inside the trachea is obtained from the non-dimensional energy balance equation

$$\tilde{\rho}\left(\delta\tilde{u}\frac{\partial\tilde{T}}{\partial\tilde{x}} + \tilde{v}\frac{\partial\tilde{T}}{\partial\tilde{y}}\right) = \delta\frac{(\gamma-1)}{\gamma}\tilde{u}\frac{\partial\tilde{p}}{\partial\tilde{x}} + \frac{(\gamma-1)}{\gamma}\tilde{v}\frac{\partial\tilde{p}}{\partial\tilde{y}} + \frac{1}{PrRe}\left(\delta^2\frac{\partial^2\tilde{T}}{\partial\tilde{x}^2} + \frac{\partial^2\tilde{T}}{\partial\tilde{y}^2}\right)$$
$$+ \frac{Ma^2(\gamma-1)}{Re}\left(2\delta^2\left(\frac{\partial\tilde{u}}{\partial\tilde{x}}\right)^2 + 2\left(\frac{\partial\tilde{v}}{\partial\tilde{y}}\right)^2 + \left(\delta\frac{\partial\tilde{v}}{\partial\tilde{x}} + \frac{\partial\tilde{u}}{\partial\tilde{y}}\right)^2 - \frac{2}{3}\left(\delta\frac{\partial\tilde{u}}{\partial\tilde{x}} + \frac{\partial\tilde{v}}{\partial\tilde{y}}\right)^2\right). \tag{7.44}$$

At order $\mathcal{O}(1)$ and using the fact that $\tilde{v} = \tilde{v}_1 + \delta\tilde{v}_2 + \delta^2\tilde{v}_3 + \ldots$, equation 7.44 can be written as

$$0 = \frac{1}{RePr}\frac{\partial^2\tilde{T}}{\partial\tilde{y}^2} + \frac{Ma^2(\gamma-1)}{Re}\left(\frac{\partial\tilde{u}}{\partial\tilde{y}}\right)^2. \tag{7.45}$$

Integrating equation 7.45 twice with respect to $\tilde{y}$ and using conditions (7.10), we easily obtain the temperature solution as

$$\tilde{T}(\tilde{x},\tilde{y}) = T_W - \frac{(\gamma-1)PrRe^2\delta^2}{\gamma^2 Ma^2}\left(\frac{\partial\tilde{p}}{\partial\tilde{x}}\right)^2\frac{\tilde{y}^3}{6} - \frac{(\gamma-1)\delta^2Re^2(16\gamma Kn(\sigma_T-2)-(\gamma+1)Pr\sigma_T)}{192\gamma^2(\gamma+1)Ma^2\sigma_T}\left(\frac{d\tilde{p}}{d\tilde{x}}\right)^2. \tag{7.46}$$

The wall shear stress is given by

$$\tilde{\tau}_{xy}(\tilde{x},\tilde{y}) = \frac{\delta Re}{\gamma Ma^2}\frac{d\tilde{p}}{d\tilde{x}}\tilde{y}. \tag{7.47}$$

Lastly, mass flow through the tracheal system for given spiracular (inlet) and tracheole tip (outlet) pressure can be calculated by multiplying equation 7.29 by the density and integrating across the channel. Thus, the steady non-dimensional mass flow rate is given

$$Q(\tilde{x}) = \int_{0.5}^{-0.5}\tilde{\rho}\tilde{u}(\tilde{x},\tilde{y})d\tilde{y}, \tag{7.48}$$

$$= -\frac{\rho}{8}\frac{\delta Re}{\gamma Ma^2}\frac{d\tilde{p}}{d\tilde{x}}\left(\frac{2}{3}+4\sigma Kn\right). \tag{7.49}$$

Evaluating equation 7.49 at $x = 1$, we have the non-dimensional mass flow given by

$$Q(1) = \frac{\rho\delta Re}{24\gamma Ma^2}(P-1)(1+P+12\sigma Kn). \tag{7.50}$$

Key results from equation 7.50 is that for a given pressure ratio P, the rarefaction acts to increase the observed non-dimensional mass flow. We also observe that the effect of slip becomes a more significant contributor to mass flow as the pressure ratio decreases. Recall that $Re = (Bu_o\rho_o)/\mu$, we have that the mass flow rate at $x = 1$ is very sensitive to the channel width B.

The solutions obtained above are not general, but satisfy the assumptions made in formulating the model system. As such, there may exist many other asymptotic solutions with different combinations of Re and Ma. The presented solutions are correct to the indicated order of magnitude, i.e. $\tilde{v}$ to $\mathcal{O}(\delta)$ and $\tilde{u}$ to $\mathcal{O}(1)$. Equation 7.29 indicates a parabolic streamwise velocity profile which changes slowly down L as the pressure drops. The temperature distribution in equation 7.46 is derived by assuming a quasi-isothermal condition, which is only valid for slow speed microchannel flows with very small temperature variations. For high speed gas microscale flows, this quasi-isothermal assumption may be invalid.

7.3 Results and Discussion

We present some numerical simulations of the results obtained. The parameters that appear more frequently in the manuscript are listed in table 7.2 (unless stated otherwise in the text). The parameter values are estimated from literature data and in cases where they could not be found, they were estimated. The parameters presented are for oxygen. The model can still be extended to include all the respiratory gases such as carbon dioxide and water vapor.

Parameters		
Symbol	Meaning	Initial value
$\delta = B/L$	Width-to-length ratio	0.05 (estimated from data by Nation [59])
p_i	oxygen inlet pressure (spiracular pressure)	21.1 kPa [73, 151]
p_o	oxygen pressure at the tracheole tips	2.66 kPa [73, 151]
T_W	Channel wall temperature	25^oC / $298.15K$ (assumed)
μ	Viscosity	0.77 [143]
Ma	Mach number at the tracheole tips	1.3×10^{-4} (assumed)
Re	Reynolds number	1.5×10^{-4} (assumed)
σ_m	Streamwise momentum accommodation	1.08108 (calculated from data by Arkilic *et al.* [114])
σ_T	Energy accommodation coefficient	0.85 [143]

TABLE 7.2: Parameter list.

7.3.1 Pressure distribution along the channel length

Using the expression for the pressure given in equation 7.44, the predicted pressure is plotted in figure 7.3. We consider the cases where the pressure is distributed in a channel with width $0.5\mu m$ with no rarefaction, i.e. the outlet Knudsen number is zero, and the case where the Knudsen number at the tips of the tracheoles is non-zero ($Kn = 0.05$). For both cases, the non-dimensional pressure distribution along the axial direction is nonlinear. Changes in the density of oxygen in the trachea and tracheoles is hypothesized to cause this nonlinearity (see [114]). We also notice that a moderate Knudsen number diminishes the nonlinear negative curvature observed in the pressure distribution.

7.3.2 Streamwise and wall normal velocity components along the axial direction

Figures 7.4 (a) and (b) show the non-dimensional streamwise and wall normal velocity components, respectively. Figure 7.4 (b) nicely shows how the velocity at the wall behaves as the pressure begins to drop. In figure 7.5, both the axial and vertical velocity components along the centerline $y = 0$ are shown. The shear stress at the upper wall is also monitored at this centerline.

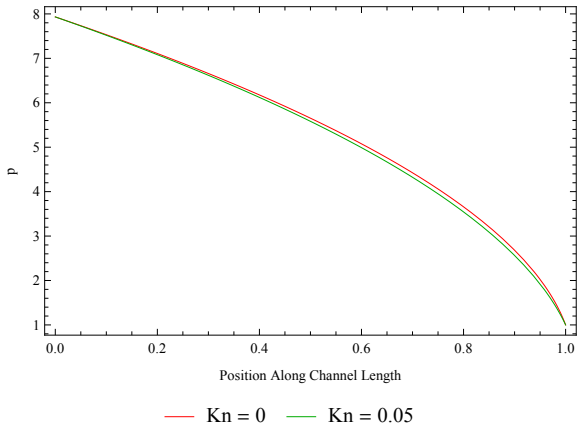

FIGURE 7.3: Pressure distribution in the trachea and tracheoles.

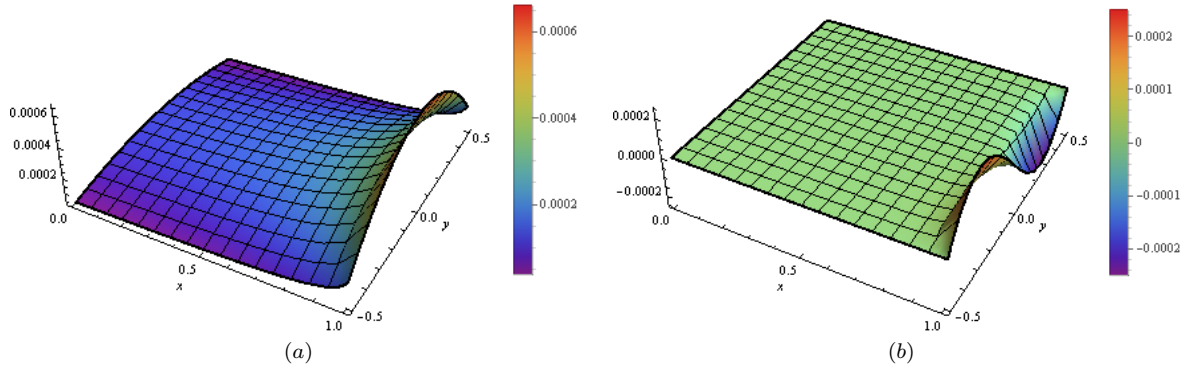

FIGURE 7.4: 3D plot of the velocity components for $kn = 0.125$. (a) The non-dimensional streamwise velocity distribution in the tracheal system. (b) The wall-normal velocity component in the trachea.

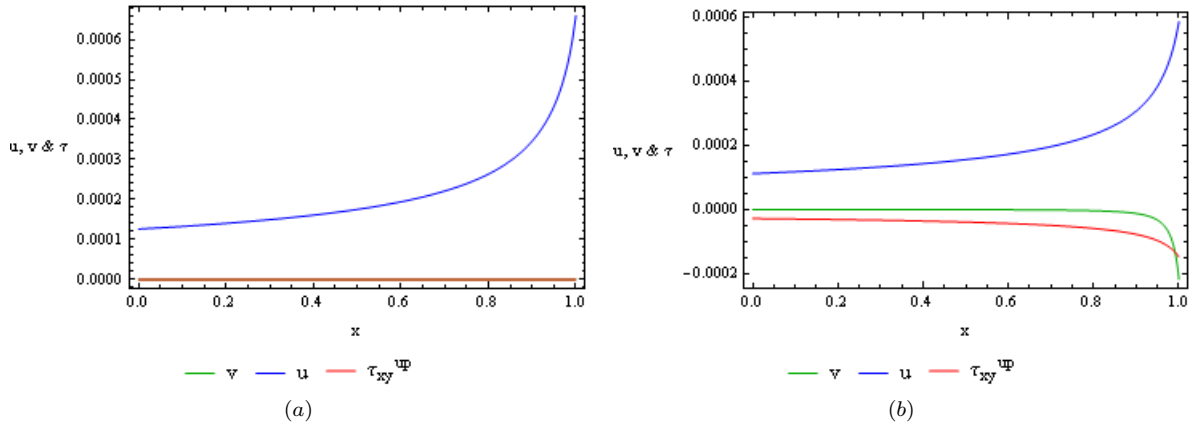

FIGURE 7.5: Distribution of flow velocity components and wall shear stress along the axial direction for $Kn = 0.125$ and pressure ratio $P = 7.93233$ at (a) $y = 0$ and (b) $y = 0.2$.

At the centerline where $y = 0$, the wall shear stress due to the flow motions is constant and equal to zero (see figure 7.5(a)) due to the existence of an inactive zone with zero wall normal velocities. For $y \neq 0$, the wall shear stress responds to pressure gradient variations. A nonzero wall shear stress in the region between the two walls is observed because of both the wall-normal and streamwise flow motions. The streamwise velocity component, u, in figure 7.5(a) shows that there will be flow that exits the channel on one side. The vertical velocity component v is zero at the centerline $y = 0$ and nonzero for $y = 0.2$ (see figure 7.5(b)). This is ideal when considering the requirement to enforce mass continuity. The fluid velocity must move from the tube centerline towards the wall. The nonzero wall normal velocity component away from the tube centerline shows mass flow towards the tracheal wall as flow progresses downstream.

7.3.3 Streamwise and wall normal velocity components along the vertical direction

In figure 7.6 we present the streamwise and wall normal velocity profiles along the y-direction at four locations along the tracheal length ($x = 0, 0.25, 0.5, 0.75$). The profiles for the streamwise component for $Kn = 0.125$ and pressure ratio 7.93233 are given in figure 7.6(a). The curves are parabolic and attain maximum values away from both the upper and lower walls. Likewise, figure 7.6(b) presents the wall normal velocity components along the y-axis at the same four locations.

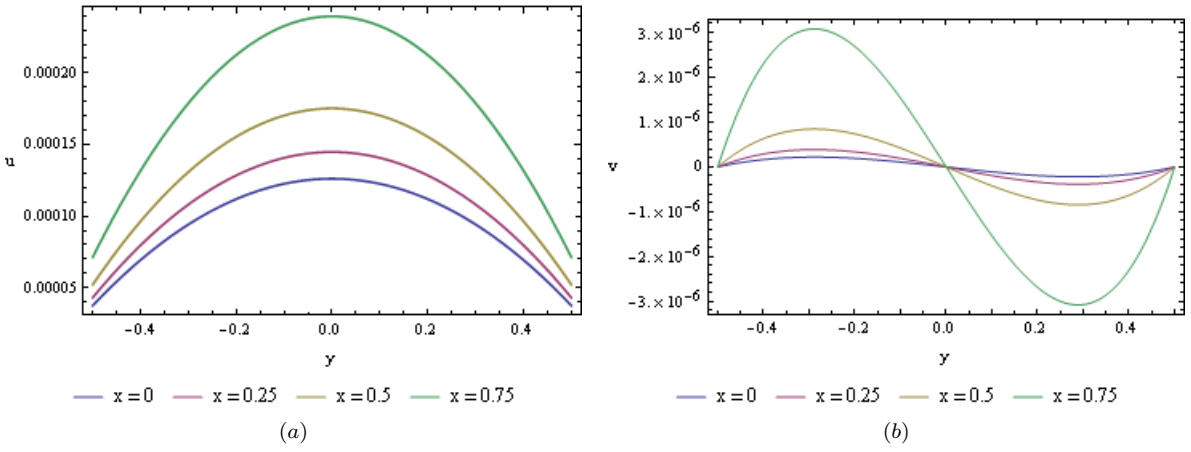

FIGURE 7.6: Flow components along the y-direction for $Kn = 0.125$ and pressure ratio $P = 7.93233$ at four locations ($x = 0, 0.25, 0.5, 0.75$). (a) Streamwise velocity component distribution. (b) Wall normal velocity component distribution.

An interesting result from these plots is that no zero-velocity profiles are observed. All the profiles are characterized by the existence of flow transport between the two walls. This indicates that flow transport and net flow out of this system can be produced.

7.3.4 Net mass flow

To ascertain if the current system layout does indeed produce unidirectional flow, we investigate how the net mass flow rate as given in equation 7.49 behaves along the axial direction. Equation 7.49 is obtained by integrating the axial velocity component over the complete vertical channel length. To impose mass continuity, velocity must drift from the channel centerline towards the walls. Figure 7.7 plots $Q(\tilde{x})$ over the entire characteristic tracheal system length. As can be seen, as x increases, net flow changes dramatically. The mass drifts down the stream as the flow progresses down the tracheal length. These results lead us to propose the following hypothesis: by using a similar channel without any wall contractions, net flow is produced and the system can be used as a simple "pumping" mechanism in a microscale gas flow regime.

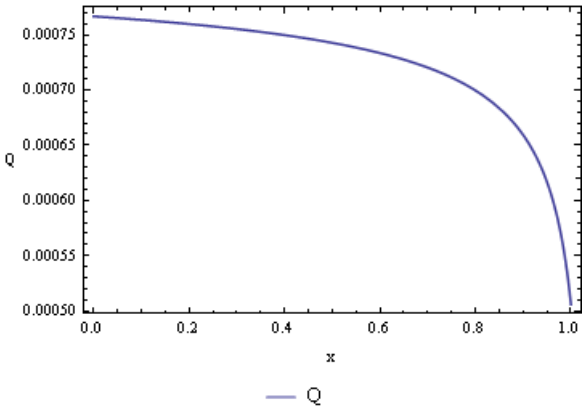

FIGURE 7.7: Non-dimensional mass-flow distribution in the tracheal system as given in equation 7.49 for pressure ratio $P = 7.93233$ and $Kn = 0.125$.

The effect of the slip condition in equation 7.9 can be clearly depicted by dividing the slip-flow mass-flow solution in equation 7.50 by the mass flow when the slip condition is ignored (i.e evaluate equation 7.50 with $Kn = 0$). This yields

$$\frac{Q(1)}{Q_{ns}(1)} = 1 + \frac{12\sigma Kn}{P+1}, \tag{7.51}$$

where Q_{ns} is the no-slip mass flow. As the pressure ratio in the trachea approaches unity, the tracheal slip mass flow increase significantly over that which would otherwise be predicted from a no-slip solution. Figure 7.8 shows the plot of the no-slip non-dimensional mass flow distribution. Comparing the mass flow distribution in figures 7.7 and 7.8, we see that slip mass flow is enhanced as compared to the no-slip mass flow.

Further, in figure 7.9 we show mass flow evaluated at $x = 1$ as a function of the inlet-outlet pressure ratio for $Kn = 0$ and $Kn = 0.125$. A weak nonlinear relationship between mass flow rate and pressure ratio is observed. The effect of the slip boundary condition is nicely depicted as well. For a given pressure ratio, the slip condition tends to enhance net flow compared to the no-slip condition.

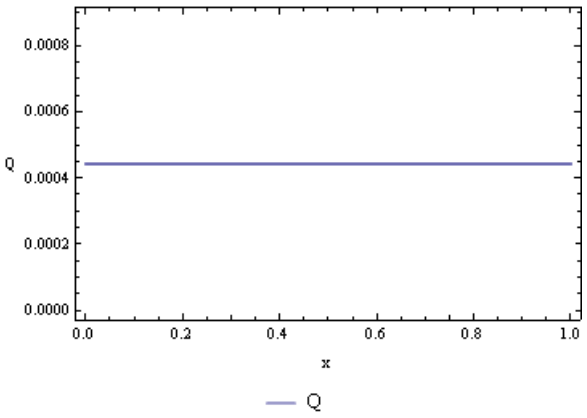

FIGURE 7.8: No-slip non-dimensional mass-flow distribution in the tracheal system for the pressure ratio $P = 7.93233$.

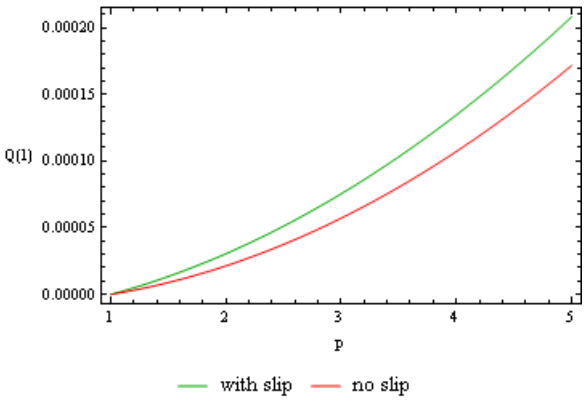

FIGURE 7.9: Mass flow rate as a function of the pressure ratio assuming the tangential momentum accommodation coefficient of $\sigma_m = 0.85$ for $Kn = 0$ (no-slip solution) and $Kn = 0.125$.

Figure 7.10 shows the relationship between mass flow rate at the channel end and the channel aspect ratio, δ, with fixed pressure ratio $P = 7.93233$ for $Kn = 0$ and $Kn = 0.125$. A positive linear relationship between the two quantities is observed with the slip condition enhancing net flow. This validates equation 7.50.

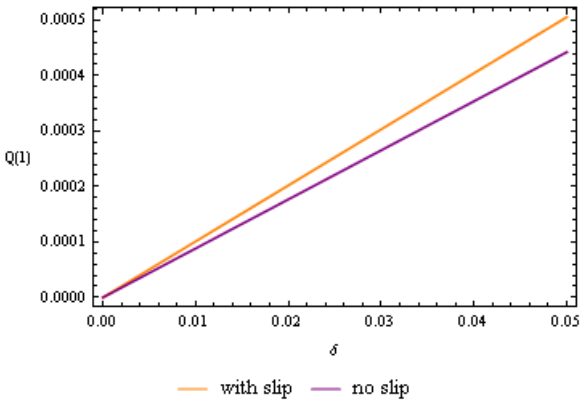

FIGURE 7.10: Mass flow rate as a function of the aspect ratio, δ, assuming the tangential momentum accommodation coefficient of $\sigma_m = 0.85$ for $Kn = 0$ (no-slip solution) and $Kn = 0.125$.

7.3.5 The Mach and Reynolds numbers

In this section, we validate the Mach-Reynolds number relationship in equation 7.23 by performing some model simulations. Amongst the most important findings of this research work, we seek to validate the tracheal wall Mach and Reynolds numbers relationship at the tracheole tips. We are very interested in what happens where gas molecules are exchanged with the respiring cell. The effect of metabolic activity on oxygen molecules uptake in this gas exchange interchange region can be quantified by comparing the relationship between the two numbers. Hence, for slip wall or no-slip wall boundary conditions, we seek to confirm the relationship between the Mach and Reynolds numbers at the tracheole tips.

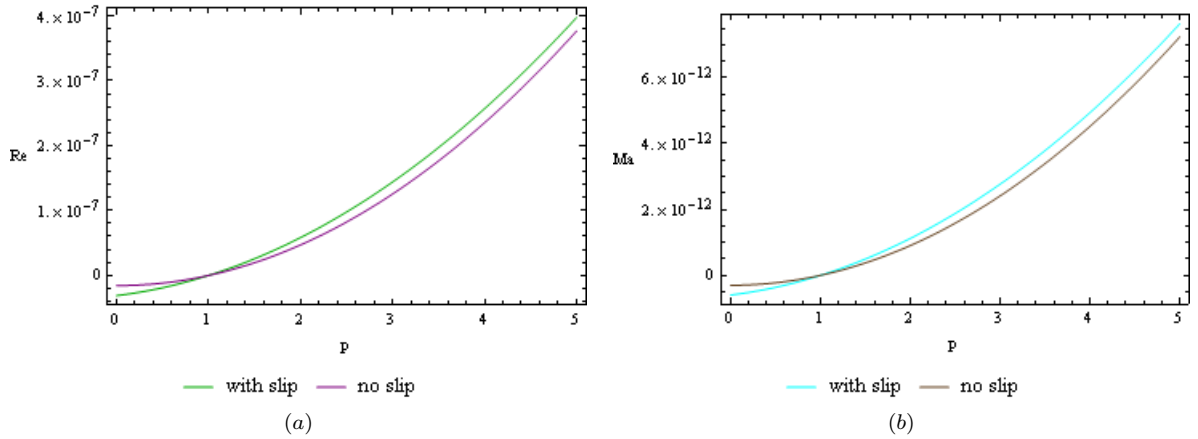

FIGURE 7.11: Variations in the Reynolds and Mach numbers as functions of pressure ratio P at the tracheole tips for the two groups in section 7.2.3. (a) Reynolds number for no-slip and slip boundary conditions. (b) Mach number for no-slip and slip boundary conditions.

Figure 7.11 shows the Reynolds and Mach numbers at the tracheole tips for the two cases in section 7.2.3 and equation 7.23. Both plots show that for pressure ratios greater than unity ($P > 1$), the slip flow cases have larger Reynolds and Mach numbers. This can be attributed to the larger exit velocities. We also see that the Mach numbers are certainly smaller than the corresponding Reynolds numbers for the two cases.

7.4 Conclusion

The analysis presented traces movement of respiratory gases in an insect trachea when the spiracles are completely sealed. The results presented are similar to those obtained by Arkilic *et al.* [114]. A non-zero wall normal velocity, which is required to satisfy the differential continuity expression in system 7.8, is predicted. The pressure distribution also includes the formal contribution of rarefaction waves.

In summary, the following results are obtained:

- By quantifying the magnitudes of the different forces inside the trachea and tracheoles, i.e. pressure drop, viscous force and convection term (momentum change), we obtain a fundamental relationship given by equation 7.23. This relationship links the Reynolds and Mach numbers at the tips of the tracheoles with the pressure drop ratio, P, and the tracheal channel aspect ratio, δ. Arkilic *et al.* [114] illustrated one special case estimation of the Reynolds and Mach numbers. Cai *et al.* [143] illustrated more estimates for the Mach and Reynolds numbers using a similar relationship. The obtained relationship can be utilized in future studies to construct different orders of the Reynolds and Mach numbers.
- Equation 7.46 presents a detailed temperature field obtained by adopting a quasi-isothermal assumption instead of the isothermal assumption which was used by many other researchers.
- The non-dimensional mass flow rate follows equation 7.49 and figures 7.9 and 7.10. Figure 7.9 shows that the pressure ratio has a weak nonlinear effect on net mass flow rate. This is because the pressure ratio has effects on the Reynolds number as well.

The presented model predicts an increase in respiratory gas net mass flow for given spiracular and tracheole tip pressures for microscale flows. The wall normal velocity profiles and pressure distribution predict a transfer of mass from the tracheal centerline to the tracheal wall for efficient supply of oxygen to respiring cells for metabolism.

Chapter 8

Conclusions and future work

Inspired by observed phenomena in insect tracheal systems, mathematical models that explain respiratory gas movement and solve for the induced flow transport in confined geometries were derived. Models for gas exchange at the tracheol tips with respiring cells were presented, expressions for tracheal partial pressures of the respiratory gases, rate of change of gas concentrations, rate of tracheal volume change, spiracle behaviour on net gas flow, cellular respiration and tissue absorption, and global movement within the insect were modelled. Further, theoretical analysis of fluid flow models was based on lubrication theory and quasi-steady approximations, which model flow transport at low Reynolds number regimes, $Re \in [0, \delta]$ where δ is the tube aspect ratio. Analytical expressions for the velocity field, wall shear stress, pressure, and net mass flow were derived. Estimates of the Reynolds and Mach numbers at the tips of the tracheoles were determined. All these flow components were derived for both no-slip and slip boundary conditions.

For the wall induced net mass flow, the flow field structures during both compressions and expansion times that are imposed by wall contractions were calculated explicitly. The net flow rate over a complete collapse-relaxation cycle was presented and given as a function of the time lag and tube configurations. Similarly, the compressible net mass flow rate was given as a function of the pressure ratio, rarefaction, and slip. The rarefaction was observed to increase observed mass flow while the effect of slip became a more significant contributor to mass flow as the pressure ratio decreased. The tracheal wall induced flow model was then optimized using the constrained optimization technique to determine the geometric and spatial design parameters that maximized the time averaged net flow. Optimization results showed that very close to each other, wide and deep contractions moving with a different phase lag resulted in increased net flow.

This thesis, proposed three main novel mathematical models to explain insect respiratory gas exchange phenomena, namely:

1. A new mathematical model for the simultaneous movement of gases across the insect spiracles. The presented model investigated and analyzed respiratory gas interaction by deriving a system of ordinary differential equations for oxygen, carbon dioxide and water vapor. The developed model revealed that changes in CO_2 elimination is directly related to the level of O_2 uptake into the trachea, while the change in water levels in the trachea is directly proportional to CO_2 emission.

2. Models that examine diffusion; How the gases are transfered from one respiratory chamber to the next, and how oxygen enters the respiring cells. With the isothermal assumption, expressions for the tracheal partial pressures of oxygen and carbon dioxide, rate of volume change, and the rate of changes of oxygen concentration and carbon dioxide concentration were derived. The effects of some flow parameters such as diffusion capacities, reaction rates and air concentrations on net flow were also studied. Numerical simulations of the tracheal flow were performed.

3. Models for tracheal fluid transport: Inspired by the internal flow distributions of respiratory gases produced by rhythmic wall contractions in insect tracheal networks, a paradigm for selectively pumping and controlling gases at the microscale in a complex network of channels was presented. The concept presented enables fluids to be transported, controlled and directed into specific branches in networks while avoiding other possible branching routes, without the use of any mechanical valves. Another model investigating compressible gas flow with slight rarefactions through the insect trachea and tracheoles during the closed spiracle phase was presented. Using this model, estimates of the Reynolds and Mach numbers at the channel terminal ends where the tracheoles directly deliver respiratory gases to the cells were determined.

The results presented in this thesis are expected to be helpful in understanding discontinuous gas exchange in insects. For instance, the results of simultaneous movement of respiratory gases across the spiracles provide a starting point to illustrate how changes in water levels in the trachea is directly proportional to carbon dioxide emission. The diffusion and convection based models of discontinuous gas exchange in the trachea presented low-order expressions of the tracheal partial pressures of oxygen and carbon dioxide, rate of tracheal volume change, and changes of gas concentrations, of which there is to the best of my knowledge not much reported in the literature. Further, the Differential Transform Method was adopted to solve the derived system of nonlinear ordinary differential equations for both the open and closed spiracle phases. This pioneering work should be useful to insect respiratory researchers interested in quantifying gas exchange. Results from fluid transport are expected to be helpful in mimicking features of physiological systems in efforts to manufacture novel efficient microfluidic devices.

The focus on fluid transport yielded two novel models, one for tracheal wall induced fluid flow observed during the open spiracle phase, while the second flow model considered gas flow

during the closed spiracle phase. The incompressible fluid flow model proposed a novel pumping paradigm that was neither propagative nor belonging to the electro-osmotic class of pumping mechanisms found in the literature. The presented model was inspired by rhythmic tracheal contractions which have been observed in insects. These contractions are expected to function in complex networks of the microscale regime within simple tube geometries. The results have highlighted the ability of producing unidirectional net flow by using an inelastic tube with at least two contractions that move with a time lag with respect to each other. Both theoretical analysis and Differential Transform Method were used to solve for the $2D$ viscous flow transport in the trachea and tracheoles with prescribed moving wall contractions. In both fluid flow models, the theoretical analysis was based on both steady approximations at low Reynolds number flow regime and lubrication theory.

The main numerical outcome of this study was the ability of applying DTM in obtaining semi-analytical solutions of the flexible tracheal models with gas exchange. DTM was applied to both cases when the spiracles were open and closed, respectively. We also applied DTM on the tracheal wall induced flow model. A bivalidation process for both the analytical and numerical approaches was performed. Both the analytical and numerical results were used to validate the assumptions made in the derivation of the theoretical model. The DTM results were consistent with results on insect physiology. They captured respiratory dynamics during both open and closed spiracle phases. The correlation between DTM solutions and insect respiratory dynamics further substantiated that our model system correctly traced the movement of tracheal respiratory gases. DTM was shown to be efficient in solving systems of nonlinear ordinary differential equations. DTM offers significant advantages in terms of its straightforward applicability, its computational effectiveness and its accuracy.

Future work that arises from insect respiration includes developing a model to show how the observed patterns of CO_2 released during the flutter phase of DGC may be generated. Experimentally, the discussion of the phase space map only briefly mentioned the problem of fluttering as an oscillation phenomenon around the O_2 threshold. This can be carried out by considering each trachea segment as an independent oscillator. Van der Kloot [158] showed that each segment independently controls its spiracles. By understanding how endotracheal partial pressures induce spiracle opening and closing, it is possible to describe how regular micro-cycles might be generated in a single segment. However, the organization of insects is metameric consisting of multiple connected segments. This connection results in the coupling of the single segment oscillators and so it is necessary to develop a mathematical model defining this coupling.

Apart from the biological questions that still need to be answered, the mathematical models presented in this thesis can be extended. The tracheal wall induced flow model may be extended to include multiple contractions to find a proper collapsing protocol that has the ability of transporting and manipulating fluids as well as controlling the fluid directionality in a complex

network of branching channels. The model could then be numerically validated using either the differential transform method or Stokelets-meshfree computations. Further, the three dimensional numerical methods can be used to solve for the induced tube structures with moving contractions. Symmetric and asymmetric contractions may be studied to determine optimal contraction shapes inducing net flow. Another future question to consider is addressing the unavailability of a number of parameters. Although parameters that are structurally identifiable in a model might be estimated by modern parameter estimation techniques, there remains a need to access most of the derived models parameters. It is possible to estimate some parameters on an individual basis by using the right choice of observation functions.

In summary, the present study attempted to answer the following questions: How do respiratory gases manage to move in opposite directions simultaneously across the insect spiracles and how does extended spiracle opening influence the influx of gases into the trachea. Novel paradigms by which oxygen is transported and absorbed by respiring cells at the tracheol tips, the phenomenon by which carbon dioxide is removed from respiring cells via the tracheal network, as well as new paradigms which trace microscale fluid flow in the tracheal network are proposed. The present study ideally provides initial guidelines in fully understanding insect respiratory gas exchange and also provides guidelines for the fabrication of novel microfluidic devices inspired by the motions of wall contractions observed in some insects. Results show that the presented model for fluid flow at microscale is advantageous over current microfabrications in that it does not require excessive pressure drops or difficult to manufacture channels.

The manner in which insects breathe is a thriving area of research. As with all problems in science, the open questions outnumber the answers available. This thesis is presented as an invitation to further develop and challenge the ideas presented.

Appendix A

Diffusion equation modelled by Krogh

The rate of movement of oxygen (dO_2/dt) across muscle tissues under both steady-state and non-steady state conditions conforms to the one-dimensional diffusion equation for gases as modified by Krogh [71, 72],

$$\frac{dO_2}{dt} = -\frac{\kappa_{O_2} A p_{O_2}}{X}, \tag{A.1}$$

where κ_{O_2} is the diffusion constant for O_2 which is the product of the diffusion coefficient for O_2 and its solubility. $\kappa_{O_2} = D_{O_2} \times \alpha_{O_2}$: D_{O_2} is the diffusion coefficient for O_2 and α_{O_2} is the solubility coefficient for O_2. A is the surface area through which exchange occurs, p_{O_2} is the O_2 partial pressure gradient across the diffusion path, and X is the length of the diffusion path.

We also note that changing temperature affects both D_{O_2} and α_{O_2}. D_{O_2} in water increases by $\sim$ 3% for each rise in temperature of $1°C$, while solubility decreases with increasing temperature by $\sim 1.4\%°C^{-1}$. Thus, the thermal sensitivity of the diffusion constant (κ_{O_2}) is $\sim 1.6\%°C^{-1}$. D_{O_2} decreases with temperature due to:

1. reduction in the kinematic energy of the system,
2. increase in viscosity (cytoplasm viscosity), which is inversely related to cell temperature.

Appendix B

Absorption model

The absorption model can be written as a system of ordinary differential equations

$$\frac{d\mathbf{x}}{dt} = g(\mathbf{x}, p_o), \tag{B.1}$$

where $\mathbf{x}$ is a vector of state variables. We then define the mitochondria saturation function as

$$S = f(\mathbf{x}). \tag{B.2}$$

In equation 3.33 we thus have that $N_o = 1$ for O_2 uptake by mitochondria. Let $\mathbf{x} \equiv x = [MO_2]$, i.e., x denotes the concentration of O_2-mitochondria combinations. We take the mitochondria saturation function S to be $S(x) = x/T_m$, and furthermore we assume that $dx/dt = g(x, p_o) = r\sigma p_o(T_m - x) - lx$.

Thus

$$\frac{dS}{dt} = \frac{1}{T_m}\frac{dx}{dt}, \tag{B.3}$$

$$= \frac{1}{T_m}(r\sigma p_o(T_m - x) - lx). \tag{B.4}$$

With $N_o = 1$, substitute equation B.3 into equation 3.33,

$$\frac{dp_o}{dt} = \frac{D_o}{v_{ct}\sigma}(p_{to} - p_o) - \frac{T_m}{\sigma}\left(\frac{1}{T_m}(r\sigma p_o(T_m - x) - lx)\right), \tag{B.5}$$

$$= \frac{D_o}{v_{ct}\sigma}(p_{to} - p_o) - \frac{1}{\sigma}(r\sigma p_o(T_m - x) - lx). \tag{B.6}$$

The above equations can then be written in their non-dimensional form. Recall

$$\frac{dp_o}{dt} = \frac{D_o}{v_{ct}\sigma}(p_{to} - p_o) - \frac{N_o T_m}{\sigma}\frac{dS}{dt}, \tag{B.7}$$

$$\frac{dx}{dt} = g(x, p_o), \tag{B.8}$$

$$S = S(x). \tag{B.9}$$

Assume that the tracheal partial pressure of oxygen, p_{to}, is constant. Divide equation B.7 through by $p_{to} \neq 0$

$$\frac{1}{p_{to}}\frac{dp_o}{dt} = \frac{D_o}{v_{ct}\sigma}\left(1 - \frac{p_o}{p_{to}}\right) - \frac{N_o T_m}{\sigma p_{to}}\frac{dS}{dt}. \tag{B.10}$$

Let $p_r = p_o/p_{to} \rightarrow \dfrac{dp_r}{dt} = \dfrac{1}{p_{to}}\dfrac{dp_o}{dt}$. Therefore

$$\frac{dp_r}{dt} = \frac{D_o}{v_{ct}\sigma}(1 - p_r) - \frac{N_o T_m}{\sigma p_{to}}\frac{dS}{dt}, \tag{B.11}$$

$$\frac{v_{ct}\sigma}{D_o}\frac{dp_r}{dt} = 1 - p_r - \frac{N_o T_m}{p_{to}}\frac{v_{ct}}{D_o}\frac{dS}{dt} \tag{B.12}$$

Let $\tau = (D_o/v_{ct}\sigma)t$ such that $d\tau = (D_o/v_{ct}\sigma)dt$. Thus

$$\frac{dp_r}{d\tau} = 1 - p_r - \frac{N_o T_m}{\sigma p_{to}}\frac{dS}{d\tau}. \tag{B.13}$$

Let $\alpha = N_o T_m/\sigma p_{to}$. Hence

$$\frac{dp_r}{d\tau} = 1 - p_r - \alpha\frac{dS}{d\tau}. \tag{B.14}$$

Recall $dx/dt = g(x, p_o)$, $p_o = p_{to}p_r$ and $d\tau = (D_o/v_{ct}\sigma)dt$, thus

$$\frac{dx}{dt} = (r\sigma p_o(T_m - x) - lx), \tag{B.15}$$

$$\frac{D_o}{v_{ct}\sigma}\frac{dx}{d\tau} = (r\sigma p_{to}p_r(T_m - x) - lx), \tag{B.16}$$

$$\frac{dx}{d\tau} = \frac{v_{ct}\sigma}{D_o}(r\sigma p_{to}p_r(T_m - x) - lx), \tag{B.17}$$

$$\frac{1}{T_m}\frac{dx}{d\tau} = \frac{v_{ct}\sigma}{D_o}\left(r\sigma p_{to}p_r\left(1 - \frac{x}{T_m}\right) - l\frac{x}{T_m}\right). \tag{B.18}$$

Let $\tilde{x} = x/T_m$. Thus

$$\frac{d\tilde{x}}{d\tau} = \frac{v_{ct}\sigma}{D_o}\left(r\sigma p_{to}p_r\left(1 - \tilde{x}\right) - l\tilde{x}\right), \tag{B.19}$$

$$= \frac{r\sigma^2 v_{ct}}{D_o}\left(p_r\left(1 - \tilde{x}\right) - \frac{l}{r\sigma p_{to}}\tilde{x}\right). \tag{B.20}$$

Let $\beta = r\sigma^2 v_{ct}/D_o$ and $\gamma = l/r\sigma p_{to}$.

$$\therefore \quad \frac{d\tilde{x}}{d\tau} = \beta \left(p_r \left(1 - \tilde{x} \right) - \gamma \tilde{x} \right). \tag{B.21}$$

Appendix C

Large "rate factor" ($\beta \gg 1$)

To understand what happens when $\beta \gg 1$, we consider two cases when $\alpha = 0$ and $\alpha \neq 0$. The system of equations 3.40−3.42 can be analyzed in the plane $(p_r, \tilde{x})$. Solving the system at equilibrium (i.e. $dp_r/d\tau = 0$ and $d\tilde{x}/d\tau = 0$) we have $(p_r = 1, \tilde{x} = 1/(1-\gamma))$. At the equilibrium, the Jacobian matrix is given by

$$J = \begin{pmatrix} -1 - \alpha\beta\left(\frac{\gamma}{1+\gamma}\right) & \alpha\beta(1+\gamma) \\ \beta\left(\frac{\gamma}{1+\gamma}\right) & -\beta(1+\gamma) \end{pmatrix}.$$

The eigenvalues are

$$\lambda_1 = -\frac{1}{2}\left(\mathcal{P} + 1 + \frac{\alpha\beta\gamma}{(1+\gamma)}\right) + \frac{1}{2}\left((\mathcal{P}-1)^2 + \frac{\alpha\beta\gamma\mathcal{Q}}{(1+\gamma)}\right)^{1/2}, \tag{C.1}$$

$$\lambda_2 = -\frac{1}{2}\left(\mathcal{P} + 1 + \frac{\alpha\beta\gamma}{(1+\gamma)}\right) - \frac{1}{2}\left((\mathcal{P}-1)^2 + \frac{\alpha\beta\gamma\mathcal{Q}}{(1+\gamma)}\right)^{1/2}, \tag{C.2}$$

where $\mathcal{P} = \beta(1+\gamma)$ and $\mathcal{Q} = 2\beta(1+\gamma) + 2 + (\alpha\beta\gamma)/(1+\gamma)$.

Case 1: When $\alpha = 0$, $\lambda_1 = -1$ and $\lambda_2 = -\beta(1+\gamma)$. The corresponding eigenvectors are

$$\mathbf{v_1} = \left[1, \frac{-\beta\gamma}{(1+\gamma) - \beta(1+\gamma)^2}\right]^T, \quad \text{and} \tag{C.3}$$

$$\mathbf{v_2} = [0, 1]^T. \tag{C.4}$$

For $\beta \gg 1$, $|\lambda_2| \gg |\lambda_1|$ and $\mathbf{v_1} \approx [1, \gamma/(1+\gamma)^2]$. That is, at equilibrium, $\mathbf{v_1}$ is tangent to the saturation curve $\tilde{S} = p_r/(p_r + \gamma)$ which is one of the nullclines in the system.

Case 2: When $\alpha \neq 0$, trajectories are trapped between the nullclines

$$\tilde{x} = \frac{p_r}{p_r + \gamma} \quad \text{(at which } \; d\tilde{x}/d\tau = 0), \quad \text{and} \tag{C.5}$$

$$\tilde{x} = \frac{p_r(1 + \alpha\beta) - 1}{\alpha\beta(p_r + \gamma)} \quad \text{(at which } \; dp_r/d\tau = 0). \tag{C.6}$$

For $\beta \gg 1$, the two nullclines are closed to each other (i.e. $\forall\ \alpha\beta \gg 1$, we have $(p_r(1 + \alpha\beta) - 1)/(\alpha\beta(p_r + \gamma)) \approx p_r/(p_r + \gamma)$). This means that for large β trajectories will be near the saturation curve. When $\alpha \neq 0$, $|\lambda_1| < 1$ and $|\lambda_2| > \beta(1 + \gamma)$ therefore the transient towards the saturation curve is faster than for the case when $\alpha = 0$. (Note that in the limit $\lambda_1 \to 0$ as $\alpha \to \infty$ since J becomes singular. λ_1 increases monotonically and therefore is never positive).

Appendix D

Model for the chemical reactions

We consider the reaction (3.59) given by

$$CO_2 + H_2O \rightleftharpoons_{\delta l_2}^{\delta r_2} H^+ + HCO_3^-. \tag{D.1}$$

The chemical reaction considered above is not coupled with either diffusion and ventilation, thereby mimicking an experiment in-vitro.

The rate equations for each of the reactions is given by

$$\bar{r}_1 = \delta r_2 CO_2(t) H_2O(t), \tag{D.2}$$

$$\bar{r}_2 = \delta l_2 HCO_3^-(t) H^+, \tag{D.3}$$

where H^+ is assumed to be constant.

The governing equations for the rate of change of the concentrations of each chemical species depend on the rate equations and the reactions

$$CO_2^{'}(t) = \bar{r}_2 - \bar{r}_1, \tag{D.4}$$

$$H_2O^{'}(t) = \bar{r}_2 - \bar{r}_1, \tag{D.5}$$

$$HCO_3^{-'}(t) = \bar{r}_1 - \bar{r}_2. \tag{D.6}$$

Appendix E

Parameters and variables

This section lists the parameters and variables that appear frequently in this manuscript (unless stated otherwise in the text). Table E.1 lists the parameters and their values used in the model simulations. Note that the parameter values are estimated from literature data and in cases where they could not be found, they were estimated. Even though some were assumed, there are also some parameters that were calculated. The diffusion capacities, D_o and D_c, depend on the surface area and the thickness of the membrane across which the diffusion takes place. The parameters presented here are for simulation purposes. It should be noted that no attempt has been carried out to carefully fit parameters to a specific experiment since the developed models are simple and cannot be expected to match experimental data exactly. Variables are presented in Table E.2. Note that t is an independent variable here. For the duration of the DGC phenomena in insects, ν would be lower than used in the simulations but the results would not change qualitatively. During periods of flutter, the pressure within the tracheal system is very close to atmospheric, although slightly negative. The negative pressure causes an inward mass flow of air. When the spiracles completely close, the pressure in the tracheal system drops precipitously. Thus for P_s and the initial value of P_T we use 760 $mmHg$ which is the atmospheric pressure at sea level.

Note that δ is interpreted as a (dimensionless) quantity which affects the buffering capacity of the hemolymph.

Parameters		
Symbol	Meaning	Value
P_s	Spiracle pressure	760 $mmHg$ [77]
p_w	Water vapor pressure at 25^oC	23.8 $mmHg$ [78]
f_{oi}	Ambient air concentration of O_2	0.21 [79]
f_{ci}	Ambient air concentration of CO_2	0 [79]
V_0	Volume when spring is unloaded	0.001 l [73]
v_{ct}	Volume of cell/cytoplasm	0.071 l (estimated from plant cells [80])
R_s	Resistance of airways to flow	2.5 $mmHg\ s\ l^{-1}$ (assumed)
E_T	Elastance of trachea	1 $mmHg\ l^{-1}$ (assumed)
D_o	O_2 diffusion capacity	$3.5 \times 10^{-4}\ mol\ s^{-1}\ mmHg^{-1}$ [73]
D_c	CO_2 diffusion capacity	$7.08 \times 10^{-4}\ mol\ s^{-1}\ mmHg^{-1}$ [73]
ν	Frequency of DGC	2π / 5 rad s^{-1} [54]
σ	Solubility of O_2 in cytoplasm	$1.4\times\ 10^{-6}\ mol\ l^{-1}\ mmHg^{-1}$ [74]
σ_c	Solubility of CO_2 in cytoplasm	$3.3 \times 10^{-5}\ mol\ l^{-1}\ mmHg^{-1}$ [74]
T_m	Concentration of mitochondria	$2\times\ 10^{-3}\ mol\ l^{-1}$ [84]
r	Rate constant for recombination	$3.6 \times 10^3\ l\ mol^{-1}\ s^{-1}$ [82]
l	Rate constant for dissociation	26.8 s^{-1} [82]
h	Concentration of H^+	$10^{-7.4}\ mol\ l^{-1}$ [81]
r_2	Dehydration reaction rate	0.12 s^{-1} [76, 83]
l_2	Hydration reaction rate	$164 \times 10^3\ l\ s^{-1}\ mol^{-1}$ [76, 83]
δ	Acceleration parameter	0.3 (calculated)

TABLE E.1: Parameter list.

Variables		
Symbol	Meaning	Initial value
P_T	Tracheal total pressure	$P_s\ mmHg$ [77]
p_{to}	Tracheal partial pressure of O_2	97.5 $mmHg$ [64, 75]
p_{tc}	Tracheal partial pressure of CO_2	37.5 $mmHg$ [64, 75]
p_o	Respiratory cell partial pressure of O_2	40 $mmHg$
p_c	Respiratory cell partial pressure of CO_2	46 $mmHg$
f_o	Concentration of O_2 in the trachea	0.1368
f_c	Concentration of CO_2 in the trachea	0.05263
CO_2	Concentration of CO_2	46 $\sigma_c\ moll^{-1}$ [76]
y	Concentration of HCO_3^{-1}	(40 $\sigma_c r_2$) / ($l_2 h$) $moll^{-1}$
q	Airflow	0 ls^{-1}

TABLE E.2: Variables initial values list.

Bibliography

[1] Alligood, T., Sauer, T.D., and Yorke, J.A., 1996. Chaos: An Introduction to Dynamical Systems. Springer-Verlag, New York.

[2] Cosner, C., DeAngelis, d.L., Ault, J.S., and Olson, D.B., 1999. Effects of Spatial Grouping on the Function Response of Predators. Theor. Pop. Biol. **56**, 65-75.

[3] Edelstein-Keshet, L., 1977. Mathematical Models in Biology. McGraw-Hill, Inc.

[4] Feng, W., Lu, X., and Liu, W., 1997. Comparison and Numerical Solutions for Diffusive Models of Resource and Sexual Competition. Non-linear Analysis, Theory, Methods and Applications. **30**, 2765-2774.

[5] Jansen, V.A., 1994. Theoretical Aspects of Metapopulation Dynamics. Ph.D Thesis, Leiden Univ, Netherlands.

[6] Manson, L., and Lundberg, P., 2006. An analysis of the analysis of herbivore population dynamics. OIKOS. **113**, 217-225.

[7] Kestler, P., 1985. Respiration and respiratory water loss. In: Environmental physiology and biochemistry of insects (Hoffmann K.H. ed). New York: Springer-Verlag, 137-183.

[8] Lighton, J.R., 1994. Discontinuous ventilation in terrestrial insects. Physiol. Zool. **67**, 142-162.

[9] Snyder, G.K., Shearor, B., Scholnick, D., and Farrelly, C., 1994. Gas exchange in the insect tracheal system. J. Theor. Biol. **172**, 199-207.

[10] Levy, R.I., and Schneiderman, H.A., 1966. Discontinuous respiration in insects - IV. Changes in intratracheal pressure during the respiratory cycle of silkworm pupae. J. Insect. Physiol. **12**, 465-492.

[11] Mellany, K., 1934. The site of loss of water from insects. Proc. R. Soc. Lond. **166**, 139-149.

[12] Welch, W.R., and Tracy, C.R., 1977. Respiratory water: A predictive model. J. Theor. Biol. **65**, 253-265.

[13] Woods, H.A., and Smith, J.N., 2010. Universal model for water costs of gas exchange by plants and animals. PNAS. **107**, 8469-8474.

[14] Pickard, W.F., 1974. Transaction regime diffusion and the structure of the insect tracheola system. J. Insect. Physiol. **20**, 947-956.

[15] Wigglesworth, V.B., 1965. The principles of insect physiology. Methuen, London, 6th Ed.

[16] Wasserthal, L.T., Cloetens, P., Fink, R., and Rack, A., 2009. Physiological measurements combined with synchrotron video-radiography and x-ray tomography for analysis of respiratory gas exchange and tracheal structure in flies. *2nd International congress of respiratory science.* Hildesheim, Berlin. Tharax Verlag.

[17] Punt, A., 1956. The influence of carbon dioxide on the respiration of Carabus nemoralis Mull. Physiologia Comparata et Oecologia. **4**, 130-139.

[18] Schneiderman, H.A., and Williams, C.M., 1955. An experimental analysis of the discontinuous respiration of the cecropia silkworm. Biological bulletin. **109(1)**, 123-143.

[19] Schneiderman, H.A., 1960. Discontinuous respiration in insects: role of the spiracles. Biological bulletin. **119(3)**, 494.

[20] Forster, T.D., and Hetz, S.K., 2008. Spiracular constriction-obeying the rules of compliance. In S. Morris and A. Vosloo, editors, *Molecules to migration: The pressures of life*, 4th CPB Meeting in Africa: Mara 2008, pp 285-292. Medimond, Bologna, 2008.

[21] Miller, P.L., 1982. Respiration in the American Cockroach (ed H.J. Bell & K.G. Adiyodi), Chapman & Hall, London, 87-116

[22] Gibbs, A.G., and Johnson, R.A., 2004. Role of Discontinuous Gas Exchange in insects: The chthonic hypothesis does not hold water. J. Exper. Biol. **207**, 3477-3482

[23] Bugboy52.40. Citing Website. Wikipedia. Retrieved October 21, 2013, from http://en.wikipedia.org/wiki/File:Fiddler_beetle_morphology_diagram.svg

[24] Hetz, S.K., and Bradley, T.J., 2005. Insects breathe discontinuously to avoid oxygen toxicity. NATURE. **433**, 516-519.

[25] Marais, E., Klok, C.J., Terblanche, J.S., and Chown, S.C., 2005. Insect gas exchange patterns: a phylogenetic perspective. J. Exper. Biol. **208**, 4495-4507.

[26] Wobschall, A., and Hetz, S.K., 2004. Oxygen uptake by convection and diffusion in diapausing moth pupae. Int. Congr. Ser. **1275**, 157-164.

[27] Chown, S.C., Gibbs, A.G., Hetz, S.K., Klok, C.J., Lighton, J.R., and Marais, E., 2006. Discontinuous Gas Exchange in Insects: a Clarification of Hypothesis and Approaches. Physiol. Biochem. Zool. **79**, 333-343.

[28] Levy, R.I., and Schneiderman, H.A., 1958. An experimental solution to the paradox of discontinuous respiration in insects. Nature, Lond. **182**, 491-493.

[29] Lehmann, F.O., 2001. Matching spiracle opening to metabolic need during flight in drosophila. Science. Mag. **294**, 1926-1929.

[30] Schmitz, A., and Wasserthal, L.T., 1999. Comparative morphology of the spiracles of the Papilionidae, Sphingidae, and Saturniidae (Insecta: Lepidoptera). J. Insect Morphology and Embryology. **28(1−2)**, 13-26.

[31] White, C.R., Blackburn, T.M., Terblanche, J.S., Marais, E., Gibernau, M., and Chown, S.L., 2007. Evolutionary responses of discontinuous gas exchange in insects. Preceedings of the National Academy of Sciences. **104(20)**, 8357-8361.

[32] Matthews, P.G., and White, C.R., 2009. Rhinoceros beetles modulate spiracular opening to regulate haemolymph pH. Comparative Biochemistry and Physiology - Part A: Molecular and Integrative Physiology. **153(2-1)**, 101-102.

[33] Bradley, T.J., 2007. Control of the respiratory pattern in insects. Adv. Exp. Med. Biol. Springer New York. **618**, 211-220.

[34] Arditi, R., and Ginzburg, L.R., 1989. Coupling in predator-prey dynamics: ratio dependence. J. Theor. Biol. **139**, 311-326.

[35] Hanski, I. 1991. The functional response of predators: worries about scale. Trends Ecol. Evol. **6**, 141-142.

[36] Ginzburg, L.R., and Akcakaya, H.R., 1992. Consequences of ratio−dependent predation for steady−state properties of ecosystems. Ecology. **73**, 1536-1543.

[37] Abrams, P.A., 1994. The fallacies of ratio dependent predation. Ecology. **75**, 1842-1850.

[38] Berryman, A.A., 1992. The origins and evolution of predator-prey theory. J. Ecology. **73(5)**, 1530-1535.

[39] Mansson, L., and Lundberg, P., 2006. An analysis of the analysis of herbivore population dynamics. OIKOS. **113**, 217 - 225.

[40] Akcakaya, H.R., Arditi, R., and Ginzburg, L.R., 1995. Ratio-Dependent predation: an abstraction that works. Ecology. **76(30)**, 995 - 1004.

[41] Abrams, P.A., and Ginzburg, L.R., 2000. The nature of predation, ratio dependent nor neither. TREE. **17(8)** 337 - 341.

[42] Feng, W., Lu, X., and Donovan, R.J., 2001. Population Dynamics in a Model for Territory Acquisition. Discrete and Continuous Dynamical systems. added volume, 156-165.

[43] Fernandez, B., 2008. A naturalized approach to the autonomy of cognitive agents. PhD Thesis. University of Basque County.

[44] Chown, S.L., and Nicolson, S.W., 2004. Insect Physiological Ecology: Mechanisms and Patterns, pp. 49-86. New York: Oxford University Press.

[45] Lighton, J.R., 1996. Discontinuous gas exchange in insects. Annu. Rev. Entomol. **41**, 309-324.

[46] Quinlan, M.C., and Gibbs, A.G., 2006. Discontinuous gas exchange in insects. Respir. Physiol. Neurobiol. **154**, 18-29.

[47] Westneat, M.W., Betz, O., Blob, R.W., Fezzaa, K., Cooper, W.J., and Lee, W.K., 2003. Tracheal respiration in insects visualized with synchrotron x-ray imaging. Science. **299**, 558-560.

[48] Westneat, M.W., Socha, J.J., and Lee, W., 2008. Advances in biological structure, function, and physiology using synchrotron x-ray imaging. Annual Review of Physiology. **70**, 119-142.

[49] Socha, J.J., Lee, W.K., Harrison, J.F., Waters, J.S., Fezzaa, K., and Westneat, M.W., 2008. Correlated patterns of tracheal compression and convective gas exchange in a carabid beetle. Journal of Experimental Biology. **211**, 3409-3420.

[50] Chapman, R.F., 1998. The insects - structure and function. Cambridge University Press. **4**, edition.

[51] Beckel, W.E., and Schneiderman, H.A., 1957. Insect spiracle as an independent effector. Science. **126 (3269)**, 352-353.

[52] Duncan, F.D., and Byrne, M.J., 2002. Respiratory airflow in a wingless beetle, J. Exper. Biol. **205**, 2489-2497.

[53] Duncan, F.D., 2002. The role of the subelytral cavity in water loss in the flightless dung beetle, circellium bacchus (Coleoptera: Scarabaeinae). Eur. J. Entomol. **99**, 253-258.

[54] Duncan, F.D., and Byrne, M.J., 2005. The role of the mesothoracic spiracles in respiration in flighted and flightless dung beetles, J. Exper. Biol. **205**, 2489-2497.

[55] Mangun, C.P., Scott, J.L., Black, R.E.L., Miller, K.I., and Van Holde, K.E., 1985. Centipedal hemocyanin: its structure and its implications for arthropod phylogeny. Proc. Natl. Acad. Sci. **82** 3721-3725.

[56] Kestler, P., 2003. Physiological gas exchange strategies for spiracular control. Comp. Biochem. Physiol. A 134, (Suppl 1). 973.

[57] Simelane, S.M., Abelman, S., and Duncan, F.D., 2014. Dynamics of oxygen, carbon dioxide, and water interaction across the insect spiracle. Abstract and Applied Analysis. **157573** (11pp).

[58] Pikovsky, A., Rosenblum, M., and Kurths, J., 2003. Synchronization: a universal concept in nonlinear sciences. Cambridge University Press.

[59] Nation, J.L., 2002. Insect physiology and biochemistry. CRC Press LLC. pp 327-347.

[60] Maina, J.N., 2002. Structure, function and evolution of the gas exchangers: comparative perspectives. J. Anat. **201** 281-304.

[61] Socha, J.J., Forster, T.D., and Greenlee, K.J., 2010. Issues of convection in insect respiration: Insights from synchrotron X-ray imaging and beyond. Resp. Physiol. Neur. **173** 65-73.

[62] Miller., P.L., 1974. Respiration−aerial gas transport. The physiology of insecta. Academic Press, 2nd edition, **6** 346-402.

[63] Lehman, F., and Heyman, N., 2005. Unconventional mechanisms control cyclic respiratory gas release in flying *Drosophila*. J. Exp. Biol. **208** 3645-3654.

[64] Groenewald, B., Hetz, S.K., Chown, S.L., and Terblanche, J.S., 2012. Respiratory dynamics of discontinuous gas exchange in the tracheal system of the desert locust, *Schistocerca gregaria*. J. Exp. Biol. **215** 2301-2307.

[65] Sanchez, D., Ganfornina, M.D., Gutierrez, G., and Bastiani, M.J., 1998. Molecular Characterization and Phylogenetic Relationships of a Protein with Potential Oxygen-Binding Capabilities in the Grasshopper Embryo. A Hemocyanin in Insects? Mol. Biol. Evol. **15(4)** 415-426.

[66] Burmester, T., and Hankeln, T., 2007. The respiratory proteins of insects. J. Ins. Physiol. **53(4)** 285-294.

[67] Ben-Tal, A., 2004. Simplified models for gas exchange in the human lungs. J. Theor. Biol. **238** 474-495.

[68] Batzel, J.J., and Tran, H.T., 2000. Modeling instability in the control system for human respiration: applications to infant non-REM sleep. Appl. Math. Comput. **110** 1-51.

[69] Palus, M., and Stefanovska, A., 2003. Direction of coupling from phases of interacting oscillators: an information-theoretic approach. Phys. Rev. E **67**, 055201(R).

[70] Levenbook, L., and Clarke, M., 1950. The physiology of carbon dioxide transport in insect blood. Experimental Biology. **27**, 175-183.

[71] Krogh, A., 1919. The number and distribution of capillaries in muscles with calculations of the oxygen pressure head necessary for supplying tissue. J. Physiol. **52** 409-415.

[72] Krogh, A., 1959. The anatomy and physiology of capillaries. New York: Hafner Publishing.

[73] Schmitz, A., and Perry, S.F., 1999. Stereological Determination of Tracheal Volume and Diffusing Capacity of the Tracheal Walls in the Stick Insect *Carausius morosus* (Phasmatodea, Lonchodidae). J. Physiol. Biochem. Zool. **72(2)**, 205-218.

[74] Guyton, A.C., and Hall, J.E., 1996. Textbook of medical physiology. W B Saunders Company. 9^{th} ED.

[75] Masserthal, L.T., 2014. Periodic heartbeat reversals cause cardiogenic inspiration and expiration with coupled spiracle leakage in resting bow flies, *Calliphora Vicina*. J. Exp. Biol. **217** 1543-1554.

[76] Gibbons, B.H., and Edsall, J.T., 1963. Rate of Hydration of Carbon Dioxide and Dehydration of Carbonic Acid at 25^o. J. Biol. Chem. **238(10)**, 3502-3507.

[77] Schmidt-Nielsen, K., 1997. Animal physiology: adaptation and environment. Cambridge University Press. 5^{th} Ed.

[78] Murphy, D.M., and Koop, T., 2005. Review of the vapor pressures of ice and super cooled water for atmospheric applications. Q.J.R. Meteorol. Soc. **131** 1539-1565.

[79] Hill, R.W., 1972. Determination of oxygen consumption by use of the paramagnetic oxygen analyzer. J. Appl. Physiol. **33(2)** 261-263.

[80] Owens, T., and Poole, R.J., 1979. Regulation of cytoplasm and vacuolar volumes by plant cells in suspension culture. J. Plant Physiol. **64** 900-904.

[81] Keener, J., and Sneyd, J., 1998. Mathematical physiology Springer, Berlin.

[82] Cai, W.J. and Wang, Y., 1998. The chemistry, fluxes and sources of carbon dioxide in the estuarine waters of the Satila and Altamaha Rivers, Georgia. Limnol; Oceanog. **43**, 657-668.

[83] Bidani, A., Crandall, E.D., and Forster, R.E., 1978. An analysis of postcapillary pH changes in blood in vivo after gas exchange. J. Appl. Physiol.: Respir. Environ. Exercise Physiol. **44(5)** 770-781.

[84] Larsen, W.J., 1970. Genesis of mitochondria in insect fat body. J. Cell Biol. **47** 373-383.

[85] Forster, T.D., 2010. Spiracular control in moth pupae: passive generation respiratory patterns. Dissertation. Humboldt−Universitst Berlin.

[86] Hetz, S.K., Wasserthal, L.T., Hermann, S., Kaden, H., and Oelbner, W., 1994. Direct oxygen measurements in the tracheal system of lepidopterous pupae using miniaturized amperometric sensors. Bioelectrochemistry and Bioenergetics, **33(2)**, 165-170.

[87] Burkett, B.N., and Schneiderman, H.A., 1974b. Roles of oxygen and carbon dioxide in the control of spiracular function in *cecropia* pupae. Biological Bulletin, **147(2)**, 274-293.

[88] Grieshaber, B.J., and Terblanche, J.S., 2015. A computational model of insect discontinuous gas exchange: a two-sensor, control systems approach. J. Theor. Biol. **374**, 138-151.

[89] Contreras, H.L., and Bradley, T.J., 2009. Metabolic rate controls respiratory pattern in insects. J. Exp. Biol. **212**, 424-428.

[90] Terblanche, J.S., Marais, E., Hetz, S.K., and Chown, S.L., 2008. Control of discontinuous gas exchange in Samia cynthia: effects of atmospheric oxygen, carbon dioxide and moisture. J. Exp. Biol. **211**, 3272-3280.

[91] Chown, S.L., and Holter, P., 2000. Discontinuous gas exchange cycle in *Aphodius fossor* (Scarabaeidae): a test of hypotheses concerning origins and mechanisms. J. Exp. Biol. **203**, 397-403.

[92] Snelling, E.P., Seymour, R.S., and Runciman, S., 2011. Moulting of insect tracheae captured by light and electron-microscopy in the metathoracic femur of a third instar locust *Locusta migratoria*. J. Insect Physiol. **57**, 1312-1316.

[93] Pendar, H., Kenny, M.C., and Socha, j., 2015. Tracheal compression in pupae of the beetle *Zophobas morio*. Biol. Letters. **11**, 20150209.

[94] Bizourn, P., Blanloeil, Y., and Pinaud, M., 1995. Comparison between oxygen consumption calculated by Fick's principle using a continuous thermodilution technique and measured by indirect calorimetry. J. Anaeth. **75**, 719-723.

[95] Hanique, G., Dugernier, T., Laterre, P.F., Roeseler, J., Dougnac, A., and Reynaert, M.S., 1994. Evaluation of oxygen uptake and delivery in critically ill patients: a statistical reappraisal. J. Intensive Care. Med. **20**, 19-26.

[96] Hlastala, M.P., and Berger, A.J., 2001. Physiology of respiration. 2nd Ed. Oxford University Press, Oxford.

[97] Bishop, G.H., 1923. Body fluid of the honey bee larva. I. Osmotic pressure, specific gravity, pH, O_2 capacity, CO_2 capacity, and buffer value, and their changes with larval activity and metamorphosis. J. Biol. Chem. **58**, 543-565.

[98] Babers, F.H., 1941. Glycogen *Prodenia eridania*, with special reference the ingestions of glucose. J. Agric. Res. **62**, 509-530.

[99] Kelley, C.T., 1999. Iterative Methods for optimization. SIAM.

[100] Chen, C.L., and Liu, Y.C., 1998. Differential transform technique for steady nonlinear heat conduction problems. Appl. Math. Comput. **97**, 155-164.

[101] Jang, M.J., and Chen, C.L., 1997. Analysis of the response of a strongly nonlinear damped system using a differential transform technique. Appl. Math. Comput. **88**, 137-151.

[102] Thongmoon, M., and Pusjuso, S., 2010. The numerical solutions of differential transform method and the Laplace transform method for a system of differential equations. Nonlinear analysis: Hybrid systems. **4**, 425-431.

[103] Jafari, H., Alipour, M., and Tajadodi, H., 2010. Two-dimensional differential transform method for solving nonlinear partial differential equations. J. Research and Reviews in Applied Sciences. **2(1)**, 47-52.

[104] Ndlovu, L.P., and Moitsheki, R.J., 2013. Applications of the two-dimensional differential transform method to heat conduction problem for heat transfer in longitudinal rectangular and convex parabolic fins. Commun. Nonlin. Sci. Num. Simul. **18(10)**, 2689-2698.

[105] Zhou, J.K., 1986. Differential transform method and its applications for electric circuits. Huazhong University Press. Wuhan, China.

[106] Kanth, A.S.V., and Aruna, K., 2008. Differential transform method for solving the linear and non-linear systems of partial differential equations. Phys. Lett. A, **372**, 6896-6898.

[107] Kanth, A.S.V., and Aruna, K., 2008. Differential transform method for solving the linear and non-linear Klein-Gordon equation. Comput. Phys. Commun. **180**, 708-711.

[108] Chen, C.K., and Ho, S.H., 1996. Applications of differential transformation to eigenvalue problems. Appl. Math. Comput. **79**, 173-188.

[109] Biazar, J., and Eslami, M., 2010. Differential transform method for quadratic Riccati differential equation. J. Nonlinear Sci. **9**, 444-447.

[110] Arikoglu, A., and Okzol, I., 2007. Solution of fractional differential equations by using differential transform method. Chaos, Solitons and Fractals. **34**, 1473-1481.

[111] Kangalgil, F., and Ayaz, F., 2009. Solitary wave solution for thr KdV and mKdV equations by differential transform method. Chaos, Solitons and Fractals. **41**, 464-472.

[112] Ayaz, F., 2004. Applications of differential transform method to differential-algebraic equations. Appl. Math. Comp. **152**, 649-657.

[113] Chen, C.L., and Liu, Y.C., 1998. Solution of two point boundary value problems using the differential transform method. J. Opt. Theory Appl. **99**, 23-35.

[114] Arkilic, E.B., Schmidt, M.A., and Kenneth, S.B., 1997. Gaseous slip flow in long microchannels. J. Microelectromechanical Systems, **6(2)** 167 - 178.

[115] Arkilic, E.B., Schmidt, M.A., and Kenneth, S.B., 1994. Gaseous flow in microchannels. Applications of Microfabrication to ss. ASME Winter Annu. Meet. Chicago, IL., 57-65.

[116] Whitesides, G.M., 2006. The origins and the future of microfluidics. Nature. **442** 368 - 373.

[117] Wang, X., Cheng, C., Wang, S., and Liu, S., 2009. Electroosmotic pumps and their applications in microfluidic systems. Microfluidic Nanofluidics. **6(2)**: 145.

[118] Li, M., and Brasseur, J.G., 1993. Non-steady peristaltic transport in finite-length tubes. J. Fluid Mech. **248**, 129-151.

[119] Macagno, E., and Christensen, J., 1980. Fluid mechanics of the duodenum. Ann. Rev. Fluid Mech. **12**, 139-158.

[120] Macagno, E., and Christensen, J., 1982. Modelling the effect of wall movement on absorption in the intestine. Am. J. Physiol. **243**, 541-550.

[121] Hayat, T., Saleem, N., and Ali, N., 2009. Peristaltic flow of a carreau fluid in a channel with different wave forms. Numerical methods for partial differential equations. **26**, 519-534.

[122] Aboelkassem, Y., and Staples, A.E., 2013. Selective pumping in a network: insect-style microscale flow transport. Bioinspir. Biomim. **8 (026004)**, (22 pp).

[123] Harrison, J.F., 2003a. Respiratory systems. Encyclopedia of insects. ed V.H. Resh and R.T. Carde. Amsterdam; Boston: Academic Press.

[124] Tabor, D., 1979. Gases, liquid and solids. **2nd** ed. Cambridge University Press. Cambridge.

[125] Walton, A.J., 1983. Three phases of matter. **2nd** ed. Clarendon Press. Oxford.

[126] Uchida, S., and Aoki, H., 1977. Unsteady flows in a semi-infinite contracting or expanding pipe. J. Fluid Mech. **82**, 371-387.

[127] Sacomb, T.W., 1978. Flow in a channel with pulsating walls. J. Fluid Mech. **88**, 273-288.

[128] Skalak, F.M, and Wang, C.Y., 1978. On the unsteady squeezing of a viscous fluid from a tube. J. Aust. Math. Soc. Ser. B. **21**, 65-74.

[129] Singh, P., Radhakrishnan, V., and Narayan, K.A., 1990. Squeezing flow between parallel plates. Ing. Arch. **60**, 274-281.

[130] Wang, C.Y., 1980. Arbitrary squeezing of fluid from a tube at low squeeze numbers. J. Appl. Math. Phys. **31**, 620-627.

[131] Ralph, M., and Pedley, T.J., 1988. Flow in a channel with moving indentation. J. Fluid Mech. **190**, 87-112.

[132] Mahmood, T., and Merkin, J., 1990. The flow in a narrow duct with indentation or hump on one wall. Warme-und Stoffubertrangung. **22**, 69-76.

[133] Aboelkassem, Y., and Staples, A.E., 2012a. Flow transport in a microchannel induced by moving wall contractions:a novel micropumping mechanism. Acta Mech. **223**, 463-480.

[134] Aboelkassem, Y., and Staples, A.E, 2012b. Stokeslets-meshfree computations and theory for flow in a collapsible microchannel. Theor. Comput. Fluid Dyn. **27(5)**, 681-700.

[135] Aboelkassem Y., Staples, A.E., and Socha, J., 2011. Microscale flow pumping inspired by rhythmic tracheal compressions in insects. Proc. ASME Pressure Vessels and Piping Conf. paper no. PVP2011-57061.

[136] Yang, F., 2010. Slip Boundary Condition for Viscous Flow over Solid Surfaces. Chem. Eng. Comm. **197**, 544-550.

[137] Meijing, L., and Brasseur, J.G., 1993. Non-steady peristaltic transport in finite-length tubes. J. Fluid Mech. 248, 129-151.

[138] Batchelor, G.K., 1967. An Introduction to Fluid Dynamics. Cambridge University Press, Cambridge.

[139] Pandolfi, A., and Ortiz, M., 2007. Improved design of low-pressure fluidic microvalves. J. Micromech. Microeng. 17, 1487-1493.

[140] Lord, R., 1977. Tangential momentum accommodation coefficients of rare gases on polycrystalline metal surfaces. Rarefied Gas Dynamics. J. Potter, Ed. New York, NY: American Instit. Aeronautics and Astronautics.

[141] Seidl, M., and Steinheil, E., 1974. Measurements of momentum accommodation coefficients on surfaces characterized by Auger spectroscopy, Sims and LEED. Rarefied Gas Dynamics. M. Becker and M. Fieberg, Eds. Berlin, Germany: DFVLR Press.

[142] Steinheil, E., Scherber, M., and Seidl, M., 1977. Investigations on the interaction of gases and well-defined solid surfaces with respect to possibilities for reduction of aerodynamic friction and aerothermal heating. Rarefied Gas Dynamics, J. Potter, Ed. American Instit. Aeronautics and Astronautics.

[143] Cai, C., Liu, D.D., and Boyd, I.D., 2007. Compressible gas flow inside a two dimensional uniform microchannel. AIAA Aerospace Sciences Meeting. Reno, Nevada.

[144] Massey, B., 1989. Mechanics of Fluids. **6th** ed. London, U.K.: Van Nostrand.

[145] Glowinski, R., and Lichnewsky, A., 1990. Computing methods in applied sciences and engineering. SIAM. pp 162 - 164.

[146] Gullan, P.J., and Cranston, P.S., 2014. The Insects: An Outline of Entomology. John Willey and Sons. **5th** ed.

[147] Pong, K., Ho, C., Liu, J., and Tai, Y., 1994. Nonlinear pressure distribution in uniform microchannels. in Appl. Microfabrication to Fluid Mechanics, ASME Winter Annu. Meet., Chicago, IL, pp. 51-56.

[148] Zohar, Y., Lee, S.Y., Lee, W.Y., Jiang, L., and Tong, P., 2004. Subsonic gas flow in a straight and uniform microchannel. J. Fluid Mechanics, **472** 125-151.

[149] Beskok, A., and Karniadakis, G., 1993. Simulation of heat and momentum transfer in micro-geometries. AIAA Paper 93-3269.

[150] Prud'homme, R., Chapman, T., and Bowen, J., 1986. Laminar compressible flow in a tube . Appl. Sci. Res. **43**, 67-74.

[151] Withers, C.P., 1992. Comparative animal physiology. Sanders College Publishing. Orlando.

[152] van den Berg, H.R., ten Seldam, C.A., and van der Gulik, P.S., 1993. Compressible laminar flow in a capillary. J. Fluid Mech. **246**, 1-20.

[153] Harley, J., Huang, J., Bau, H., and Zemel, J.N., 1995. Gas flow in microchannels. J. Fluid Mech. **284**, 257-274.

[154] Piekos, E., and Breuer, K., 1995. DSMC modeling of micromechanical devices. AIAA Paper 95-2089.

[155] Oran, E.S., Oh, C.K., and Cybyk, B.Z., 1998. Direct simulation Monte Carlo: Recent advances and applications. Ann. Review of Fluid Mechanics. **30** 403 - 441.

[156] Cai, C., Boyd, I., Fan, J., and Candler, G.V., 2000. Direct simulation methods for low-speed microchannel flows. J. Thermophysics and Heat Transfer, **14** 368-378.

[157] Xu, K., and Li, Z., 2004. Microchannel flow in the slip regime: gas-kinetic BGK-Burnett solutions. J. Fluid Mechanics. **513** 87 - 110.

[158] van der Kloot, W.G., 1963. The electrophysiology and the nervous control of the spiracular muscle of pupae of the giant silkmoths. Comparative Biochemistry and Physiology. **9(4)**, 317-333.